



STScI | SPACE TELESCOPE
SCIENCE INSTITUTE

Instrument Science Report WFC3 2022-04

Monitoring WFC3/UVIS Photometric Sensitivity with Spatial Scans

Mariarosa Marinelli, Varun Bajaj, Annalisa Calamida, Harish Khandrika,
Jennifer Mack, Aidan Pidgeon, Clare Shanahan, & Debopam Som

July 6, 2022

ABSTRACT

Using five years of observations from the Hubble Space Telescope (HST) Wide Field Camera 3 (WFC3), we assess the changing sensitivity rate of the two WFC3/UVIS charge-coupled devices (CCDs) and evaluate the photometric repeatability of the spatial scan observing mode in comparison to the standard staring mode. We perform aperture photometry on vertical, linear spatial scans of two white dwarf standard stars (GD153 and GRW+70D5824) taken on corner subarrays of the WFC3/UVIS detector, and compute the rate of photometric sensitivity decline from 2017 to 2021. To gauge the relative accuracy of scans, we compare sensitivity losses for staring mode observations over the same 5-year time scale and those acquired over longer time scales. After removing the time-dependence of the relative photometry, dispersion of the residuals is used as a proxy to measure repeatability of observing modes, and thus assess precision. We establish that spatial scans are more precise than staring mode observations. Scans with UVIS 1 show $2.4\times$ less residual noise than their staring mode counterparts; for UVIS 2, residual noise for scans is $2.5\times$ less than residual noise for staring mode. For scans, sensitivity losses are relatively flat independent of wavelength on both UVIS CCDs, with no evidence of contamination. UVIS 2 appears to have slightly higher losses (-0.17 ± 0.01 %/yr) compared to UVIS 1 (-0.12 ± 0.01 %/yr). When measured over the same time period, spatial scans and staring mode observations yield filter-dependent loss rates that agree well with each other in most filters within computed uncertainties.

Contents

1. Introduction	3
2. Observations	6
2.1. Purpose and Scope of UVIS Photometric Monitoring Calibration Programs .	7
2.2. Spatial Scan Observation Parameters	9
2.2.1 Subarray Apertures	9
2.2.2 Post-flash	9
2.2.3 Filters and Targets	9
2.2.4 Scan Trajectory	10
3. Data	11
3.1. Acquisition and Calibration	11
3.2. Visual Inspection	12
3.3. Data Reduction	13
3.3.1 Considerations for Cosmic Ray Rejection	13
3.3.2 Geometric Distortion	15
3.3.3 Sky Subtraction	16
3.3.4 Aperture Photometry	17
3.4. Staring Mode Data	20
4. Analysis	22
4.1. Instrument Sensitivity	22
4.2. Photometric Repeatability	23
5. Results	24
5.1. Instrument Sensitivity	24
5.2. Photometric Repeatability	33
6. Discussion	37
6.1. Future Improvements to Scan Photometry	38
6.2. Software Tools	38
6.3. Aperture Corrections for Synthetic Scan Photometry	38
7. Conclusions	40
References	41
A Appendix A - Sensitivity Losses	43
A1. Scan Data	43
A2. Concurrent Data	51
A3. Published Data	59
A4. All Data	67
B Appendix B - Photometric Repeatability	75

1. Introduction

Installed on board the Hubble Space Telescope (HST) in 2009 as part of Service Mission 4, the Wide Field Camera 3 (WFC3) instrument is capable of high-resolution, direct imaging over a wide wavelength range. Equipped with both infrared and ultraviolet-visible (UVIS) channels, WFC3 is a workhorse enabling imaging from 200 to 1000 nm.

Characterizing how the two independent WFC3 charge-coupled devices (CCDs) change throughout the instrument’s lifetime is vital for instrument calibration and validation of scientific results, and thus for perpetuating the instrument’s utility for the wider scientific community. In this report, we investigate WFC3/UVIS photometric sensitivity using a non-standard, high-precision observing mode. We compare the reliability and quality of the resultant data to equivalent data from WFC3’s default observing mode that is historically used for absolute flux calibration of the instrument.

In the default staring mode of the WFC3/UVIS detector, the telescope is locked into position after target acquisition, making small adjustments over the duration of the exposure to maintain an exact pointing. The spatial scan mode was introduced in 2011 as an alternative observing mode for both the UVIS and IR detectors. In scan mode, the telescope moves in a commanded trajectory, either in straight lines or “boustrophedonic” multi-line scans; both options can be obtained at any permitted angle on the detector, at a constant rate chosen from a permitted range (McCullough, 2017). As a result, objects in the field are trailed across the detector, spreading their flux over many pixels. Figure 1 compares these two observing modes when implemented to image the star GRW+70D5824, using the F606W filter and UVIS2-C512C-SUB subarray.

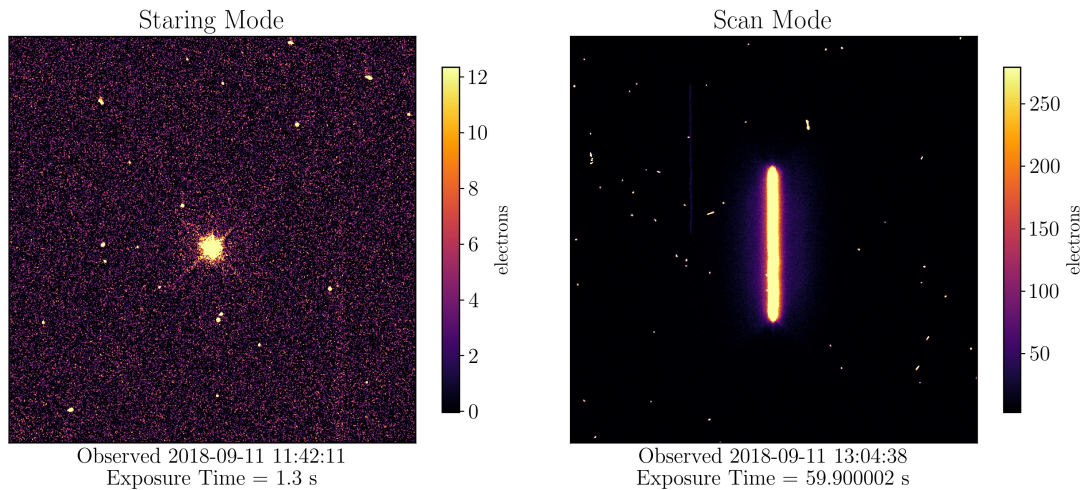


Figure 1: F606W observations of GRW+70D5824, taken on the UVIS2-C512C-SUB subarray. At left is a standard staring mode exposure; at right is a spatial scan. Plots were individually scaled using each image’s 50th percentile and 99th percentile as thresholds.

Depending on science goals, using the spatial scan mode instead of staring mode can be advantageous for several reasons. The full well limit for WFC3/UVIS varies spatially

across the detector and ranges from 63,000 to 72,000 electrons per pixel (Gilliland et al., 2010). Choice of observing mode will affect the optimal exposure times to avoid reaching the saturation limit for a given observation.

In staring mode, a star’s light is confined to the pixels in one area of the detector. Thus the saturation limit and maximum exposure time are governed by the brightness of the object being observed, since charge is accumulating only across those pixels of the detector whereupon the telescope has fixed the staring-mode point spread function.

In scan mode, charge is generated from the same amount of photons striking the detector as would be observed in staring mode, but over a greater number of pixels. This reduces the possibility of filling any given pixel’s full well, as well as reduces spatially-dependent sources of noise. With spatial scans, longer exposure times are therefore more easily accomplished without risking oversaturation, thereby increasing the overall signal of the object. Additionally, spatial scans reduce overhead time that would normally accrue when taking several, shorter exposures, allowing even more photons to be collected in an orbit.

Considering Poisson statistics, achieving 0.1% photometric repeatability requires collection of at minimum one million electrons such that signal-to-noise is equal to 1000. With scans’ shorter overhead and longer exposure times, collection of that many electrons is more feasible than the same goal for staring mode. The signal-to-noise for spatial scans was examined in Shanahan et al. (2017a); a single scan observation from a preliminary set resulted in higher photometric repeatability between visits, on the order of 0.1% between subsequent visits compared to 1% for staring mode.

However, spatial scans can present unique challenges for observers. When planning an observation with maximized exposure times, neighboring objects must be carefully considered to prevent contamination of star trails. Low-brightness and previously unseen objects especially pose a threat to accurate scans of target object, and may only be noticed after data is obtained. For a more thorough discussion on considerations for planning spatial scan programs, see McCullough & MacKenty (2012).

Even after successful observations, understanding spatial scan data can be a formidable task. At present, analysis of WFC3/UVIS spatial scans generally requires creation of custom data reduction software. Many existing data reduction tools cannot be easily leveraged for analysis of spatial scans because the vast majority of those tools were designed around the parameters and physics of staring mode observations.

Despite those challenges, observers have successfully used WFC3/UVIS in scan mode, characterizing exoplanet atmospheres (Fraine et al., 2021) and making high-precision measurements for Cepheid stars (Riess et al., 2014; Casertano et al., 2016).

The high-precision photometry enabled by the spatial scan mode also makes it an excellent observing strategy for monitoring the photometric stability of the instrument. Photometric monitoring has been done on a continual basis since the installation of WFC3 in 2009, as a standard component of the multitude of efforts to monitor and maintain instrument health.

Each cycle, two calibration programs were used to monitor the sensitivity of the two

UVIS CCDs. The “UVIS Contamination Monitor” was designed to look for the presence of contaminants on the optics by regularly monitoring (5x per year) the relative count-rates of two standard CALSPEC white dwarfs (GRW70 and GD153) in a key subset of ultraviolet and visible filters. Because the stability of these two standard white dwarf stars, GD153 and GRW+70D5824 (hereafter referred to as GRW70), is well-established (Bohlin et al., 2014; Bohlin et al., 2020), instrument sensitivity was evaluated by measuring changes in the count-rate of these objects over time.

The “WFC3 Photometry Monitor” is also designed to track the detector sensitivity using a larger set of CALSPEC standards observed once per year on each UVIS CCD and the IR detector, sampling nearly every available filter. These calibration data are used to derive the absolute photometric calibration, including zeropoints, encircled energies and color terms and are based on three CALSPEC white dwarf standards (GD153, GD71, GRW70) plus the G-type star (P330E).

Initially, the “UVIS Contamination Monitor” was limited to staring mode observations. In cycle 24, the six-orbit preliminary calibration program (Program 14878¹) was designed to test whether using spatial scans could improve the repeatability and therefore the precision in monitoring relative changes in sensitivity. Data from the first four visits was presented in Shanahan et al. (2017a). Initial results found that spatial scan photometric repeatability was on the order of 0.1% between subsequent visits compared to 1% for staring mode (Shanahan et al., 2017b). Based on these promising results, spatial scan monitoring was approved for future monitoring of the photometric stability, in addition to the staring mode observations for the same white dwarfs and other standard stars in different filter.

In this report, we present the results of several cycles of WFC3/UVIS spatial scan data from 2017 to 2021, across five total proposals. In a continuation of the analysis of Shanahan et al. (2017a), we compare the photometric repeatability of spatial scans to their counterpart data obtained in staring mode. We measure the changing photometric sensitivity across filters and their corresponding pivot wavelengths. We compare these results from staring mode observations over the same time period and also over the WFC3 lifetime.

¹Observing Program 14878: WFC3 UVIS contamination using spatial scans (McCullough et al., 2016)

2. Observations

This analysis includes five full cycles of WFC3/UVIS spatial scan data, spanning from March 2017 to December 2021. Table 1 gives an overview of this information, as well as additional observational parameters explained in Section 2.2..

Program	Cycle	CCD	Post-flash (e-)	Targets	Filters
14878	24	UVIS 1	0	GD153, GRW70	F218W, F225W, F275W, F336W, F438W, F606W, F814W
		UVIS 2	0, 12		
15398	25	UVIS 1	0	GD153, GRW70	F218W, F225W, F275W, F336W, F438W, F606W, F814W
		UVIS 2	0, 12		
15583	26	UVIS 1	0	GD153, GRW70	F218W, F225W, F275W, F336W, F438W, F606W, F814W
		UVIS 2	0, 12		
16021	27	UVIS 1	12	GD153, GRW70, <i>P330E</i>	F218W, F225W, F275W, F336W, F438W, F606W, F814W, <i>F390W</i> , <i>F475W</i> , <i>F555W</i> , <i>F625W</i> , <i>F775W</i>
		UVIS 2	12		
16416	28	UVIS 1	20	GD153, GRW70, <i>P330E</i>	F218W, F225W, F275W, F336W, F438W, F606W, F814W, <i>F390W</i> , <i>F475W</i> , <i>F555W</i> , <i>F625W</i> , <i>F775W</i>
		UVIS 2	20		

Table 1: Observation information and varying parameters for programs using spatial scans for UVIS photometric monitoring. Each CCD was paired with a specific subarray and output amplifier for all observations; that information is given in Section 2.2.1 but excluded from this table to avoid redundancy. The target and filters that are not used in this analysis are italicized and included for completeness.

We focus on a core set of seven wide-band filters: F218W, F225W, F275W, F336W, F438W, F606W, and F814W. These filters both have a sufficient number of observations across all five cycles and sample the spectrum adequately to measure any wavelength-dependent effects on throughput over time. Figure 2 shows the system throughput curves for these filters on UVIS 1 calculated as of installation.

Although the two most recent programs (Programs 16021² and 16416³) also included a limited number of observations of the G-type star P330E, we restrict our analysis to the two previously mentioned white dwarfs, GD153 and GRW70, which cover a much longer time baseline. Figure 3 depicts the composite spectral energy distributions (SEDs) from CALSPEC for the two white dwarfs (Bohlin et al., 2014; Bohlin et al., 2020).

²Observing Program 16021: WFC3 UVIS Time Dependent Sensitivity (Shanahan et al., 2019)

³Observing Program 16416: WFC3 UVIS Time Dependent Sensitivity (Calamida, 2020a)

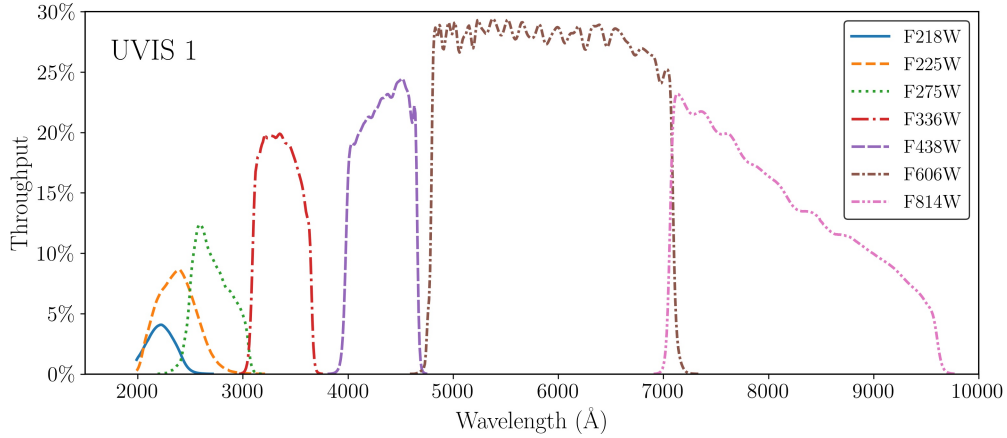


Figure 2: WFC3/UVIS 1 throughput curves for the seven filters utilized for this work.

2.1. Purpose and Scope of UVIS Photometric Monitoring Calibration Programs

Over time, the WFC3/UVIS photometric calibration programs have undergone significant changes in both the purpose and scope. Here we will discuss the major changes from cycle 24 to cycle 28, which are also summarized in Table 2.

Cycle	Program	Observing Mode	Orbits
24	14883	staring	11
	14815	staring	13
	14878	scan (preliminary)	11
25	14992	staring	11
	15398	staring	10
		scan	10
26	15582	staring	12
	15583	staring	10
		scan	10
27	16030	staring	20
	16021	scan	12
28	16415	staring	21
	16416	scan	12

Table 2: Summary of changes to UVIS photometric monitoring calibration programs from cycle 24 to cycle 28.

Previously, the main focus of the recurring WFC3/UVIS photometric calibration programs was to look for contamination, a specific mechanism causing sensitivity loss over time. As a result, the recurring calibration programs for cycles 24, 25, and 26 were designed to monitor both stability and possible contamination.

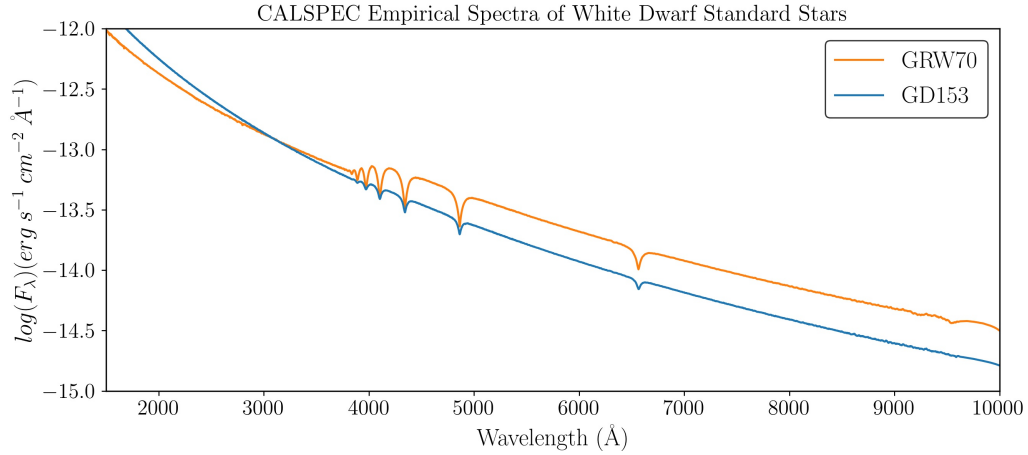


Figure 3: CALSPEC empirical spectral energy distributions for two spectrophotometric standard white dwarfs used in this work.

To this end, only dithered staring mode observations were taken during the cycle 24 WFC3/UVIS photometric calibration program (Program 14815⁴). During the same cycle, Program 14878 was executed to test the feasibility of photometric calibration using spatial scans. Based on the results from this initial exploratory program, half of the WFC3/UVIS contamination monitor orbits were allocated for spatial scans for both cycle 25 and 26 (Programs 15398⁵ and 15583⁶).

Optical contamination would be indicated by wavelength-dependent declining sensitivity rates in which bluer filters were more strongly affected. No evidence of contamination events in staring mode data was detected as of the publication of Shanahan et al. (2017b).

In the absence of evidence for contamination, the purpose of the recurring monitoring program was broadened to encompass the multitude of mechanisms that may cause sensitivity changes over time. By cycle 27, a baseline of high-quality spatial scan photometric results had been established across three programs of data. Combined, these factors led to partitioning of the WFC3/UVIS monitoring program, emphasizing spatial scans for monitoring relative photometric changes with a scan-specific program titled “WFC3 UVIS Time Dependent Sensitivity” (Program 16021 for cycle 27). A smaller subset of the UVIS staring mode visits were then grouped together with corresponding dithered IR observations in the separate calibration program “WFC3 UVIS and IR Photometry Monitor” (Program 16030⁷ for cycle 27). This ensures that we can continue the decade-long history of periodic staring mode observations as well as continue to assess how scan photometry compares to staring mode photometry. In cycle 28, as in cycle 27, UVIS spatial scans were observed as their own program (Program 16416) and UVIS staring mode observations were executed as part of a

⁴Observing Program 14815: WFC3/UVIS contamination and stability monitor (Baggett et al., 2016)

⁵Observing Program 15398: WFC3/UVIS Contamination Monitor (McCullough et al., 2017)

⁶Observing Program 15583: WFC3 UVIS Contamination Monitor (staring and scans)(McCullough et al., 2018)

⁷Observing Program 16030: WFC3 UVIS and IR Photometry Monitor(Calamida et al., 2019)

dual UVIS/IR photometry calibration program (Program 16415⁸).

2.2. Spatial Scan Observation Parameters

In this section, we discuss the varying parameters for spatial scan observations, the reasons for which they were chosen, and how the parameters have changed with time.

2.2.1 Subarray Apertures

The UVIS channel of the WFC3 instrument consists of two different charge-coupled devices (CCDs). As the CCDs are separate physical objects, monitoring changes to the UVIS detector requires a piecewise examination, treating the two chips (hereafter referred to as UVIS 1 and UVIS 2) as independent of each other. To study the changes in each chip’s sensitivity over time, scans were taken on one 512×512 subarray per chip (Figure 4). The UVIS 1 subarray is UVIS1-C512A-SUB, which uses output amplifier A; for UVIS 2, the subarray is UVIS-C512C-SUB, which uses output amplifier C. These corner subarrays were chosen specifically because their proximity to the read-out amplifier minimizes trails due to charge transfer efficiency (CTE) losses.

2.2.2 Post-flash

As of cycle 20, post-flash has been available for WFC3/UVIS observations to mitigate CTE losses, especially for sources with low signal-to-noise (Anderson et al., 2012; Sabbi & WFC3 Team, 2013). For calibration scans in cycles 24-26, UVIS 1 observations used no post-flash, and UVIS 2 observation used post-flash levels alternating between 0 and 12 electrons. After the execution of the cycle 26 program, no significant differences in repeatability between the unflashed and flashed data were detected, informing the decision to post-flash all scans for both UVIS 1 and UVIS 2 going forward. In cycle 27, the post-flash level was set to 12 electrons, and was raised to 20 electrons in cycle 28 following recommendations from Anderson (2020).

2.2.3 Filters and Targets

Beginning in Cycle 27, one calibration program was established specifically for UVIS spatial scans (See Table 2). At this point, one target and three filters were added to the program. Two orbits of 12 total were allocated to P330E, a G2 V CALSPEC standard star. The remaining ten orbits were then evenly split between aforementioned targets GD153 and GRW70. Three supplemental filters (F390W, F555W, and F775W) were used for spatial scans of GD153 and GRW70 when there was extra time in an orbit, otherwise prioritizing the core set of filters.

When planning these programs, visits were scheduled for every 4-6 weeks, alternating targets while working around limits in target visibility. For observations of P330E, visits were spaced out maximally. This cadence was maintained across cycle boundaries as best as possible.

⁸Observing Program 16415: WFC3 UVIS and IR Photometry(Calamida, 2020b)

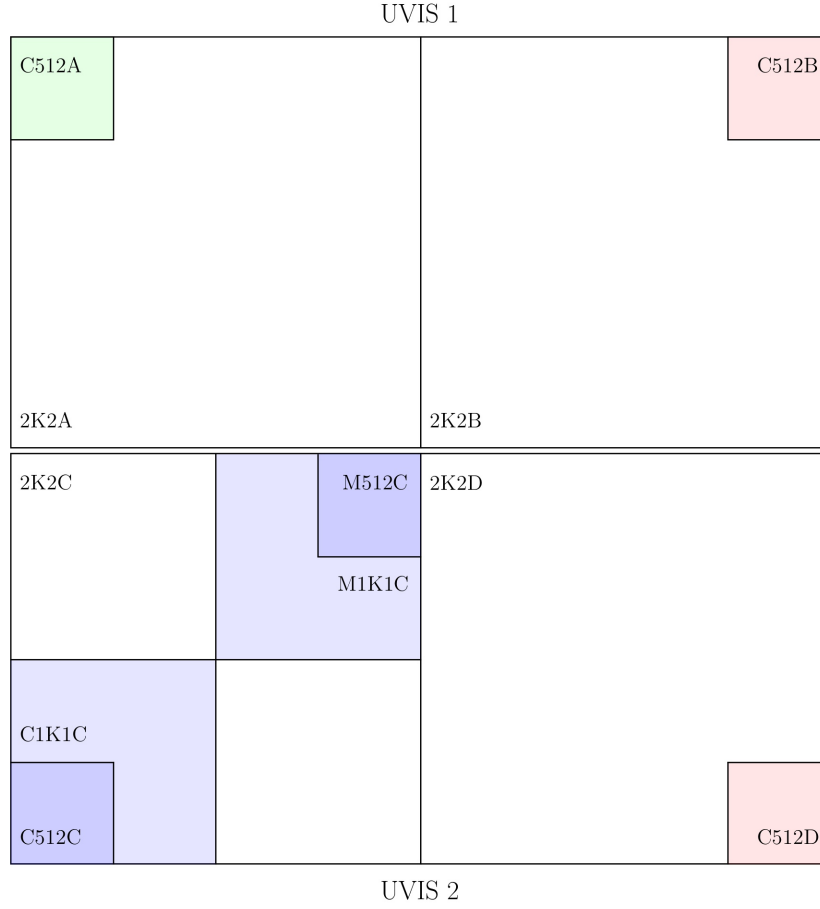


Figure 4: WFC3 UVIS subarray diagram, modeled after Figure 6.2 of the Cycle 30 WFC3 Instrument Handbook. All observations analyzed in this paper were taken on 512×512 subarrays UVIS1-C512A-SUB (green) and UVIS2-C512C-SUB (blue; lower left). While we only include staring mode data also taken on the aforementioned subarrays in our analysis, the calibration subarrays for output amplifier B and D (red) are labeled for the sake of completeness.

2.2.4 Scan Trajectory

Several observation parameters are identical across the entirety of the spatial scan data presented in this report, and were determined during the design of Program 14878. An initial visit during this exploratory program experimented with scan trajectory, resulting in the decision to utilize straight line scans, vertically oriented on the subarray at a slight ($< 1^\circ$) angle. Angling the scan samples the pixel phase, minimizing CTE losses, also known as charge transfer inefficiency (CTI). A run of the Hubble Space Telescope Exposure Time Calculator (HST ETC) determined an optimal exposure time of 60 seconds and a scan rate of 0.125 arcseconds per second. These values, independent of filter, target, and chip, were chosen to avoid saturation in the most sensitive configuration, while simultaneously producing enough signal in the less sensitive configurations.

3. Data

In this section, we discuss first how the data were obtained and calibrated, then explain each step of the data reduction process. A flowchart highlighting the reduction steps is presented in Figure 5.

3.1. Acquisition and Calibration

Scans were downloaded from the Barbara A. Mikulski Archive for Space Telescopes (MAST) by using the `astroquery` Python package.⁹ These images have been through the WFC3 calibration pipeline, `calwf3`, which applies basic astronomical data reduction steps including dark, bias, and flat-field corrections.

Our data products herein were calibrated with `calwf3` version 3.6.2¹⁰. A full description of `calwf3` 3.3 is presented in Ryan et al. (2016), which was the version utilized for analysis of Visit 01 from Program 14878 (McCullough, 2017). Updated reference files (IMPHTTAB, BIASFILE, FLSHFILE) were delivered in mid-2017 as part of the HSTCAL 1.1.0 release (`calwf3` 3.4) and implemented in the analysis of the first four visits of Program 14878 (Shanahan et al., 2017a). As we do not apply CTI correction for UVIS scans, the only relevant changes from subsequent release versions are bug fixes for the IMPHTTAB package and an update to enable chip- and time-dependent photometric corrections, both of which were included in the HSTCAL 2.5.0 release (`calwf3` 3.5.2)¹¹

For spatial scans, we use the “FLT” data products, which have gone through every necessary calibration step except for CTI correction. CTI quantifies the loss of photoelectrons during readout. Because the scans are bright, oriented perpendicularly to the serial readout direction, and obtained in subarrays close to the readout amplifiers, CTE losses are minimal. The end of the scan farthest to the readout amplifier may still suffer from some CTI, but a sufficiently large extraction box allows any trailed flux to be captured during aperture photometry. Furthermore, the CTI correction currently implemented in the `calwf3` pipeline is optimized for point sources, and has not yet been tested for scanned observations. This is our justification for the decision to use the FLT data products rather than the “FLC” CTI-corrected files.

A calibration program was executed in Cycle 29 to investigate the degree to which CTE losses impact staring mode observations of resolved objects (Program 16863); analysis of that data has not yet been released but is expected to help better parameterize CTE with regard to extended sources.

⁹`astroquery` (Ginsburg et al., 2019)

¹⁰`calwf3`

¹¹See Release HSTCAL 2.5.0

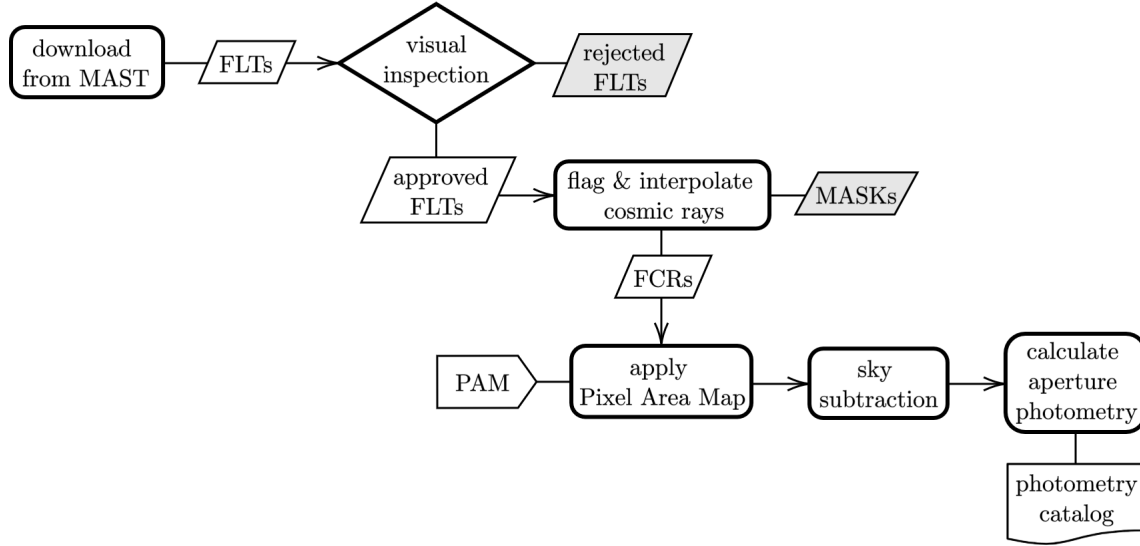


Figure 5: The data reduction process for spatial scans. Parallelograms signify image products; those that are gray are not used for analysis. Rectangles represent automated processes and the diamond represents a human decision-making step. The final products of the data reduction process are catalogs of aperture photometry.

3.2. Visual Inspection

Not every spatial scan FLT image of these calibrations was included in this analysis. We visually checked each scan to check for any major problems, and rejected a small number of them ($< 2\%$). For instance, some scans suffered from observing errors, resulting in unstable trajectories and crooked scans. Additionally, we only used spatial scans from Program 14878 that were vertically oriented on the subarrays, excluding the experimental boustrophedonic and horizontal scans. At present, the complexity of these scans’ analysis outweighs the additional scientific value of the scans.

One exposure (Program 16416, obsID “iegga9ieq”) included a satellite trail that passed through the sky background aperture; this FLT was individually processed by adapting tools from `acstools` satellite detection module¹² to create a mask. The uncorrected FLT was passed through the cosmic ray rejection routine (3.3.1) and PAM correction (3.3.2). The resulting FCR file was combined with the satellite mask prior to photometry being performed. Careful comparison of sky background statistics showed no significant deviations, and thus we have included it in our final dataset.

¹²`acstools`

3.3. Data Reduction

Photometry on the FLT images was performed with a multi-step processing pipeline written in Python, leveraging tools from several scientific data analysis packages including `astropy`¹³, `photutils`¹⁴, and `scipy`¹⁵. This pipeline contains steps for cosmic ray detection and repair in the images, source centroid detection, scan orientation determination, geometric distortion correction, background level estimation and subtraction, aperture photometry, and determination of photometric errors. An earlier version of this data reduction pipeline is described in Shanahan et al. (2017a).

3.3.1 Considerations for Cosmic Ray Rejection

Because the scanned star covers a significant portion of the detector compared to a normal staring mode PSF, the effect of cosmic rays on a scan is significant. Most of the scan trails suffer from cosmic ray hits. This introduces a non-negligible source of noise, decreasing repeatability between observations. Because of the significant impact of cosmic rays on this data, the calibrated, non-CTE-corrected files obtained via MAST are first processed with a custom cosmic ray detection and repair routine that is optimized for spatial scan data. Two additional files are generated for each FLT file ingested: a “MASK” file which marks the location of cosmic rays in the image, and a “FCR” file that is used to perform aperture photometry. Figure 6 compare an observation’s FLT and FCR files. The FLT has a noisier background than the FCR due to the abundance of cosmic rays. There is a larger population

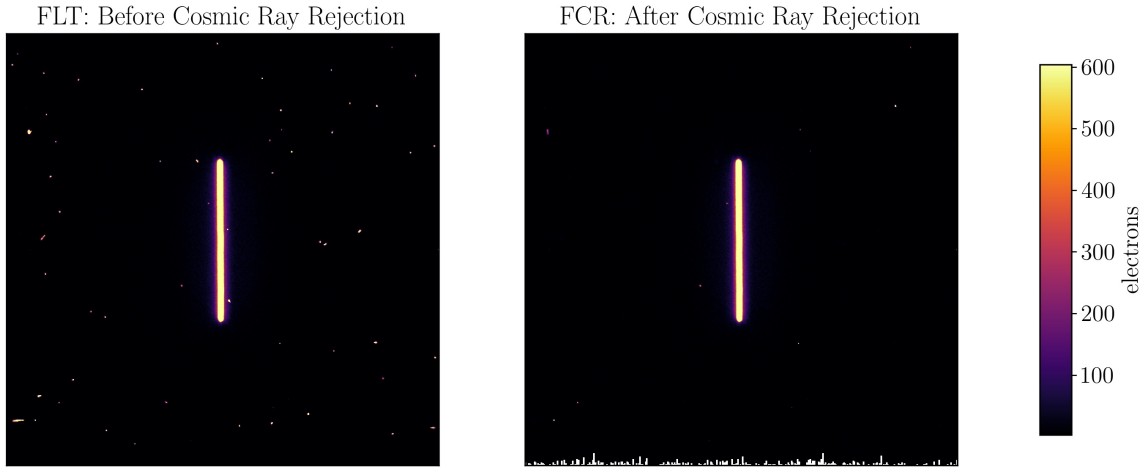


Figure 6: Left: `calwf3`-calibrated FLT image downloaded from MAST. Right: FCR file yielded after the FLT underwent the cosmic ray rejection routine. In each plot, data is in electrons and scaled using 50th percentile for the lower limit and the 99.5th percentile as the upper limit.

¹³`astropy` (Astropy Collaboration et al., 2013; Astropy Collaboration et al., 2018)

¹⁴`photutils` (Bradley et al., 2021)

¹⁵`scipy` (Virtanen et al., 2020)

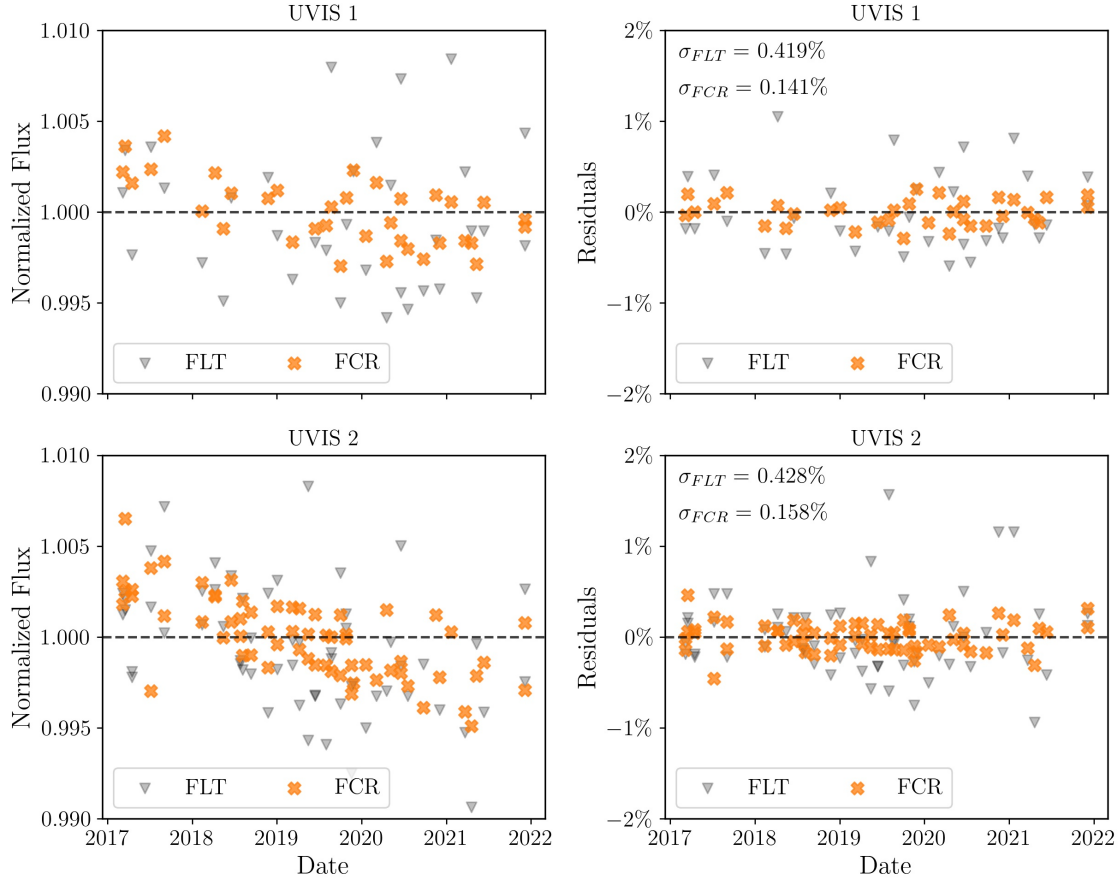


Figure 7: Comparing F814W photometry performed on GRW70 scans before (gray triangles) and after (orange crosses) the cosmic ray rejection routine. Left column: scan count-rates normalized to the data subset mean. Right column: residuals corrected for detector sensitivity with $1 - \sigma$ scatter listed. UVIS 1 data is in the top row, and UVIS 2 data is in the bottom row.

of bad pixels at the edges of the UVIS detector, which constrains the performance of cosmic ray identification and interpolation in that region. For spatial scans on UVIS 1 (Amp A), the affected area is the top edge of the subarray, while the bottom edge of the UVIS 2 (Amp C) subarray will be impacted (see 4). In Figure 6, a UVIS 2 spatial scan, the bottom edge of the FCR is lined with masked pixels where interpolation failed due to an excess of bad pixels and non-physical values.

Using cosmic ray rejection with correctly tuned detection parameters significantly reduces scatter in photometry, as illustrated in Figure 7. Identical aperture photometry routines were run on FLT (uncorrected for cosmic rays) and FCR (corrected for cosmic rays) scans of the target star GRW70 in the F814W filter for both CCDs. The photometric count-rates of the FLT files show a wide scatter, normalized to the data subset mean. In UVIS 1, the scatter of the FLT data is so significant that there appears to be no decline. For both CCDs, the FLT and FCR photometry were fit to slopes using linear regression. Plotted on the right are

the data corrected for time dependence. The residuals further confirm that implementing a validated cosmic ray rejection routine is essential for ensuring reliable and stable photometry between epochs.

3.3.2 Geometric Distortion

Both WFC3 detectors, IR and UVIS, are affected by geometric distortions such that the size of the pixels, and thus their capacity for recording charge, is a function of position on the detector. Larger pixels record more light than smaller pixels. Uncorrected, this leads to a gradient across the detector, as described in Kalirai et al. (2010). This is a serious concern when performing photometry: the measured total brightness of any given source will vary depending on where the light falls on the detector, up to 7.2% between both UVIS chips.

Drizzling is often implemented to counter the effects of distortion on photometry and image appearance; for example, one could combine multiple FLTs into a “DRZ” file that is “flat” across the field. However, it is not necessary to drizzle scans to remove the geometric distortion; instead, FLTs can be multiplied by the UVIS pixel area map (PAM) (Figure 8). By applying this field-dependent factor, any given source in a PAM-corrected FLT image will yield a count-rate equivalent to what would have been achieved with drizzling (Deustua et al., 2017a).

Thus, we apply the PAM to the FCRs, which are FLTs that have been corrected for cosmic rays. Point source and scanned photometry measurements from FLT images will differ depending on where the source falls on the detector, but it is important to note that the *sky* brightness of FLTs should not be significantly impacted by geometric distortion. Those files have been flat-fielded, so the sky is a uniform surface brightness. Additionally, the gradient of distortion across the subarrays used for these calibration scans is only $\sim 1\%$. Therefore, the cosmic ray rejection routine can safely be implemented before the application of the PAM.

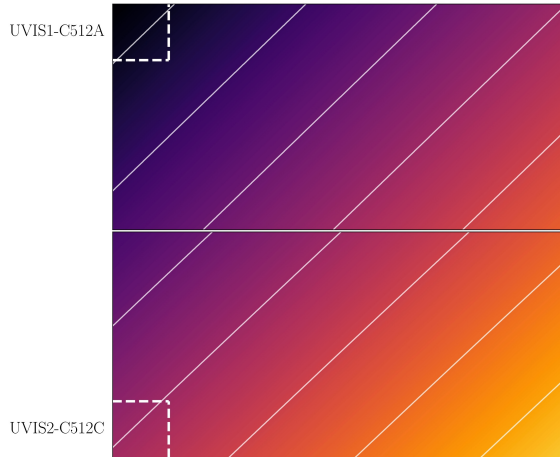


Figure 8: The UVIS pixel area map, with gradient lines at every 1% deviation, beginning with 0.97% in the top left corner and concluding with 1.03% in the bottom right corner. Adapted from Fig 1 of Kalirai et al. (2010). The position of the subarrays used for this analysis are marked with dashed lines and labeled.

3.3.3 Sky Subtraction

To calculate the background sky level, a 30-pixel-wide rectangular “rind” was drawn around the scan, as depicted in Figure 9. Fine-tuning the size of the background aperture rind is important in order to limit capturing flux from the scan itself.

Since the scans are oriented vertically on the subarray, the background aperture must be sufficiently wide to avoid the excess light radiated outwards from the sides of the scans. The background aperture must also be sufficiently long to avoid encapsulating light from either end of the scan. Simultaneously, the background aperture rind must not be too long; the scans themselves are approximately 192 pixels long, and they are not always perfectly centered on the 512×512 sub-array. Thus, if the background aperture is too tall and the scan is offset vertically, it may end up off-frame.

Ultimately, the optimal size of the inner boundary was determined to be 300 pixels wide and 400 pixels tall, oriented relative to the centroid of the scan. At 30 pixels in thickness, the outer boundary is thus 360 pixels wide and 460 pixels tall. This distance ensures minimal contamination of the scan flux in the measurement of the sky flux.

It should be noted that this is a departure from the approach taken in Shanahan et al. (2017a), in which sky background was calculated using a larger rind with an inner boundary of 75×400 , encompassing the rest of the subarray up to 10 pixels from the edge. During the course of this newer analysis, which included significantly more data than was available in 2017, testing suggested that there still exists significant flux from the scans at a distance of 75 pixels. This was the motivation to reconsider the parameters for sky subtraction.

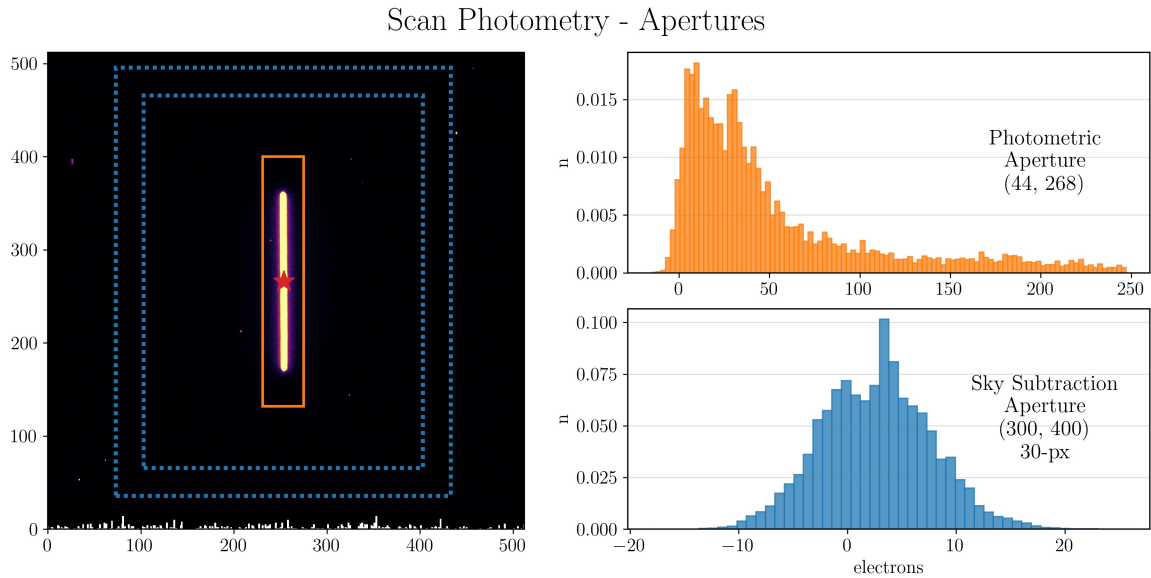


Figure 9: The same spatial scan depicted in Figure 6. On the left, the centroid of the scan (red star), the photometric aperture (orange box), and the sky subtraction rind (blue dotted frame) are plotted over the image. Histograms on the right plot the pixel values in the photometric aperture (top) and sky subtraction rind (bottom).

3.3.4 Aperture Photometry

Optimizing the aperture with which to measure the flux of the scan itself is a complex process. Staring mode photometry is able to take advantage of radial symmetry of the photometric aperture, but spatial scans require rectangular apertures to encapsulate the flux of the line spread function.

In Shanahan et al. (2017a), four aperture widths (16, 30, 40, and 70 pixels) were tested while holding aperture height constant at 250 pixels. The primary motivation for aperture testing was quantifying potential repeatability for scan photometry. For each aperture, the ratio between measured flux for identical observations from Program 14878 Visit 3 and Visit 2 was taken. Repeatability suffered most significantly in the largest aperture, 70×250 , likely due to additional sky noise.

As a test case, using Cycle 29, UVIS 2 data, we performed two rounds of parallel aperture photometry across 100 aperture combinations: 70 varying width, and 30 varying height. When varying width, we used a constant aperture height of 268 pixels. The optimal width was determined to be 44 pixels, and was used as the constant width when testing aperture height. The final, optimal aperture was determined to be 44×268 . All 57 exposures from Program 16416 underwent cosmic ray rejection, PAM correction, and background sky subtraction. The centroid of each scan was identified, and calculations were performed for each aperture combination.

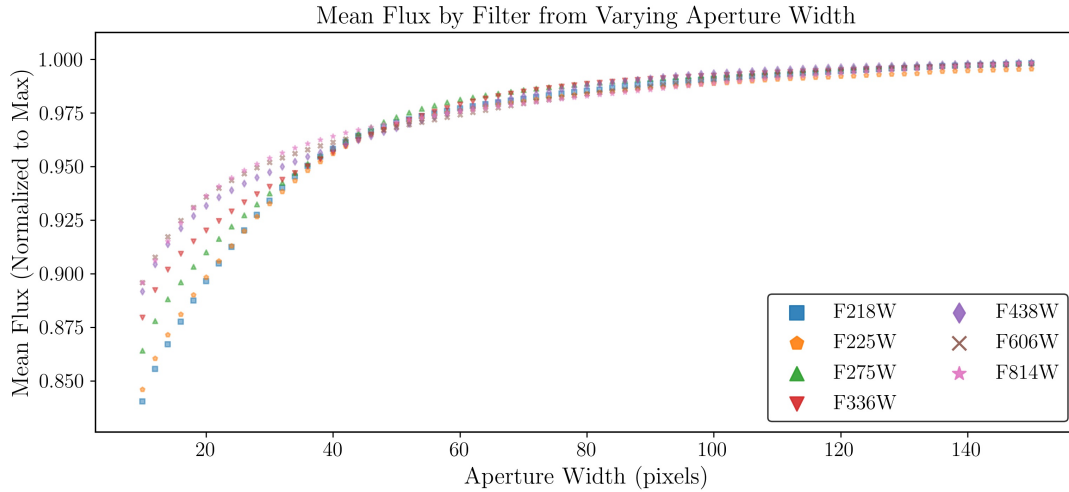


Figure 10: Program 16416 photometry of GRW70 on Amp C (UVIS 2) for varying aperture widths. Aperture length was held constant, at 268. Every scan was normalized by its flux at the largest aperture, 150×268 . The max-normalized mean of all scans for each aperture is plotted by filter.

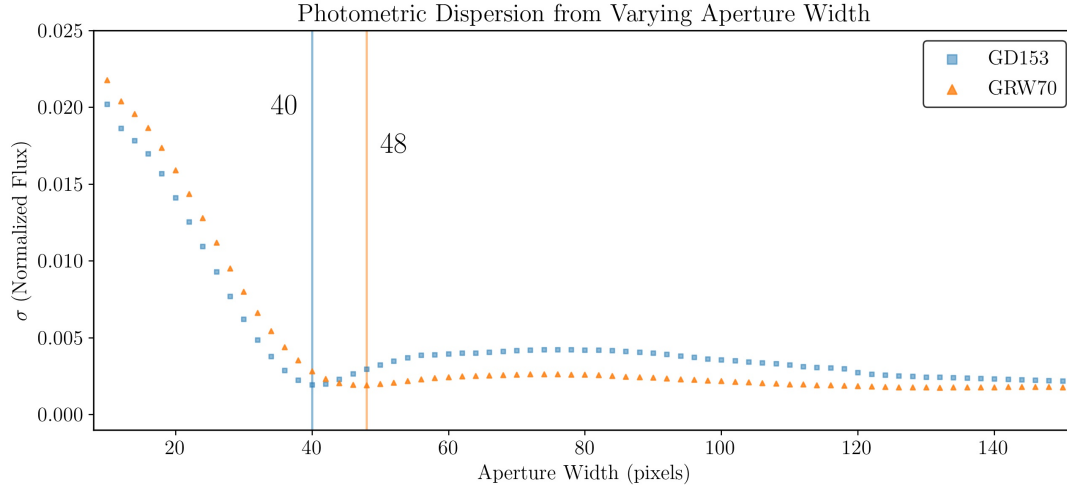


Figure 11: Dispersion of filter-aggregated max-normalized flux by aperture width, from Program 16416 on Amp C (UVIS 2), for both GRW70 and GD153. At each aperture width, the max-normalized fluxes (used to produce mean values plotted in Figure 10) from all seven filters were combined into one data set, and the standard deviation calculated. For each target, the first minimum is plotted as a vertical line and labeled with the aperture width.

Testing Aperture Width

Width-varying apertures were examined first. Data were divided according to target, and then normalized with respect to the flux in the largest aperture (150×268). As an example, Figure 10 shows the mean normalized flux values at each aperture width for GRW70, broken down by filter. This approximation of enclosed energy demonstrates the fact that as aperture initially increases, the amount of flux captured in the aperture increases - but it does so at different rates across wavelengths/filters.

From Figure 10, it can be seen that using too narrow of an aperture has wavelength-dependent consequences. The ideal aperture should be a point where all filters receive the same relative amount of light; in Figure 10 this would be a point where the filter curves join together. However, using too large an aperture would include too much background noise, reducing repeatability. To identify the optimal aperture width, we combine relative data from all seven filters into two, target-specific datasets and find the standard deviation at each aperture. They are plotted together in Figure 11.

As aperture increases, the flux in each filter increases at a different rate, ultimately approaching unity. For each target, we find the first local minimum, corresponding to the smallest aperture with the lowest dispersion between the filters. These local minima are labeled in Figure 11. We take the median of the local minima, 44, as our optimal aperture width.

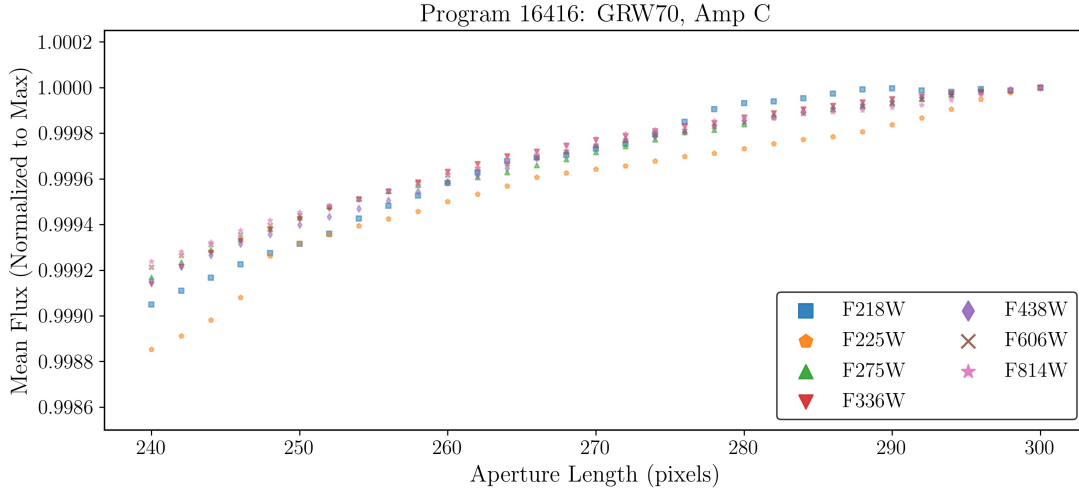


Figure 12: Program 16416 photometry of GRW70 on Amp C (UVIS 2) for varying aperture heights. The optimal aperture width, 44, was used. Every scan was normalized by its flux at the largest aperture, 44×300 . The max-normalized mean of all scans for each aperture is plotted by filter.

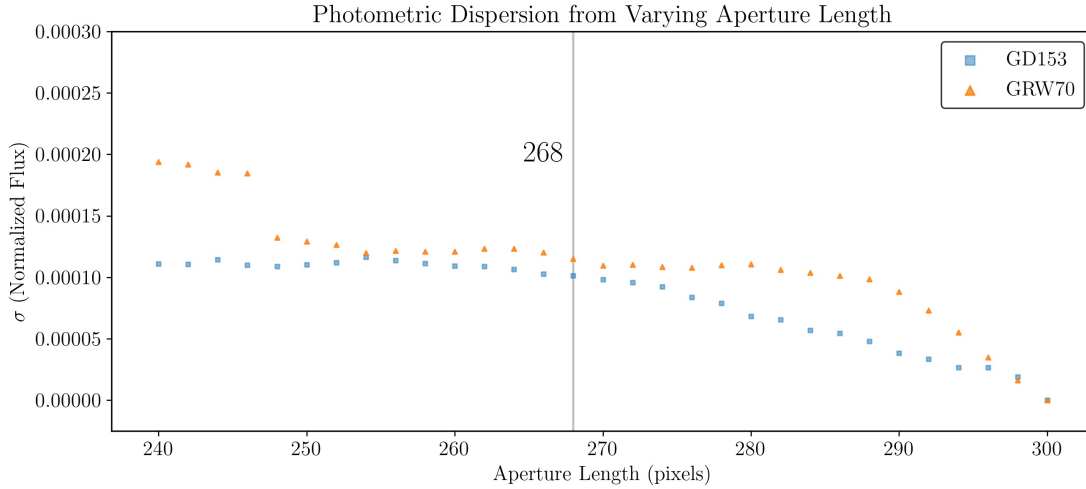


Figure 13: Dispersion of filter-aggregated max-normalized flux by aperture height, from Program 16416 on Amp C (UVIS 2), for both GRW70 and GD153. At each aperture height, the max-normalized fluxes (used to produce mean values plotted in Figure 12) from all seven filters were combined into one data set, and the standard deviation calculated. The aperture height held constant during aperture width testing is marked as a gray line.

Testing Aperture Height

Using the determined aperture width, we tested 30 aperture heights from 240 pixels to 300 pixels. For each exposure, we normalized the flux by that of the maximum aperture. Figure 13 shows aggregated data for GRW70 - in each filter, and at each aperture, the mean normalized value is plotted.

The height-varying enclosed energy curves did not vary as significantly between filters as those for the width testing. When comparing both the scale and shape of Figure 13 to the width-varying photometry (Figure 10), it seems that the range of heights used largely excludes the regime where the amount of captured light is greatly affected by filter choice. The dispersion of the height-testing data quantifies this: following the methods used to determine the optimal aperture width, we take the standard deviation for each target’s filter-combined max-normalized data, presented in Figure 13 along with a vertical line signifying the standard aperture height used for testing aperture widths, 268 pixels. The dispersion of the majority of tested aperture heights was on the order of 0.01%. On this basis, we kept 268 as our optimal aperture height.

Having determined our optimal aperture, the remaining data were processed, returning catalogs of scan aperture photometry.

3.4. Staring Mode Data

As a basis of comparison, we also utilize catalogs of staring mode photometric data. WFC3/UVIS staring mode calibration observations cover 13 years and include several filters and five targets. Sensitivity losses identified from this dataset were presented in Khandrika et al. (2018) and Calamida et al. (2021c).

We define three distinct staring mode datasets. For each, data were restricted to staring mode observations of GD153 and GRW70 on UVIS1-C512A-SUB and UVIS2-C512C-SUB using the core set of seven filters.

- **Concurrent:** For optimal comparison to scan photometry, we define the dataset “Concurrent” to data collected from 2017 to 2021, thus matching the time period over which the scan mode data were taken. This dataset contains a total of 1114 observations.
- **Published:** To compare our rates of detector sensitivity change to those published in Calamida et al. (2021c), we define the dataset “Published” as data collected through November 2019. For filters F218W, F225W, F275W, only observations after MJD = 55738 are included. In total, this dataset contains 3056 observations.
- **All:** Finally, we include all staring mode data available through the end of 2021 in a dataset named “All”. As with the Published dataset, UV observations before MJD = 55738 are excluded. In total, this dataset contains 3291 observations.

Detailed photometric data and plots can be found in Appendix A. Specifically, see Section A2. for the Concurrent dataset, Section A3. for the Published dataset, and Section A3. for the All dataset.

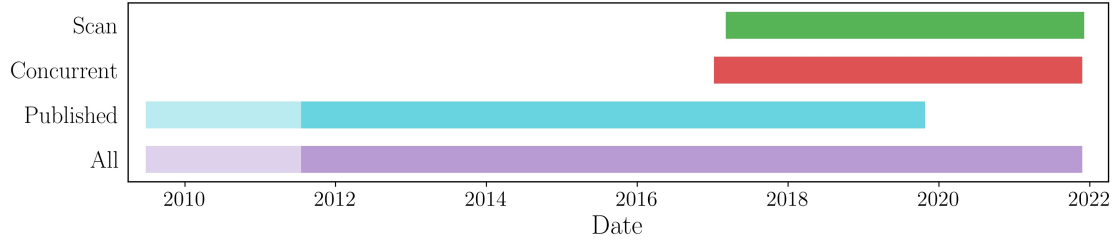


Figure 14: The timespan for the four named datasets. For the Published and All dataset, data from UV filters begin in mid-June 2011. Dataset sizes and outliers are tabulated in 3.

Staring mode photometry was performed on CTE-corrected files, or FLCs, and multiplied by the PAM to correct geometric distortion. No cosmic ray rejection was performed because of the difficulty of properly identifying and masking cosmic rays in individual FLCs under these observing conditions; instead, sigma-clipping was used to remove any contaminated exposures. The photometric aperture radius was set at 10-pixels, the standard radius used for WFC3/UVIS staring mode photometry. At that radius, airy ring “breathing” does not significantly affect the star’s encircled energy (Sabbi & Bellini, 2013; Khandrika et al., 2018). Median background was subtracted using a sky annulus from 150 to 200 pixels.

4. Analysis

Our goals are to determine the rate of change for the WFC3/UVIS detector using scans taken on the corner subarrays and to assess the photometric repeatability of WFC3/UVIS spatial scans. With regards to both goals, it is of particular interest to compare the performance of a non-standard observing mode to staring mode within the context of calibration work, thus staring mode data were analyzed in an identical manner to scan mode data.

For each dataset, 28 subsets were defined by the unique combinations of observation CCD, target, and filter. Within each subset, linear regression was used to identify data points greater than 3σ from the mean. The total number of outliers across the Scans dataset was 7 (0.99%). There were 9 total staring mode outliers in the Concurrent dataset (0.81%), 42 outliers in the Published dataset (1.37%), and 47 outliers in the All dataset (1.43%). These values are compiled in Table 3.

Dataset Name	Observation Mode	Timespan	n_{total}	$n_{outlier}$	n
Scan	spatial scan	2017 – 2021	706	7	699
Concurrent	staring	2017 – 2021	1114	9	1105
Published	staring	2009* – 2019	3056	42	3014
All	staring	2009* – 2021	3291	47	3244

Table 3: Dataset names, sizes, and outliers; n represents the number of observations retained for analysis after sigma-clipping ($n_{total} - n_{outlier}$). *For the filters F218W, F225W, F275W, data before mid-2011 was excluded.

Outliers were removed from the analysis pipeline, and a new subset mean count-rate was calculated. Data were normalized to this value, enabling us to compare relative change across subsets of data, as well as pool results across targets and filters in order to determine overall trends.

4.1. Instrument Sensitivity

WFC3/UVIS photometric sensitivity changes with time (Gosmeyer & Baggett, 2016; Shanahan et al., 2017b; Khandrika et al., 2018; Calamida et al., 2021c). Our first analysis objective was to quantify changes in UVIS count-rates over time solely using spatial scans, then compare our findings to staring mode data.

With each chip/filter/target subset of normalized scan data, we used `scipy` to perform a linear regression, fitting the data to a line (Equation 1) and computing the rate of change in the photometric sensitivity over time. This rate was calculated according to Equation 2. Error in the linear fit of the slope was calculated according to Equation 3.

This resulted in 28 individual rates across each subset, which are provided in Tables A1 and A2 along with sample size and the standard deviation of normalized data. Next, normalized data from each target were pooled together to determine chip-specific sensitivity

$$y(t) = m \times t + y_0 \quad (1)$$

Equation 1: A line of best fit, calculated from a linear least-squares regression, is used in this work to describe how the UVIS detector's sensitivity ($y(t)$, mean-normalized count-rates) changes with time (t , years). The slope of this line is m and y_0 is the y-intercept.

$$m = \frac{\sum (t_i - \bar{t})(y_i - \bar{y})}{\sum (t_i - \bar{t})^2} \quad (2)$$

Equation 2: Calculation of the slope (m) of the line of best fit (Equation 1), which represents the rate of photometric change in normalized count-rate per year. Here, \bar{t} is the mean time and t_i is the i th observation time. Since count-rate is normalized to the mean, y_i is the i th mean-normalized count-rate and \bar{y} is equal to 1.0.

$$m_{err} = \sqrt{\frac{1 - r^2}{n - 2} * \frac{\sum (y_i - \bar{y})^2}{\sum (t_i - \bar{t})^2}} \quad (3)$$

Equation 3: Calculation of m_{err} , the standard error of the slope. Here, r is the correlation coefficient and n is the number of observations. As in Equation 2, m is the slope, \bar{t} is the mean time, t_i is the i th observation time, n is the number of observations, y_i is the i th mean-normalized count-rate, and \bar{y} equals 1.0.

losses for all seven filters, producing 14 total slopes as seen in Table 4. Finally, we calculated overall rates of instrumental sensitivity decline per year for each UVIS CCD.

After this was done for the scan mode data, the same process was performed for the normalized staring mode datasets (Concurrent, Published, and All).

4.2. Photometric Repeatability

Shanahan et al. (2017a) examined experimental spatial scans and found the repeatability between identical visits to be on the order of 0.1%, ten times more precise than staring mode's 1.0% repeatability (Shanahan et al., 2017b).

To assess the repeatability of spatial scans across five years of data, we remove the overall time dependence of the mean-normalized data and examine the scatter of the residuals. As with our analysis of changing instrumental sensitivity, we complete this process for all four sets of data: Scan, Concurrent, Published, and All. Within each dataset, scatter is calculated for all 28 unique combinations of chip, filter, and target. Next, target data are combined, and scatter is calculated for each filter on each chip. Finally, data across filters is combined to evaluate the scatter for each UVIS chip.

5. Results

5.1. Instrument Sensitivity

Spatial scan data from 2017 to 2021 confirm that UVIS photometric sensitivity is declining with time. The mean-normalized flux over time in F218W is displayed in Figure 15 as an example. As explained in Section 4.1., data have been sigma-clipped, normalized to their subset mean (where a subset is the unique combination of chip, filter, and target), and fit to a slope, which is included in the plot legends. The overall F218W rate for the UVIS 1 CCD, displayed in the bottom right corner, was calculated by performing linear regression on subset-mean-normalized data from both targets.

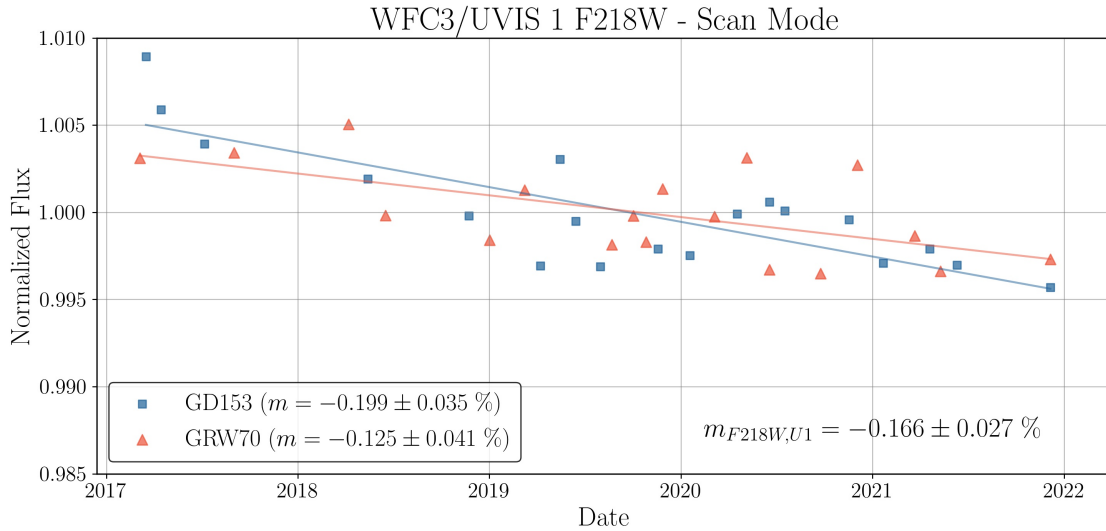


Figure 15: F218W Scan photometry of GD153 (blue squares) and GRW70 (orange triangles) on UVIS 1, showing temporal trends in photometric sensitivity. Data are count-rates (electrons/s) normalized to the target mean count-rate (electrons/s). This plot is duplicated in Appendix A as Figure A1. For F218W UVIS 2, as well as plots for all other core filters, see Figures A2 - A14. Figures A15 - A28 are equivalent plots for the Concurrent data set, Figures A29 - A42 are equivalent plots for the Published data set, and Figures A43 - A56 are equivalent plots for the All data set.

Can a linear slope well characterize the temporal photometric sensitivity of the detector? Let's take a moment to establish that a linear approximation is more appropriate to describe the photometric sensitivity change of the detector over the timescales at hand than an alternative explanation like exponential decay.

Fitting normalized photometry with least-squares regression results in a line as defined in Equation 1, where m is the slope and y_0 is the intercept, such that some time t yields a normalized count-rate $y(t)$. This is a linear approximation for an exponential like Equation 4. With such an exponential, we can write a second-order Maclaurin expansion, and substitute

m for $-y_0\tau^{-1}$ (Equation 5).

$$y(t) = y_0 e^{\frac{-(t-t_0)}{\tau}} \quad (4)$$

Equation 4: An exponential function to compare to our linear fit (1) for the relationship between detector sensitivity and time. Here, τ is some time constant.

$$\begin{aligned} y(t) &= y_0 - y_0 \frac{t - t_0}{\tau} + \frac{1}{2} y_0 \left(\frac{t - t_0}{\tau} \right)^2 \\ &= y_0 + m (t - t_0) + \frac{1}{2} \frac{m^2}{y_0} (t - t_0)^2 \end{aligned} \quad (5)$$

Equation 5: A second-order Maclaurin expansion of the exponential defined in Equation 4.

Note that together, the first two terms of Equation 5 comprise the line of best fit from the least-squares regression. If the second order term is significant, then that would suggest that an exponential function would better fit the relationship between time and detector sensitivity. Thus, we isolate the second order term to test how appropriate a linear fit is for this data. Normalizing count-rates to their mean over a five-year period gives us a y_0 of 1 at $t - t_0 = 2.5$ years. As an example, these values with a calculated rate of -0.2% per year (typical of the results in this work) results in a second order term of $1.25 \times 10^{-5}\%$. We consider this contribution insignificant, and conclude that a linear fit well describes the detector sensitivity changes over this time scale.

$$\begin{aligned} \frac{1}{2} \frac{m^2}{y_0} (t - t_0)^2 &= \frac{1}{2} \frac{(0.2\%/yr)^2}{100\%} (2.5\text{ yr})^2 \\ &= 1.25 \times 10^{-5} \% \end{aligned} \quad (6)$$

Equation 6: For an example slope of $0.2\%/year$ (typical of rates calculated in this analysis) measured over five years using mean-normalized photometry, we find the difference between the exponential and the first order approximation to be negligible.

Next, the presentation and interpretation of the results contained herein require a few caveats. In regression analysis, error calculation assumes that the error of the underlying data is normally distributed. This is not necessarily true for our data - certain proposals and observing epochs are associated with errors clustered at discrete values. Consequently, the standard error (Equation 3) is likely underestimated, although the least-squares calculation of the slope (Equation 2) is unaffected. Thus, we include the error as a measurement of the goodness of a fitted slope, with the caveat that it is likely underestimated due to non-Gaussian errors and underlying systematics. The complexity of characterizing such systematics would hinder further analysis.

The filter-specific rates of change from spatial scan photometry are listed in Table 4. Figures 16 and 17 plot the percent change in relative photometry per year as a function of filter pivot wavelength for the Scan and Concurrent datasets (scan mode and staring mode photometry from 2017 to 2021, respectively). The error in the linear fit of the slope was calculated according to Equation 3 and plotted as error bars.

CCD	Filter	n	$m \pm m_{err}$ (%/yr)
UVIS 1	F218W	37	-0.166 ± 0.027
	F225W	37	-0.096 ± 0.026
	F275W	38	-0.165 ± 0.023
	F336W	40	-0.110 ± 0.015
	F438W	37	-0.116 ± 0.016
	F606W	38	-0.089 ± 0.009
	F814W	35	-0.091 ± 0.021
UVIS 2	F218W	59	-0.138 ± 0.021
	F225W	62	-0.202 ± 0.013
	F275W	65	-0.206 ± 0.013
	F336W	63	-0.154 ± 0.013
	F438W	63	-0.195 ± 0.011
	F606W	62	-0.189 ± 0.010
	F814W	63	-0.123 ± 0.016

Table 4: Filter-dependent sensitivity rates for UVIS 1 and UVIS 2 as derived from **spatial scans** of two white dwarf standards (GD153 and GRW70) spanning five years (2017-2021).

diverging target-specific rates, Scan data appears to agree well with one target over the other. On UVIS 2 (Amp C), the F606W slope for Concurrent observations of GRW70 is instead much shallower than the Concurrent GD153 slope and the Scan slopes for both targets. On UVIS 1 (Amp A), GRW70 Concurrent rates appear significantly deeper than GD153 Concurrent rates in filters with pivot wavelength $< 5000\text{\AA}$; Scan data for both targets is clustered near the calculated Concurrent rate for GD153. An examination of the normalized photometry for UVIS 1 Concurrent data (Figure A15, reproduced here as Figure 18, as well as Figures A17, A19, A21, A23, A25, and A27) shows that the most recent UVIS 1 staring mode observations for GRW70 are responsible for this effect.

In the Scan data, the measured rate of decline in photometric sensitivity over five years is less than -0.25% per year for all targets and filters. Rates calculated for each target agree well with each other for each filter and on both chips. There is generally good agreement between the target-specific sensitivity loss rates across both CCDs and all filters. Photometric sensitivity appears to be declining more rapidly for UVIS 2, as evidenced by deeper slopes in all core filters besides F218W. Using spatial scans alone, we find overall sensitivity rates of $m_{\text{UVIS 1}} = -0.119 \pm 0.008\%/ \text{year}$ and $m_{\text{UVIS 2}} = -0.172 \pm 0.005\%/ \text{year}$.

How well do these data compare to staring mode data from the same time period? A comparison of the Scan and Concurrent data reveal a few insights. In each filter, error in the Concurrent dataset is larger than error calculated for scan data, though they were calculated in an identical manner. In filters where the Concurrent data results in

$$s = \frac{\sigma_e}{\sqrt{n}} = \frac{\sqrt{\frac{\sum (y_i - \bar{y})^2}{n-2}}}{\sqrt{n}} \quad (7)$$

Equation 7: Estimation of the standard error (s) of the filter- and chip-specific sensitivity rate calculated for each dataset. Here, σ_e is the standard deviation.

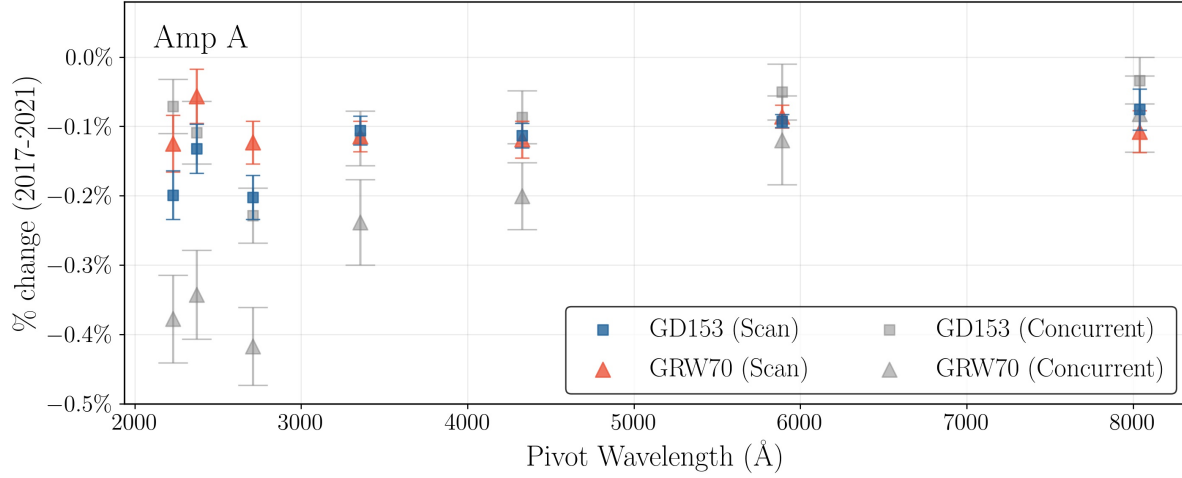


Figure 16: WFC3/UVIS 1 (Amp A) sensitivity losses per year for each target, by pivot wavelength of filter, from 2017 to 2021. Rates derived from **scan mode data** are shown as blue squares (GD153) and orange triangles (GRW70), and are listed in Table A1. Rates derived from **staring mode data** (Concurrent data set) are shown as gray squares (GD153) and gray triangles (GRW70), and are listed in Table A3.

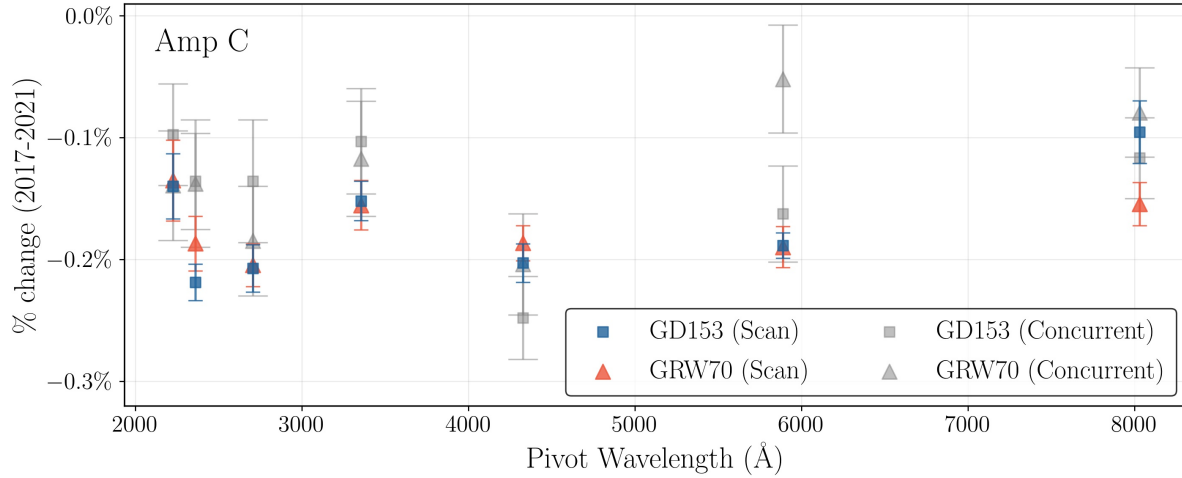


Figure 17: Like Figure 16, but for WFC3/UVIS 2 (Amp C). Scan rates per target are listed in Table A2, and equivalent rates for the Concurrent staring mode data set are listed in Table A4.

Having examined the difference between staring mode and scan mode photometric losses over the *same* time period, we now turn our attention to examine sensitivity loss rates derived over greater timespans. Figures 19 and 20 plot the photometric sensitivity rates for each of the four datasets (Scan, Concurrent, Published, and All), calculated from GD153 and GRW70 data only. Previously established rates from Calamida et al. (2021c) are plotted as

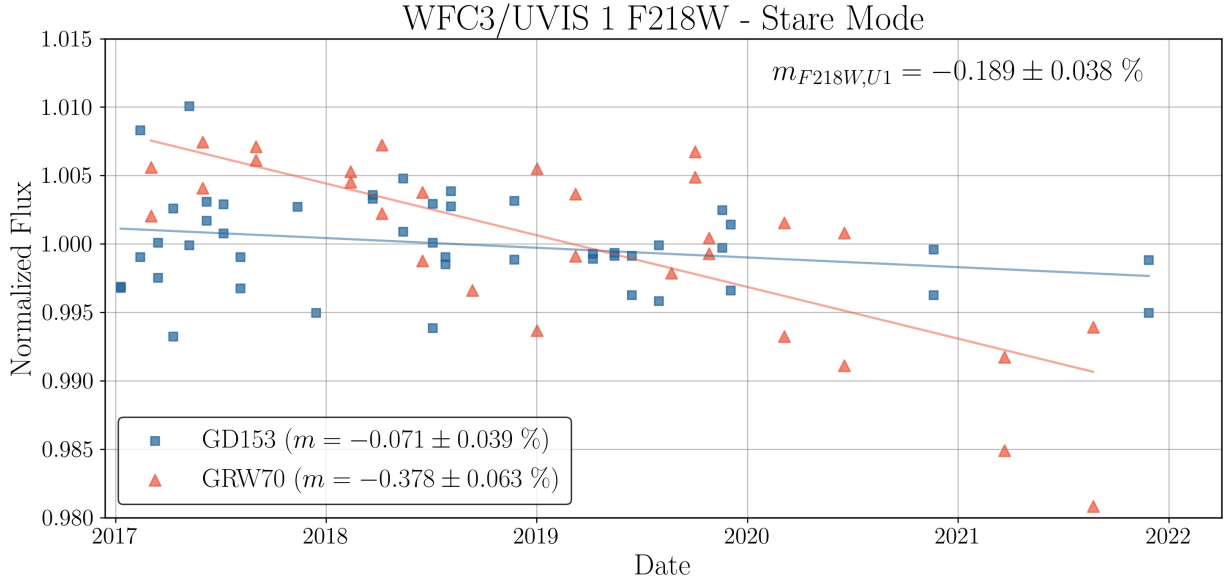


Figure 18: UVIS 1 (Amp A) F218W photometry for Concurrent data. Recent observations of GRW70 recorded much lower flux relative to the mean than the equivalent normalized flux for GD153. This contributes to GRW70’s much steeper slope, and drives the overall slope for this filter down.

a gray horizontal bar. For each dataset, the standard error for the filter-specific sensitivity rate is calculated as standard deviation of the residuals divided by the square root of the number of data points (Equation 7). In Figures 19 and 20, error is plotted as a shaded box to preserve legibility. In Figures 21 and 22, error bars in each filter are mapped horizontally and scaled individually to better show the spread of the data.

Calamida et al. (2021c) presented time-dependent inverse sensitivities for all 42 filters for the WFC3/UVIS instrument by using staring mode and scan mode observations of five total targets to assess the sensitivity loss rate of the CCDs between installation and the current epoch. Single linear fit slopes were calculated using photometry from 2009 to November 2019 for all but five ultraviolet filters, which experienced increased sensitivity for the first two years of instrument life (noted regarding WFC3/UVIS in Shanahan et al. (2017b) and Khandrika et al. (2018), as well as for HST/STIS in Carlberg & Monroe (2017)). For these five filters¹⁶, two slopes were calculated, delineating between eras using MJD = 55738. We include only the later published rate, calculated using data from mid-2011 to November 2019, in our comparative analysis.

As a reminder, all data in the Published set were used in Calamida et al. (2021c), and yet the rates are not identical. Thus we can see how including additional targets and early scan data affects the calculation of photometric decline by comparing the rates from Calamida et al. (2021c) to the rates yielded when restricting that data to only GD153 and GRW70,

¹⁶These five filters are **F218W**, **F225W**, **F275W**, F280N, and F300X. The first three are included in the core set of filters for this spatial scan analysis.

which are plotted as cyan crosses. In most cases, there is still generally good agreement, which suggests that while the inclusion of other targets potentially could result in more robust results, the three additional targets used by Calamida et al. (2021c) evidently do not cause their results to differ significantly from those we derive here from GD153 and GRW70 alone.

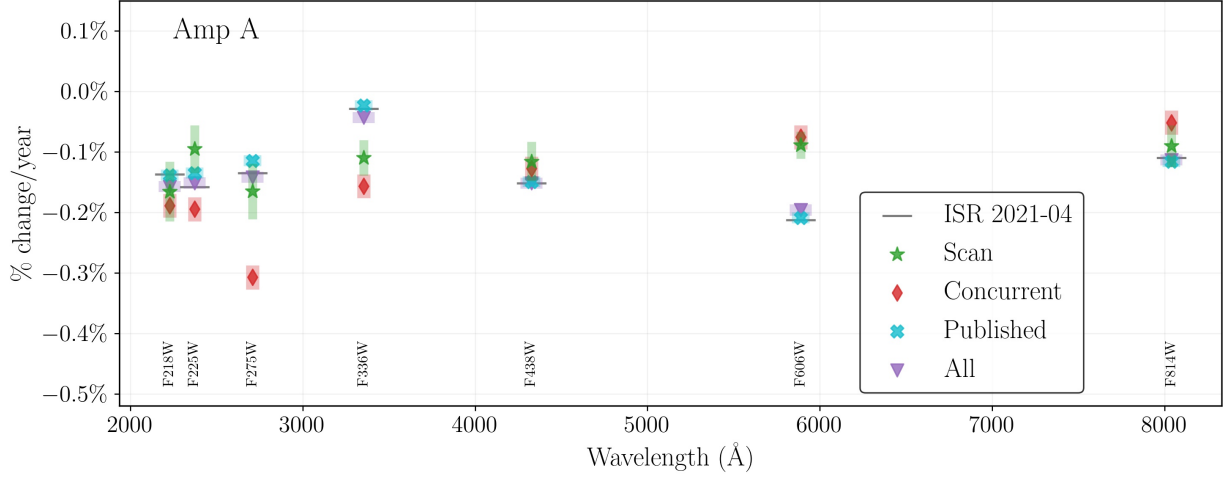


Figure 19: Modeled after Figure 7 from Calamida et al. (2021c), this plot shows the overall percent change in photometric sensitivity per year as a function of filter pivot wavelength for UVIS 1 (Amp A). Scan data is plotted as green stars. Concurrent, Published, and All staring mode data sets are plotted as red diamonds, cyan crosses, and purple triangles respectively. Standard error for each slope is plotted as a shaded rectangle. Slopes from Calamida et al. (2021c) are plotted as gray horizontal bars.

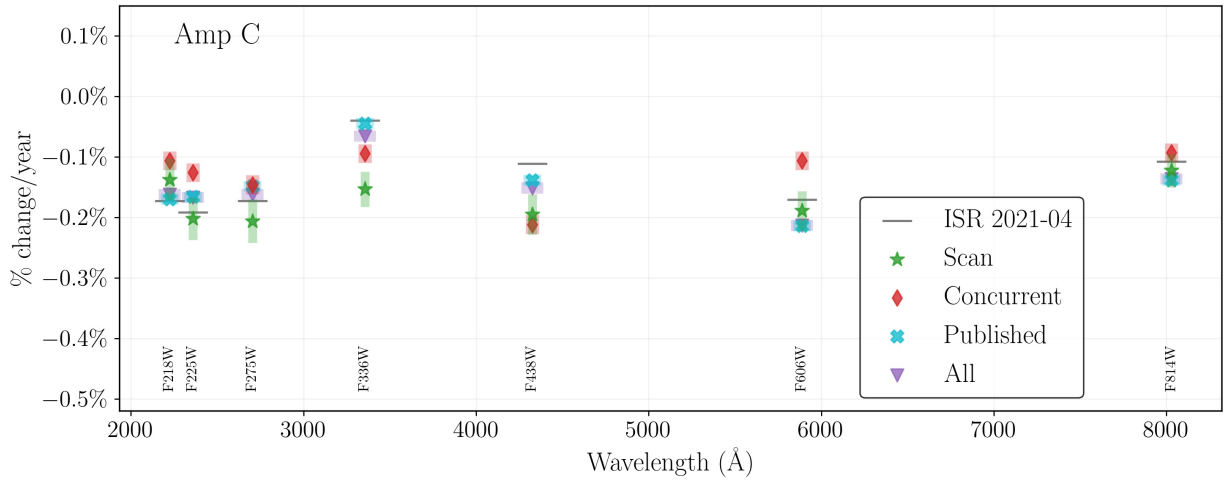


Figure 20: Same as Figure 19, but for UVIS 2 (Amp C).

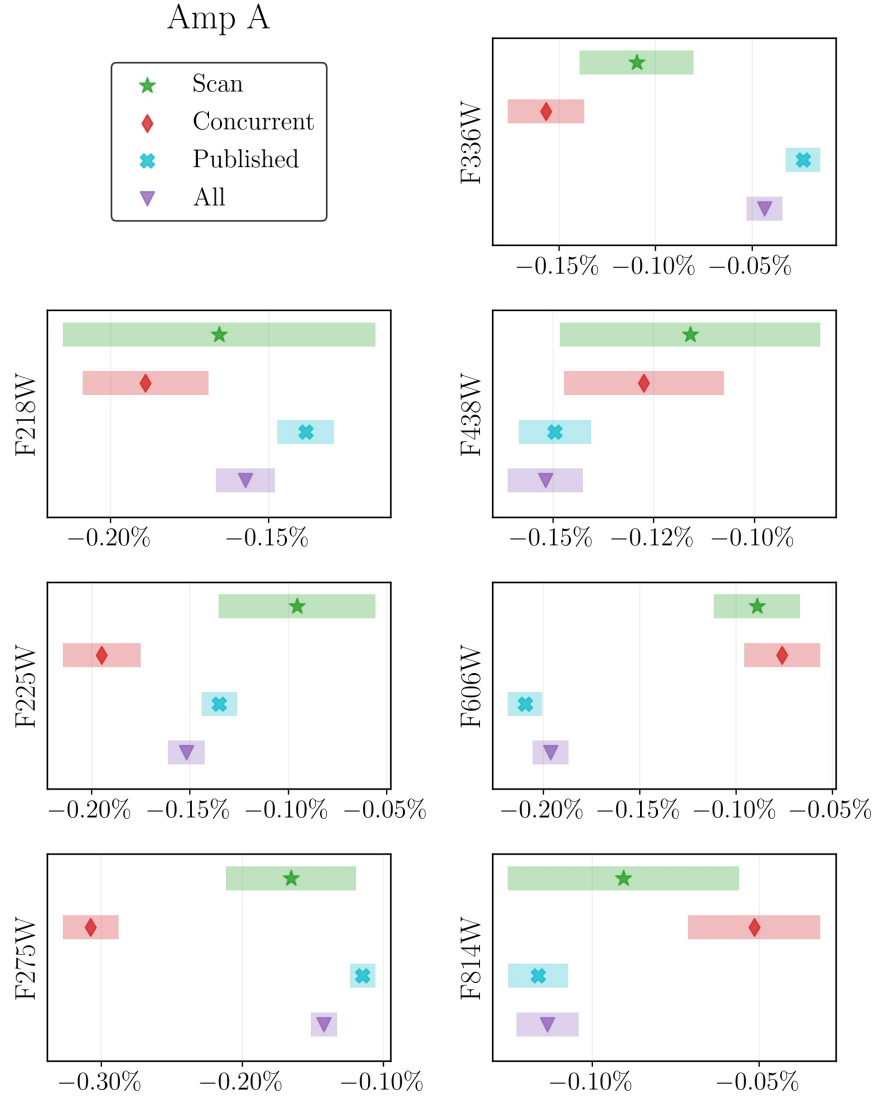


Figure 21: A closer look at the error bars in Figure 19. Slope standard errors are calculated by Equation 7.

The All dataset, plotted as purple triangles, is totally inclusive of the Published dataset, and also includes data from December 2019 through December 2021. These calculated rates allow us to see how longitudinal photometric rates are affected by the addition of most recent years' of observations. For example, if rate of detector sensitivity loss significantly increased in the past two years, the inclusion of such data would be expected to drive the calculated sensitivity rate down. However, in no filter do the All rates differ significantly from both the calculated Published rates and Calamida et al. (2021c) rates.

Next, we can compare the previous staring mode sets discussed (Published, All) and the slopes of Calamida et al. (2021c) to staring mode data from the past five years (Concurrent). Concurrent data, plotted as red diamonds, diverges significantly from long-term rates in

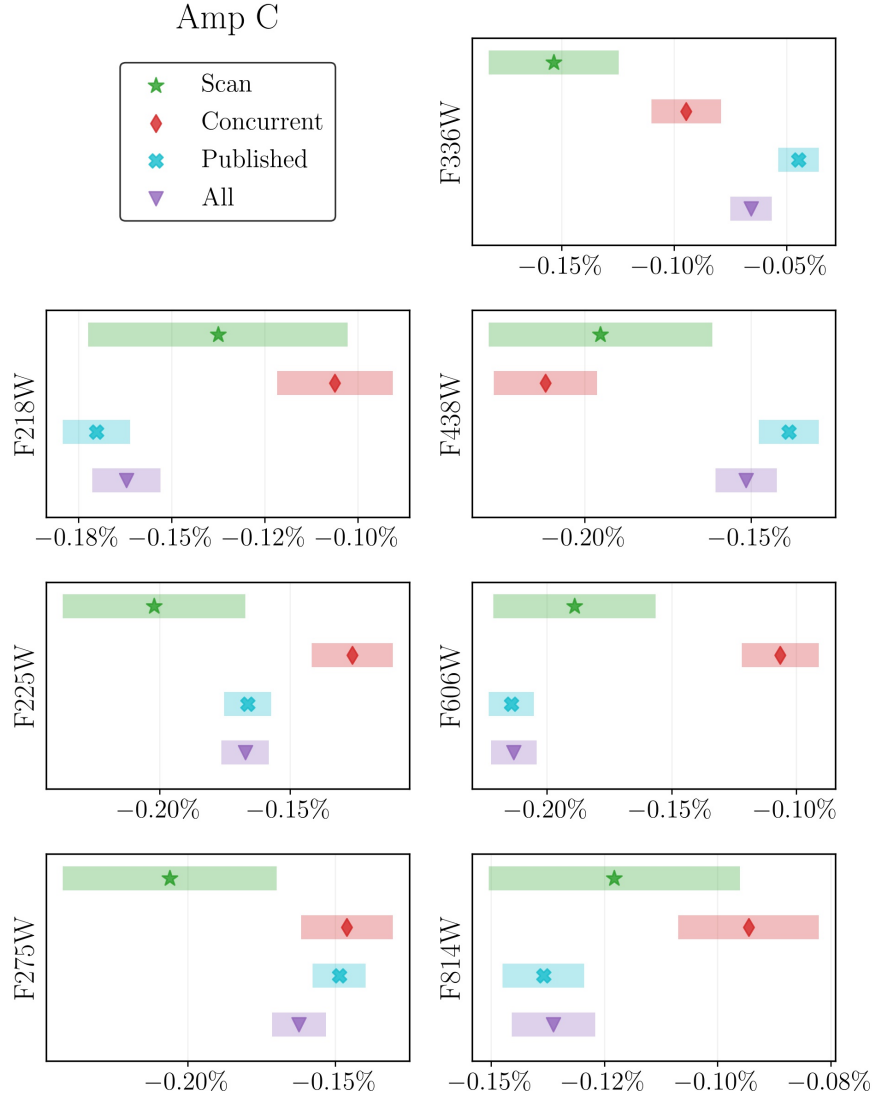


Figure 22: Same as Figure 21, but for UVIS 2 (Amp C) data.

many filters. On UVIS 1, Concurrent data records much greater losses in F275W and F336W; for F606W, Concurrent data results in a much shallower slope than in Calamida et al. (2021c) or from the Published or All datasets.

By comparing Scan rates (plotted as green stars) to rates from Calamida et al. (2021c) and the three staring mode datasets, we can see how observational methods differ, as well as examine, in aggregate, the impact of target exclusion and restricted data timespan. Scan-derived slopes are the most accurate; we’ve seen already that Scan data are relatively resistant to the systematics associated specifically with GRW70 that drove the largest differences between target-specific Concurrent rates (Figure 18).

On UVIS 1, Scan data appear to agree better with longitudinal staring mode rates (All, Published) in ultraviolet filters than Concurrent data, reflecting the impact of the differences

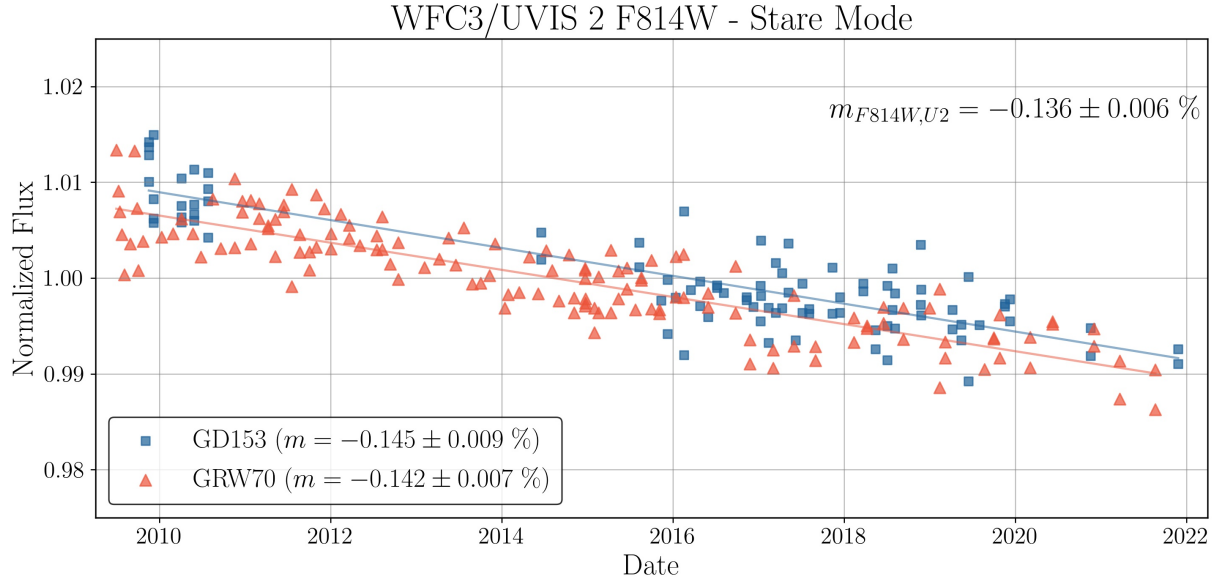


Figure 23: UVIS 2 (Amp C) F814W photometry for All data.

in the Concurrent rates derived for each target. Similarly, on UVIS 2 in F606W, Scan data align with the longer-term rates rather than the much shallower overall Concurrent rate, a byproduct of the significantly shallower rate of decline for GRW70 Concurrent data on this CCD and in this filter. Changes in detector sensitivity appear stable where scan-derived rates align with long-term staring mode rates, such that rates derived from recent high-precision data do not differ significantly from rates calculated over a much longer timespan using lower-precision observations.

However, some time-dependent differences do emerge where Scan and Concurrent rates converge at an offset from long-term rates. This is seen on UVIS 1 in F336W and F606W most significantly. In the F336W filter, Scan and Concurrent rates are moderately deeper than the Calamida et al. (2021c), All, and Published rates. In the F606W filter, Scan and Concurrent rates are instead approximately 0.1% shallower than the Calamida et al. (2021c), All, and Published rates.

It should be noted that the normalized Published and All datasets are likely affected by target coverage since installation. As seen in Figure 23 (reproduced from Figure A56 in Appendix A), there have been more observations of GRW70 than GD153. GRW70 has also been more consistently observed over a longer period of time than GD153; when pooling long-term data from the two targets together, the mean from one star is likely to be biased earlier (and thus brighter). Thus, there is systematic error in the normalization of the longitudinal datasets, contributing to larger overall residuals in the data.

5.2. Photometric Repeatability

Using mean-normalized photometry corrected for the observed slopes as a proxy for precision, we assess the repeatability of spatial scans and compare it to the Concurrent staring mode results. We find that dispersion of the spatial scan residuals is systematically smaller than that of the staring mode residuals, indicating that scans are more precise.

Figure 24 presents residuals for scan mode and staring mode photometry in F218W, divided by CCD and target; Figure 25 does the same for F606W data. Since residuals are calculated relative to mean-normalized flux, they can also be pooled together for comparison.

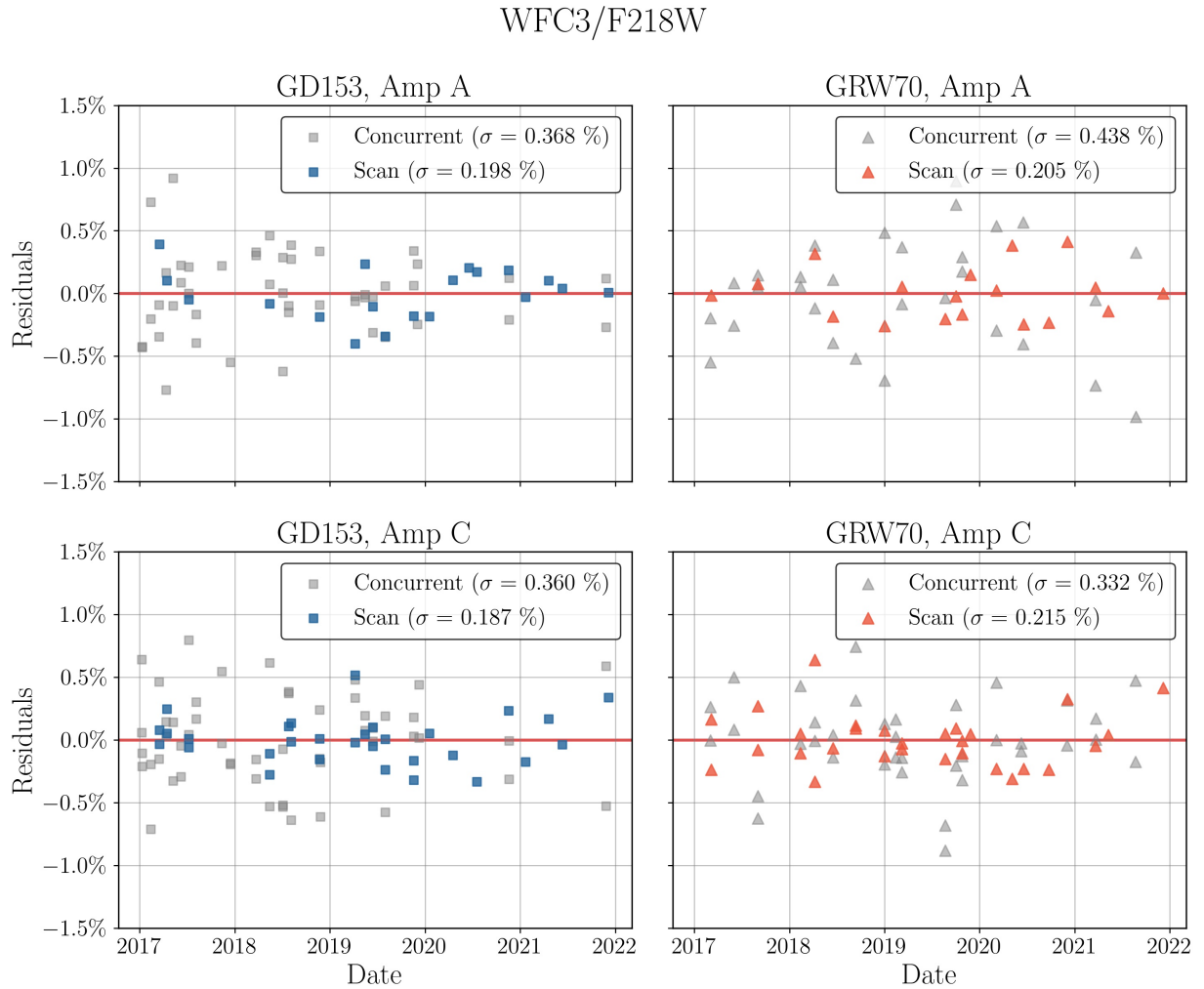


Figure 24: Residuals for Scan (colorful markers) and Concurrent staring mode observations in the F218W filter. The left column contains results for GD153 (blue and gray squares); the right column contains results for GRW70 (orange and gray triangles). The top row is UVIS 1 and the bottom row is UVIS 2. Standard deviation is included in each subplot legend.

Note that we do this only for the Scan and Concurrent datasets. As discussed in the previous section, there is a systemic error in the normalization of the longitudinal datasets due to the disparity in the frequency and number of observations of the two targets. This contributes to larger overall residuals in the data. However, the Concurrent dataset has similarly even coverage between targets over the same five-year period as the Scan dataset, so we can safely compare those datasets.

The spread of the residuals varies with filter, target, output amplifier, and observation mode. Filter-specific 1σ dispersion values for both the Scan and Concurrent datasets are presented in Table 5. Target- and filter-specific dispersion values for both the Scan and Concurrent datasets are presented in Table B1 (UVIS 1) and Table B2 (UVIS 2). In F218W, the aggregated 1σ dispersion for the Scan data is 0.201% for both UVIS 1 and UVIS 2, which also agrees well with the individual dispersion values, specified in each subplot's legend as well as tabulated in Tables B1 and B2. Meanwhile, Concurrent data for the same filter yields

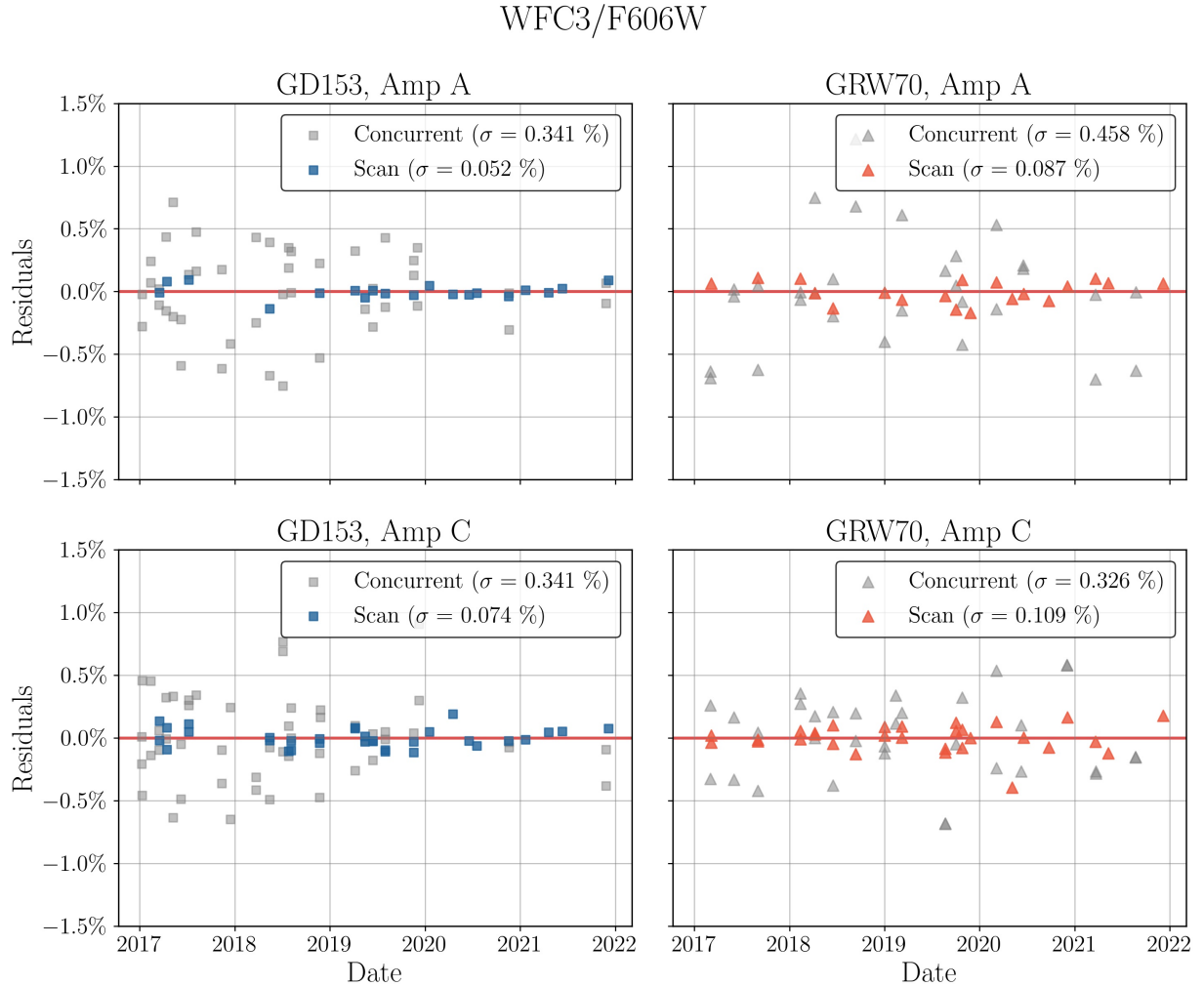


Figure 25: Same as Figure 24, but for F606W.

CCD	Filter	σ_{Scan} (%)	$\sigma_{Concurrent}$ (%)	$\sigma_{Concurrent}/\sigma_{Scan}$
UVIS 1	F218W	0.201	0.396	1.97
	F225W	0.200	0.411	2.05
	F275W	0.171	0.342	2.00
	F336W	0.119	0.323	2.71
	F438W	0.122	0.345	2.83
	F606W	0.072	0.393	5.48
	F814W	0.161	0.329	2.04
UVIS 2	F218W	0.201	0.349	1.74
	F225W	0.123	0.363	2.95
	F275W	0.131	0.376	2.87
	F336W	0.124	0.389	3.15
	F438W	0.103	0.297	2.87
	F606W	0.093	0.335	3.62
	F814W	0.153	0.280	1.82

Table 5: UVIS 1 (Amp A) and UVIS 2 (Amp C) $1 - \sigma$ dispersion of residuals for scan and staring mode data from 2017-2021 (Scan and Concurrent data sets).

$\sigma_{UVIS1} = 0.396\%$, which is significantly affected by the large scatter for Amp A observations of GRW70 ($\sigma = 0.4580\%$). On UVIS 2, Concurrent photometry across targets is more consistent, yielding $\sigma_{UVIS2} = 0.348\%$.

Taking the ratio of the dispersion of the staring mode data to the dispersion of the scan data allows us to approximate the precision with which we have made our measurements (see last column in Tables 5, B1, and B2). Thus, for UVIS 1 in the F218W filter, the ratio indicates that spatial scans are $1.97\times$ more precise than staring mode observations. For UVIS 2 in the same filter, scans are $1.74\times$ more precise than staring mode.

Figure 25 is markedly different. The dispersion of F606W Concurrent residuals is on the same order as the F218W Concurrent residuals. In contrast, Scan data is much more tightly clustered in this filter, resulting in $\sigma_{UVIS1} = 0.072\%$ and $\sigma_{UVIS2} = 0.093\%$. In fact, F606W is the only filter in which sub-0.1% repeatability is achieved, as measured by the standard deviation of the de-trended mean-normalized scan photometry. For F606W, Scan photometry was nearly 5.5 times more precise than Concurrent photometry on UVIS 1; spatial scans were 3.62 times more precise on UVIS 2.

For easier comparison of dispersion values between observation mode and across wavelength space, Figures 26 and 27 plot the information in Table 5, as well as the target-specific data in Tables B1 and B1.

While sub-0.1% repeatability, by the defined metric of this analysis, is only achieved in the F606W for the pooled-target residuals, two of the target-specific groups of residuals in F438W also yield standard deviations below this cutoff ($\sigma_{UVIS1, GD153} = 0.099\%$ and $\sigma_{UVIS2, GRW70} = 0.093\%$). Scan photometry appears to hover between 0.1% and 0.2%. While Concurrent staring mode photometry generally ranges from 0.3% and 0.4%, it is important

to note that only FLCs were used for staring mode observations in this work. The scatter of residuals for drizzled, CTE-corrected files (DRCs) would be lower.

Calculated photometric repeatability of spatial scans across all filters is $\sigma_{UVIS1} = 0.155\%$ and $\sigma_{UVIS2} = 0.136\%$. For staring mode photometry over the same time period (Concurrent dataset), the photometric repeatability is $\sigma_{UVIS1} = 0.367\%$ and $\sigma_{UVIS2} = 0.343\%$. **On average, scan mode photometry is $2.4\times$ more precise than staring mode photometry on UVIS 1; on UVIS 2, scans are $2.5\times$ more precise.**

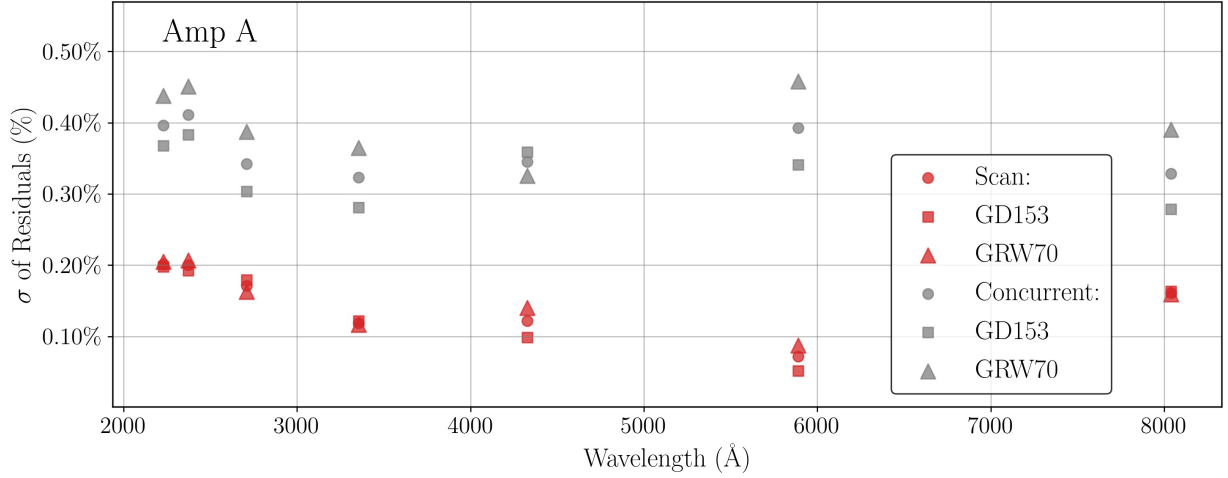


Figure 26: Dispersion of residuals against pivot wavelength of filter for UVIS 1 staring mode (gray) and scan mode (red) observations of GD153 (squares) and GRW70 (triangles) from 2017-2021. Circles plot the dispersion for the aggregated residuals.

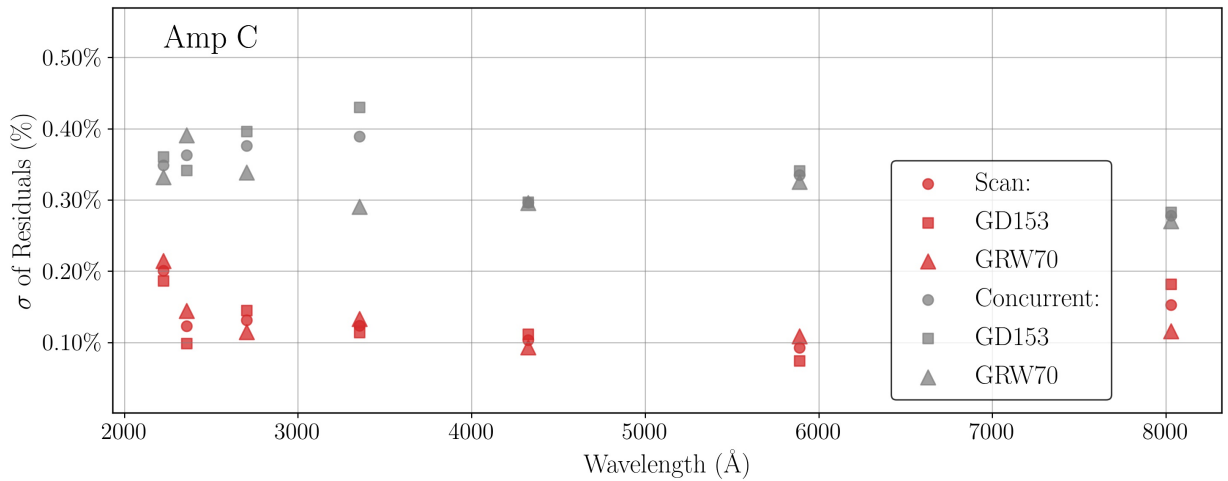


Figure 27: Same as Figure 26, but for UVIS 2.

6. Discussion

When WFC3/UVIS calibration spatial scans were evaluated in Shanahan et al. (2017a), the analysis included only observations from the first four of six orbits. This new analysis includes five years of data across five completed observing programs; this increase in our sample size and time frame allows us a more robust understanding of both the precision and accuracy of WFC3/UVIS spatial scans. In addition, we are able to better quantify the changing photometric sensitivity of the WFC3/UVIS detector.

The average photometric repeatability for spatial scans was slightly above 0.1%, with sub-0.1% repeatability only reliably occurring in F606W. In comparison to staring mode photometry over the same time period, scans offer from $2.4\times$ (UVIS 1) to $2.5\times$ (UVIS 2) better precision.

With this in mind, we observe that from 2017-2021, UVIS 1 sensitivity losses measured with high-precision scans are generally less than or equal to those measured using staring mode observations. For the Concurrent staring mode data, there were greater losses for GRW70 than GD153 in filters with pivot wavelength $< 5000\text{\AA}$. In ultraviolet filters, the target-specific loss rates had a separation of $\sim 2.5\%/year$ (see Figure 16). This drove the overall Concurrent rate down relative to the Scan data. In contrast, UVIS 2 losses are generally greater when using scans than staring mode (Figure 17). The Scan sample size for UVIS 1 is approximately 60% that of UVIS 2, leading to more uncertainty in deriving a slope for UVIS 1. Such trends underscore the importance of including spatial scans when calculating photometric zeropoints and inverse sensitivities.

The sensitivity change rates calculated by using spatial scan observations of GD153 and GRW70 agree very well, within uncertainties, with those determined by using staring mode observations of more targets in a longer time interval. The similarity of the results between stars validates that the stars are photometrically stable at the level of precision and time scales of interest.

However, we did find a small difference in the sensitivity change rates of the F336W filter for both detectors, where the sensitivity decline is steeper when calculated from recent scan photometry compared to staring mode photometry over the lifetime of the detector. In addition, the sensitivity loss of the F606W filter for UVIS 1 is lower when determined both from scanning mode and concurrently-occurring staring mode observations, compared to long-term staring mode observations. In these cases, a single linear rate over the lifespan of each detector appears inadequate for fully characterizing temporal photometric sensitivity changes.

One possible explanation is that we may be capturing underlying stellar variation, or systematics relating to the different cadences over which the targets for staring mode observations are observed. Another possibility is that the detector may be aging differently in recent epochs compared to its long-term performance.

However, uncertainty in these observations is likely underestimated. The differences between rates calculated in this work and those published in Calamida et al. (2021c) could be attributable to a target selection effect: calculating sensitivity rates using two standard

stars for this work, versus a total of five for Calamida et al. (2021c). More scan mode observations of additional standard stars will help us to better understand this issue in the future.

6.1. Future Improvements to Scan Photometry

We acknowledge that there are significant uncertainties to this analysis; evaluation of systematic errors for scan photometry is complex, and likely underestimated in this work. An in-depth characterization of systematic uncertainties for spatial scans is beyond the scope of this report, however it will be explored in future work. The scan photometry routine could be refined by fitting the scan PSF by row to improve the error in the background sky measurement. With the current volume of scan data at hand, we could also calculate experimental enclosed energies to better characterize spatial scan line-spread functions as a function of wavelength.

In the final two subsections of this document, we outline two ongoing projects related to WFC3/UVIS spatial scans.

6.2. Software Tools

Currently, WFC3 does not offer any software tools for users to process UVIS spatial scan data, and the code used for this analysis is not publicly available. This presents a two-fold issue. First, we want to use the spatial scans to better characterize the time-dependent sensitivity changes of the WFC3/UVIS detector. In addition, we would like the user to be able to fully reproduce our calibration. While the calibration data used in this analysis is publicly accessible, the software is not, and thus our results are non-reproducible outside of the WFC3 team. Secondly, any users who may wish to observe with WFC3/UVIS spatial scans will have to build their own tools to process and analyze data. This may present a barrier to entry, dissuading less experienced observers from leveraging spatial scans.

To increase transparency and accessibility, we will publicly release the `wfc3-phot-tools` library later this year, accompanied by a proof-of-concept Jupyter notebook tutorial for photometry of WFC3/UVIS spatial scans. The `wfc3-phot-tools` library will contain specialized routines for spatial scan photometry, including cosmic ray rejection (Section 3.3.1), sky subtraction (Section 3.3.3), and photometry with rectangular apertures (Section 3.3.4). It also includes generalized functions for accessing data as well as performing photometry on staring mode observations.

6.3. Aperture Corrections for Synthetic Scan Photometry

A key aspect missing from our analysis is comparison to synthetic photometry. Unlike staring mode photometry, which uses a radially symmetric and circular aperture, spatial scans are more difficult to characterize for an accurate measure of absolute photometry. We are developing rectangular aperture corrections for synthetic photometry by parameterizing enclosed energies of modeled line spread functions based on deep PSFs in staring mode. For staring mode photometry, the infinite aperture enclosing all of the light is defined at a radius

of 150 pixels. Determining the equivalent optimal aperture dimensions for a synthetic spatial scan is ongoing.

Preliminary analysis indicates our methods yield highly precise observed-to-synthetic count-rate ratios within filters; however, the observed-to-synthetic ratios are offset from 1.0 by a filter-specific offset. That is, the observed-to-synthetic ratios are precise, but not accurate. It is in the F814W filter on the UVIS 2 subarray that the spatial scan observed-to-synthetic ratios most closely approach 1.0, as seen in Figure 28.

We believe this issue originates from an incomplete characterization of synthetic spatial scans' enclosed energies. At present, a synthetic scan is created by convolving a filter-dependent PSF with a line matching the observational scan length, a process that likely overly simplifies where the light falls on the detector.

As this work is ongoing, a more thorough exploration of aperture corrections for spatial scans will be included in a future ISR.

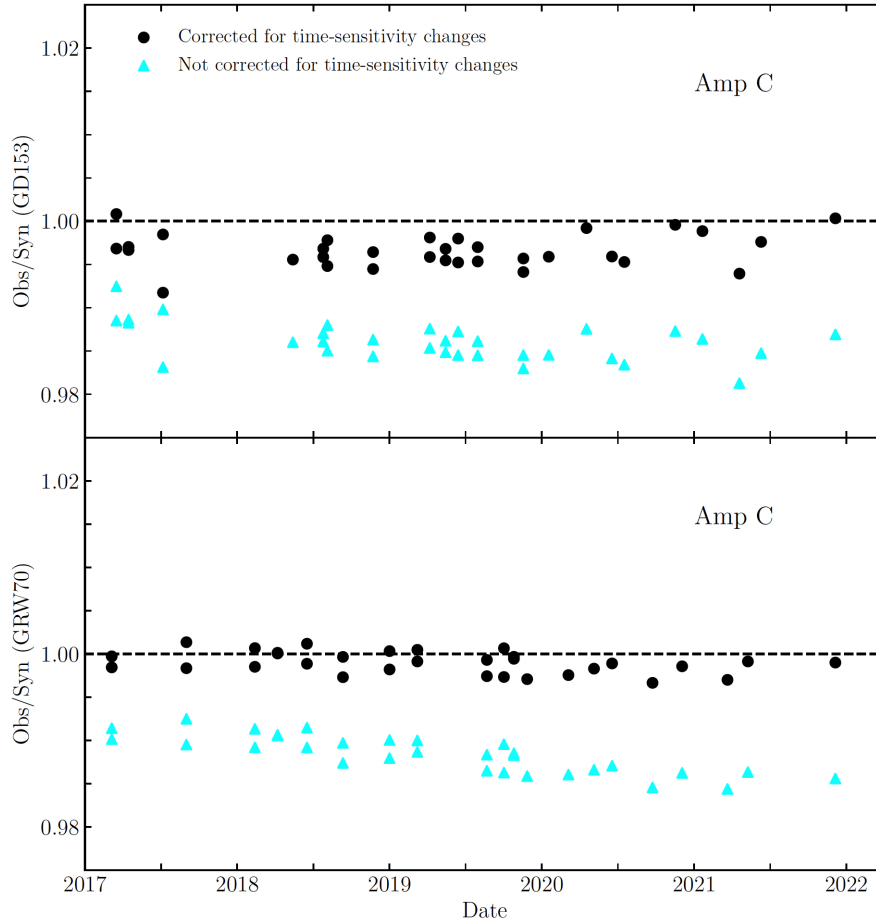


Figure 28: Preliminary observed to synthetic count-rate ratios for UVIS 2/F814W spatial scans. Duplicated from Calamida et al. (2022).

7. Conclusions

In this report, we have analyzed five years of WFC3/UVIS spatial scans to evaluate changing instrumental sensitivity and observing mode precision. We summarize our major findings as follows:

- The average photometric repeatability of spatial scans was about 0.1%.
- Spatial scans are $2.4\times$ (UVIS 1) to $2.5\times$ (UVIS 2) more precise than staring mode observations.
- Using spatial scans alone, we find overall sensitivity rates of $m_{\text{UVIS1}} = -0.119 \pm 0.008\%/ \text{year}$ and $m_{\text{UVIS2}} = -0.172 \pm 0.005\%/ \text{year}$.
- Over the same time period (2017-2021), UVIS 1 photometric sensitivity losses calculated using scans were **less than or equal to** those calculated using staring mode observations, while UVIS 2 losses obtained from scans were **slightly steeper** than those obtained from staring mode.
- Generally, detector sensitivity rates derived from recent, high-precision observations (scans) do not differ significantly from rates calculated over a much longer timespan using lower-precision observations.
- A significant exception was in the F606W filter for UVIS 1, where staring mode sensitivity losses were 0.1% steeper when evaluated over a long baseline than when restricted to scan and staring mode data observed from 2017-2021.

The authors thank Peter McCullough for his extensive review of this report and helpful discussions regarding scan photometry. We are grateful for Sylvia Baggett’s insightful suggestions along the course of this analysis and her careful eye during review. We also thank Joel Green for his thorough review of this report.

References

- Anderson, J. 2020, Strategies for Mitigation of CTE Losses in WFC3/UVIS, Space Telescope WFC3 Instrument Science Report 2020-08
- Anderson, J., et al. 2012, The Efficacy of Post-Flashing for Mitigating CTE-Losses in WFC3/UVIS Images, Space Telescope WFC3 White Paper
- Astropy Collaboration, et al. 2013, A&A, 558, A33, doi: 10.1051/0004-6361/201322068
- Astropy Collaboration, et al. 2018, AJ, 156, 123, doi: 10.3847/1538-3881/aabc4f
- Baggett, S. M., et al. 2016, WFC3/UVIS contamination and stability monitor, HST Proposal. Cycle 24, ID. #14815
- Bohlin, R. C., et al. 2014, PASP, 126, 711, doi: 10.1086/677655
- Bohlin, R. C., et al. 2020, AJ, 160, 21, doi: 10.3847/1538-3881/ab94b4
- Bradley, L., et al. 2021, astropy/photutils: 1.3.0, 1.3.0, Zenodo, doi: 10.5281/zenodo.5796924
- Calamida, A. 2020a, WFC3 UVIS Time Dependent Sensitivity, HST Proposal. Cycle 28, ID. #16416
- Calamida, A. 2020b, WFC3 UVIS and IR Photometry, HST Proposal. Cycle 28, ID. #16415
- Calamida, A., et al. 2021a, WFC3 UVIS Time Dependent Sensitivity, HST Proposal. Cycle 29, ID. #16580
- Calamida, A., et al. 2019, WFC3 UVIS and IR Photometry Monitor, HST Proposal. Cycle 27, ID. #16030
- Calamida, A., et al. 2021b, WFC3 UVIS and IR Photometry, HST Proposal. Cycle 29, ID. #16579
- Calamida, A., et al. 2021c, New time-dependent WFC3 UVIS inverse sensitivities, Space Telescope WFC3 Instrument Science Report 2021-04
- Calamida, A., et al. 2022, AJ, 164, doi: 10.3847/1538-3881/ac73f0
- Carlberg, J. K., & Monroe, T. 2017, Updated Time Dependent Sensitivity Corrections for STIS Spectral Modes, Space Telescope STIS Instrument Science Report 2017-06
- Casertano, S., et al. 2016, ApJ, 825, 11, doi: 10.3847/0004-637X/825/1/11
- Deustua, S. E., et al. 2017a, WFC3 Chip Dependent Photometry with the UV filters, Space Telescope WFC3 Instrument Science Report 2017-07
- Deustua, S. E., et al. 2017b, WFC3/UVIS Updated 2017 Chip-Dependent Inverse Sensitivity Values, Space Telescope WFC3 Instrument Science Report 2017-14
- Fraine, J., et al. 2021, AJ, 161, 269, doi: 10.3847/1538-3881/abe8d6
- Gilliland, R. L., et al. 2010, WFC3 UVIS Full Well Depths, and Linearity Near and Beyond Saturation, Space Telescope WFC3 Instrument Science Report 2010-10
- Ginsburg, A., et al. 2019, AJ, 157, 98, doi: 10.3847/1538-3881/aafc33
- Gosmeyer, C. M., & Baggett, S. M. 2016, WFC3/UVIS External CTE Monitor: Single-Chip CTE Measurements, Space Telescope WFC3 Instrument Science Report 2016-17
- Kalirai, J. S., et al. 2010, WFC3 Pixel Area Maps, Space Telescope WFC3 Instrument Science Report 2010-08
- Khandrika, H., et al. 2018, WFC3/UVIS - Temporal and Spatial Variations in Photometry, Space Telescope WFC3 Instrument Science Report 2018-16
- McCullough, P. 2017, Trajectories of Multi-lined Spatial Scans, Space Telescope WFC3 Instrument Science Report 2017-06

- McCullough, P., et al. 2016, WFC3 UVIS contamination using spatial scans, HST Proposal. Cycle 24, ID. #14878
- McCullough, P., et al. 2018, WFC3 UVIS Contamination Monitor (staring and scans), HST Proposal. Cycle 26, ID. #15583
- McCullough, P., et al. 2017, WFC3/UVIS Contamination Monitor, HST Proposal. Cycle 25, ID #15398
- McCullough, P., & MacKenty, J. 2012, Considerations for using Spatial Scans with WFC3, Space Telescope WFC3 Instrument Science Report 2012-08
- Riess, A. G., et al. 2014, ApJ, 785, 161, doi: 10.1088/0004-637X/785/2/161
- Ryan, R. E., J., et al. 2016, The Updated Calibration Pipeline for WFC3/UVIS: a Reference Guide to calwf3 (version 3.3), Space Telescope WFC3 Instrument Science Report 2016-01
- Sabbi, E., & Bellini, A. 2013, UVIS PSF Spatial & Temporal Variations, Space Telescope WFC3 Instrument Science Report 2013-11
- Sabbi, E., & WFC3 Team. 2013, WFC3 Cycle 20 Calibration Program, Space Telescope WFC3 Instrument Science Report 2013-05
- Shanahan, C., et al. 2019, WFC3 UVIS Time Dependent Sensitivity, HST Proposal. Cycle 27, ID. #16021
- Shanahan, C., et al. 2017a, Photometric Repeatability of Scanned Imagery: UVIS, Space Telescope WFC3 Instrument Science Report 2017-21
- Shanahan, C. E., et al. 2017b, 2017 Update on the WFC3/UVIS Stability and Contamination Monitor, Space Telescope WFC3 Instrument Science Report 2017-15
- Virtanen, P., et al. 2020, Nature Methods, 17, 261, doi: 10.1038/s41592-019-0686-2

A Appendix A - Sensitivity Losses

A1. Scan Data

Filter	Target	n	$m \pm m_{err}$ (%/yr)	σ (%)
F218W	GD153	19	-0.199 ± 0.035	0.335
	GRW70	18	-0.125 ± 0.041	0.258
F225W	GD153	18	-0.132 ± 0.035	0.263
	GRW70	19	-0.056 ± 0.039	0.219
F275W	GD153	19	-0.202 ± 0.032	0.331
	GRW70	19	-0.123 ± 0.031	0.227
F336W	GD153	21	-0.106 ± 0.021	0.187
	GRW70	19	-0.115 ± 0.022	0.187
F438W	GD153	18	-0.113 ± 0.018	0.185
	GRW70	19	-0.119 ± 0.027	0.207
F606W	GD153	19	-0.092 ± 0.009	0.136
	GRW70	19	-0.086 ± 0.017	0.140
F814W	GD153	16	-0.076 ± 0.030	0.198
	GRW70	19	-0.107 ± 0.030	0.210

Table A1: UVIS 1 (Amp A) target-specific detector sensitivity decline rates for each filter. Values are derived solely from **spatial scan data from 2017-2021** (Scan dataset). The number of exposures in each subset is indicated by n . Slopes (percent sensitivity loss per year) are listed with their standard errors. Standard deviation of the normalized flux for each data subset is listed as a percentage.

Filter	Target	n	$m \pm m_{err}$ (%/yr)	σ (%)
F218W	GD153	30	-0.140 ± 0.027	0.262
	GRW70	29	-0.135 ± 0.033	0.273
F225W	GD153	32	-0.219 ± 0.015	0.281
	GRW70	30	-0.187 ± 0.022	0.270
F275W	GD153	34	-0.207 ± 0.019	0.309
	GRW70	31	-0.205 ± 0.018	0.274
F336W	GD153	32	-0.152 ± 0.016	0.227
	GRW70	31	-0.155 ± 0.020	0.231
F438W	GD153	33	-0.203 ± 0.016	0.282
	GRW70	30	-0.187 ± 0.014	0.248
F606W	GD153	32	-0.188 ± 0.011	0.254
	GRW70	30	-0.190 ± 0.017	0.258
F814W	GD153	32	-0.095 ± 0.026	0.219
	GRW70	31	-0.154 ± 0.018	0.221

Table A2: Same as Table A1, but for UVIS 2 (Amp C) rates of detector sensitivity decline

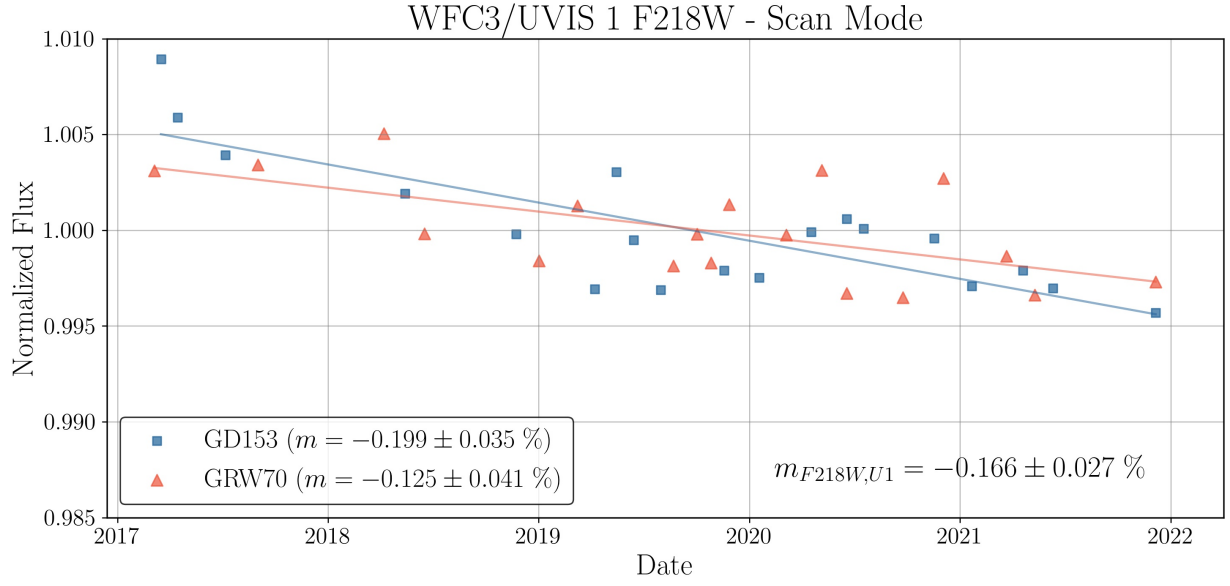


Figure A1: UVIS 1 (Amp A) F218W photometry for Scan data.

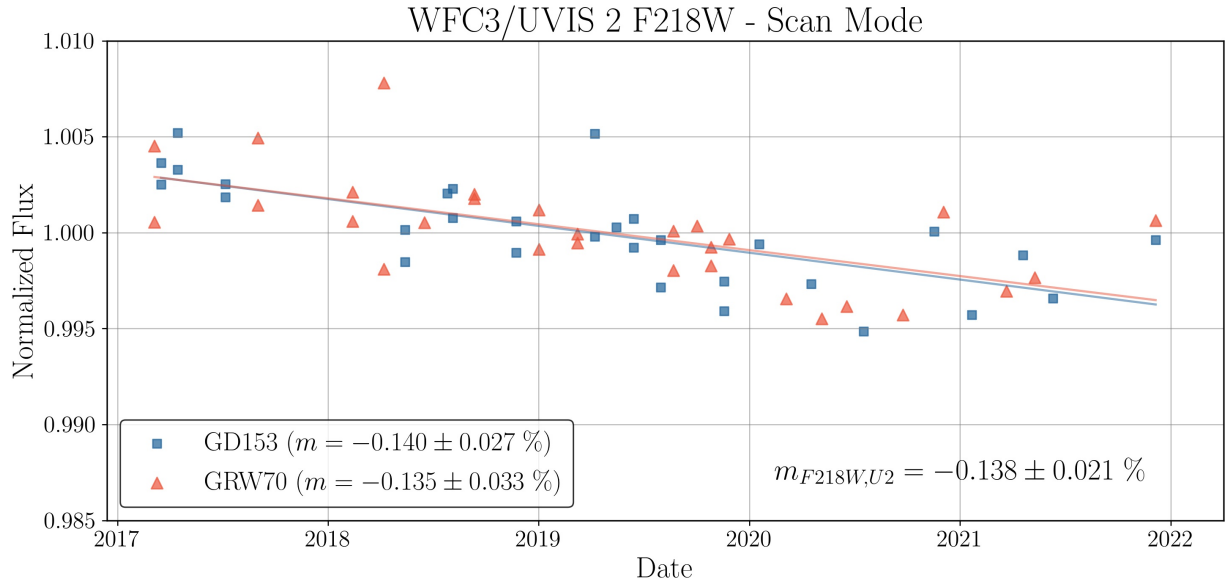


Figure A2: UVIS 2 (Amp C) F218W photometry for Scan data.

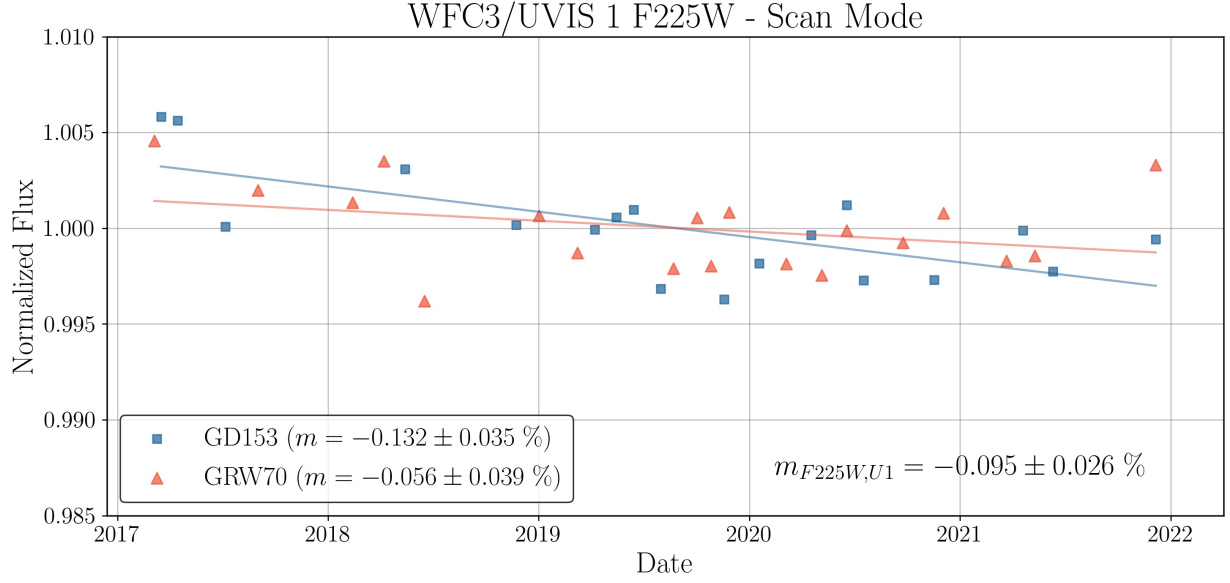


Figure A3: UVIS 1 (Amp A) F225W photometry for Scan data.

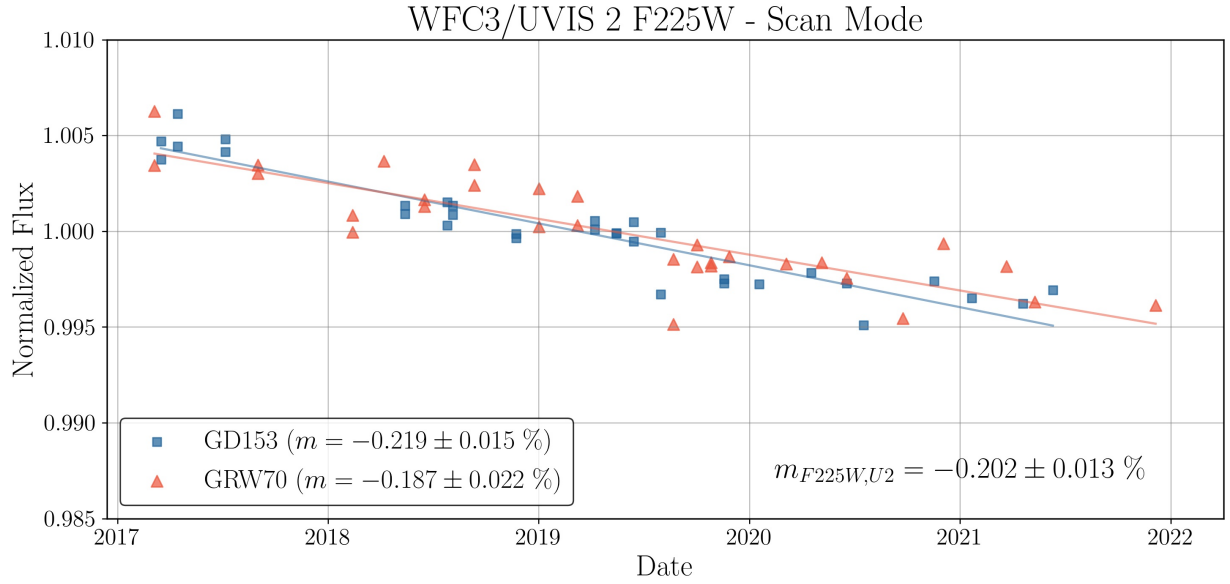


Figure A4: UVIS 2 (Amp C) F225W photometry for Scan data.

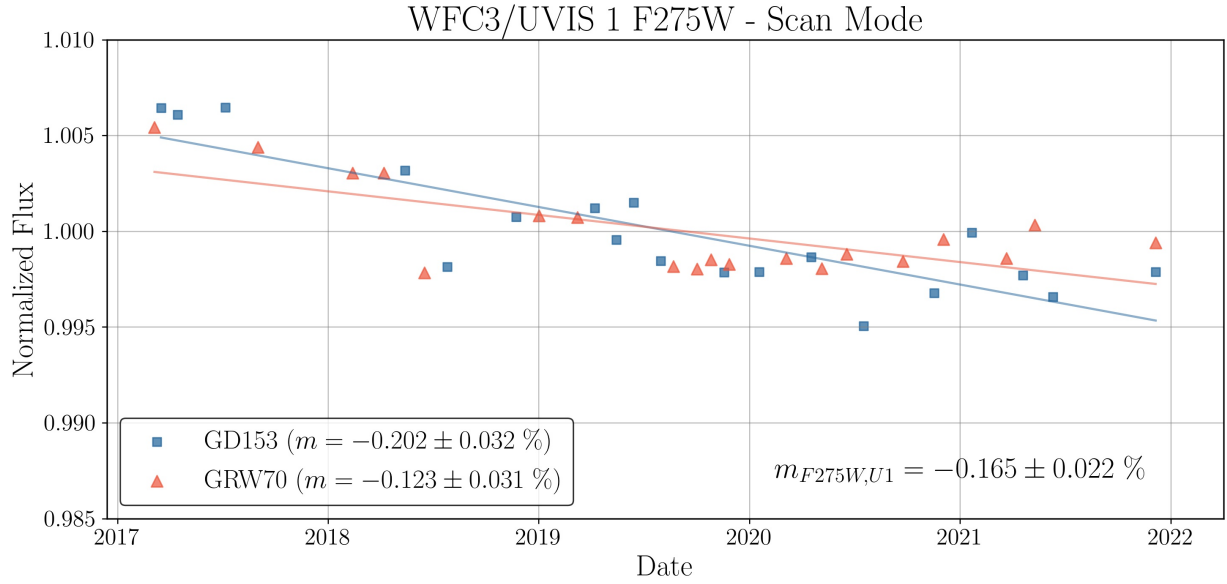


Figure A5: UVIS 1 (Amp A) F275W photometry for Scan data.

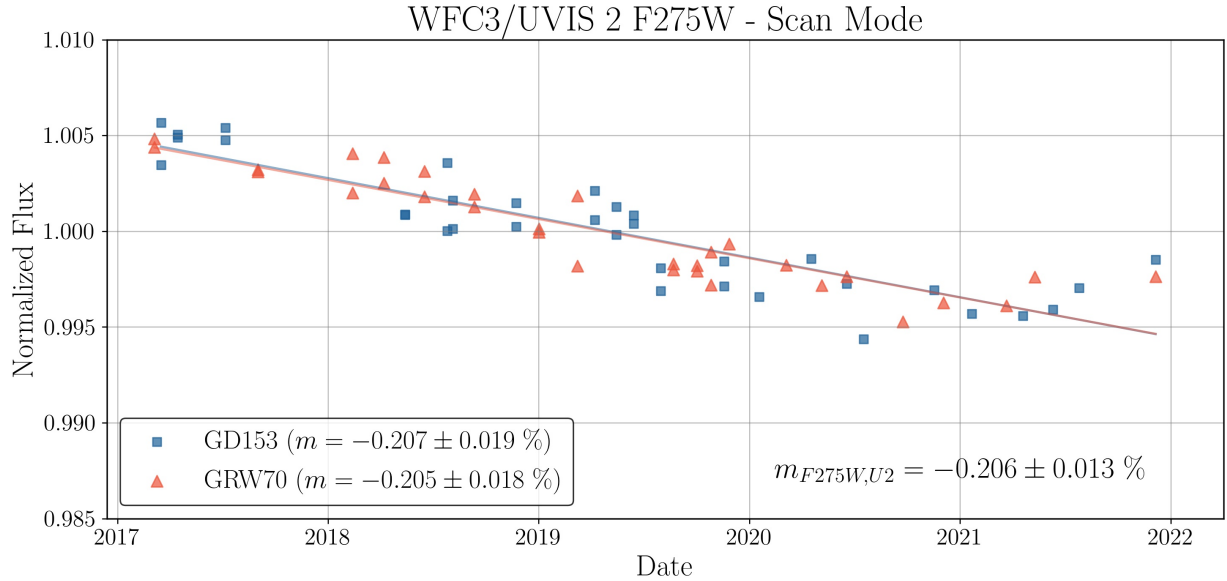


Figure A6: UVIS 2 (Amp C) F275W photometry for Scan data.

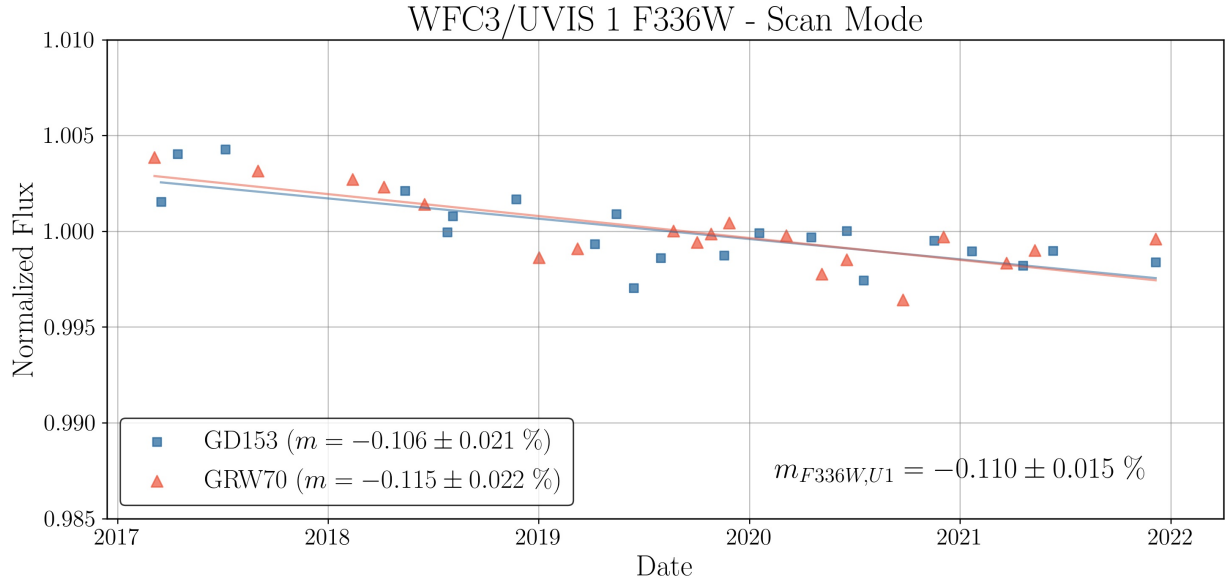


Figure A7: UVIS 1 (Amp A) F336W photometry for Scan data.

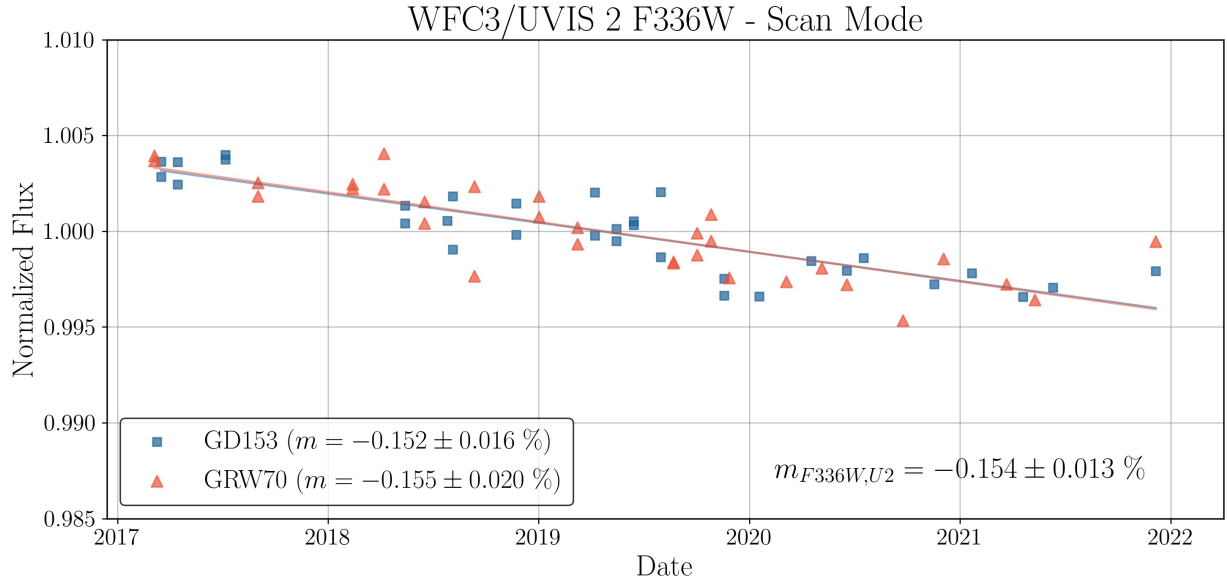


Figure A8: UVIS 2 (Amp C) F336W photometry for Scan data.

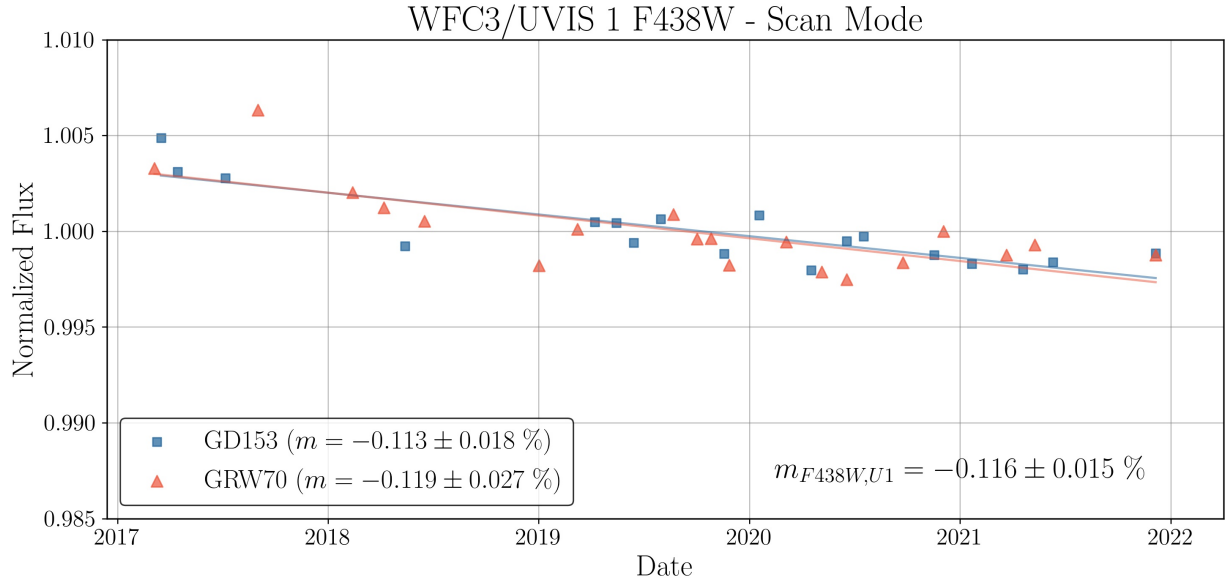


Figure A9: UVIS 1 (Amp A) F438W photometry for Scan data.

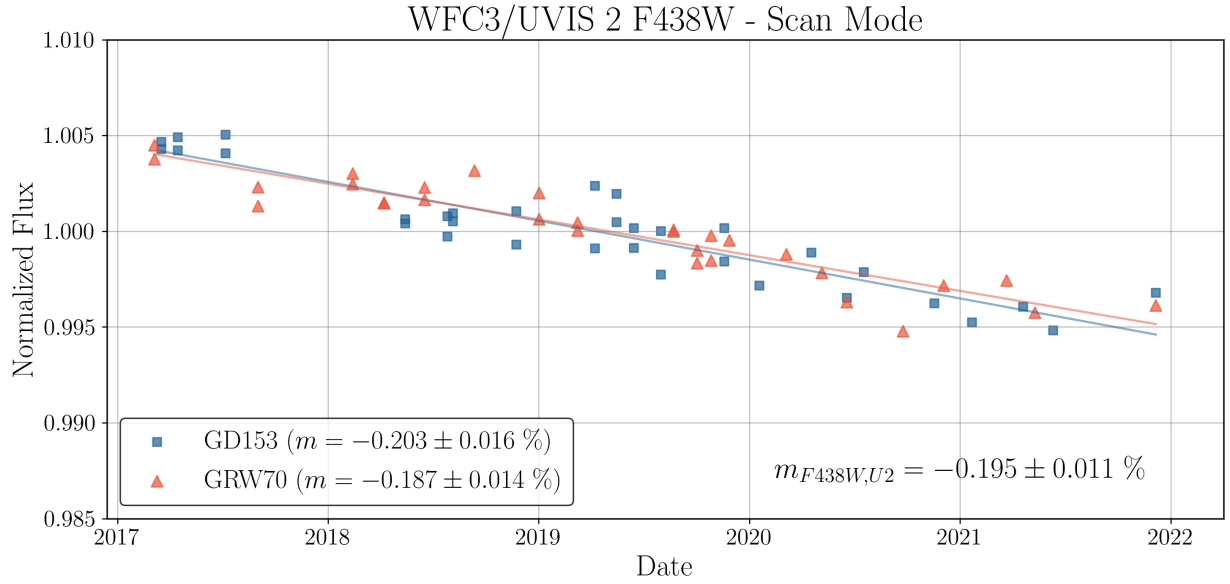


Figure A10: UVIS 2 (Amp C) F438W photometry for Scan data.

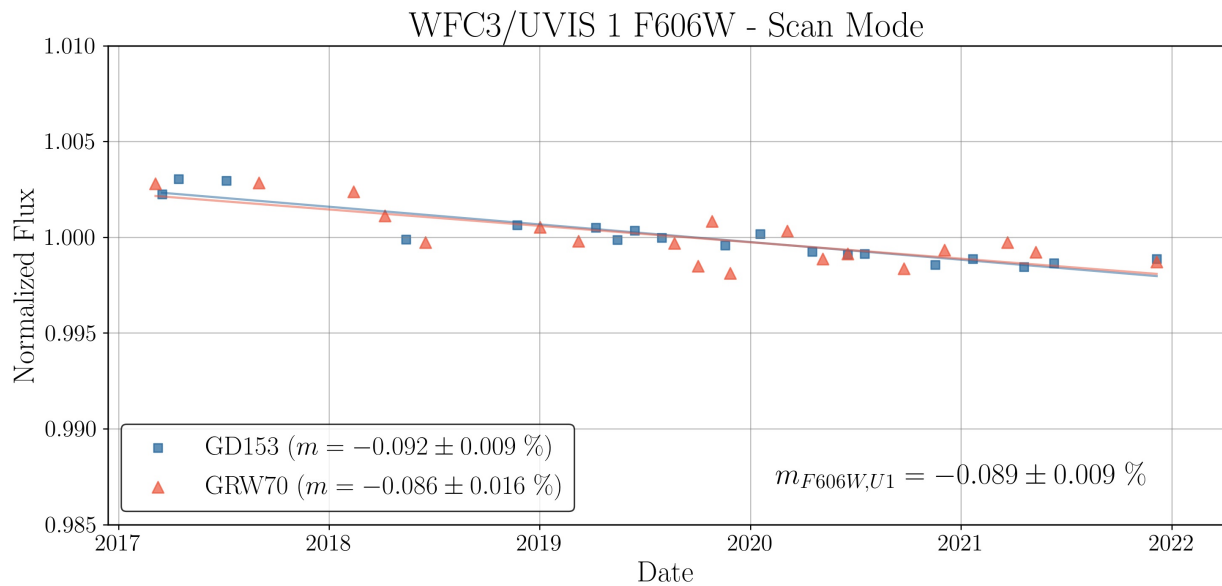


Figure A11: UVIS 1 (Amp A) F606W photometry for Scan data.

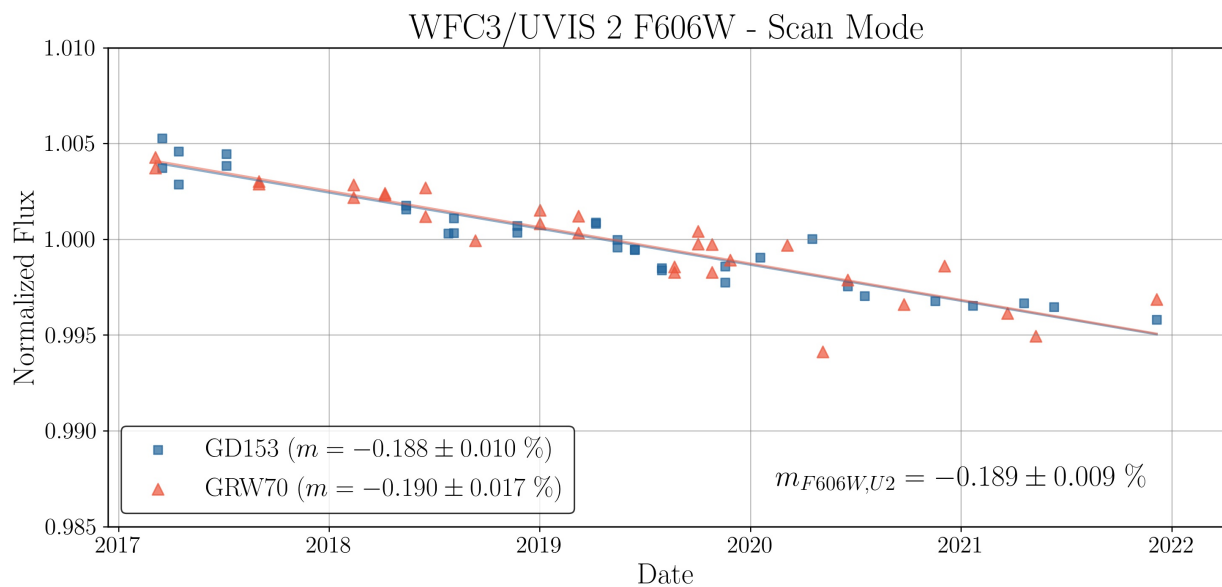


Figure A12: UVIS 2 (Amp C) F606W photometry for Scan data.

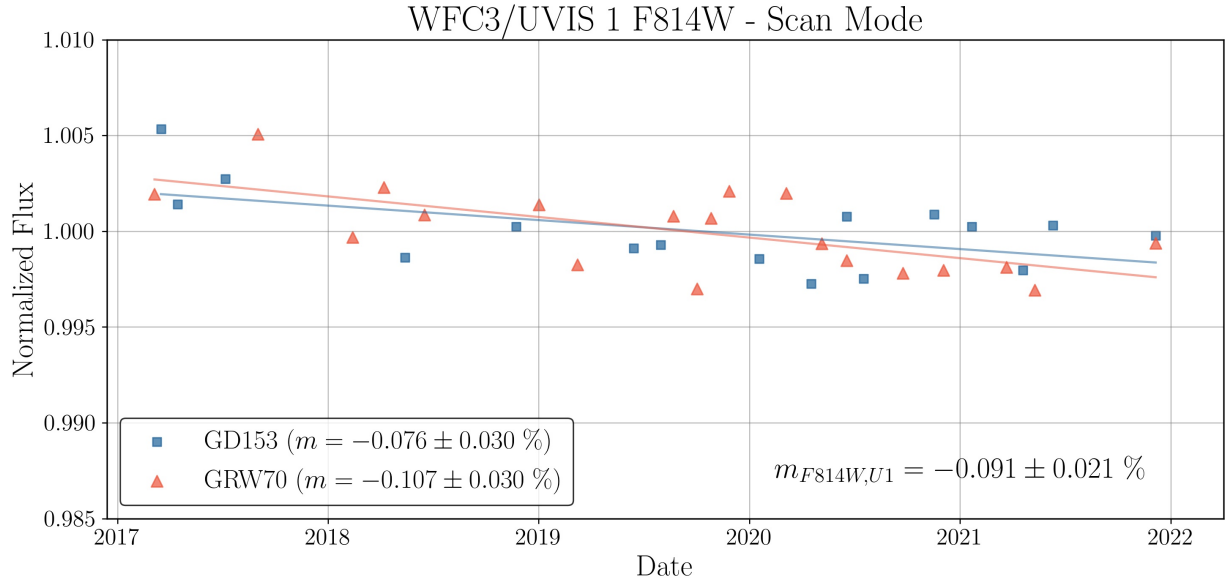


Figure A13: UVIS 1 (Amp A) F814W photometry for Scan data.

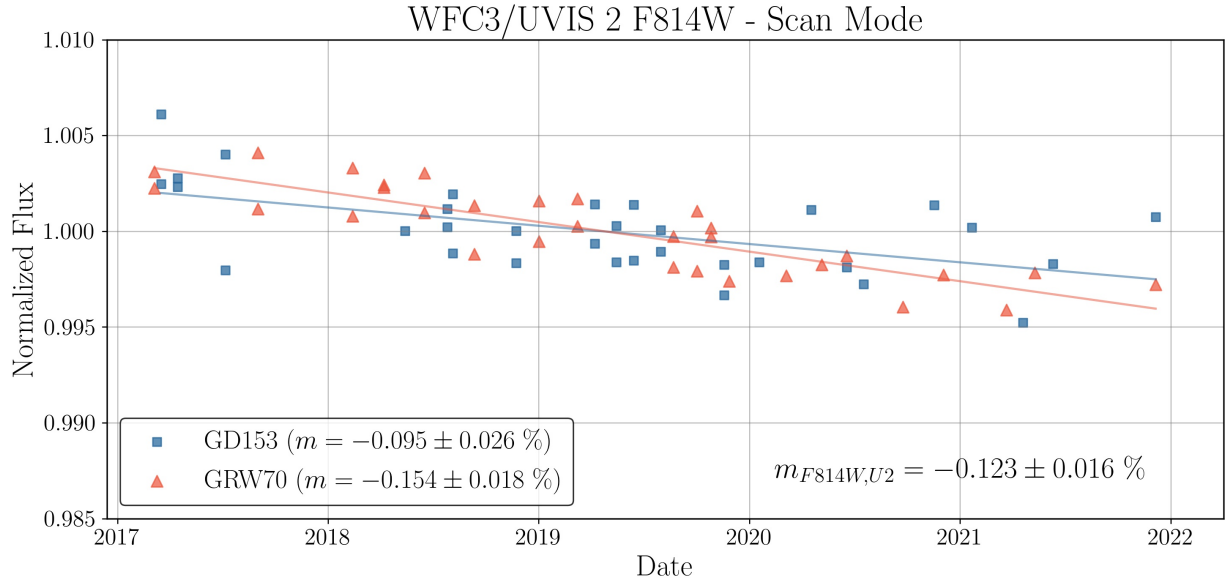


Figure A14: UVIS 2 (Amp C) F814W photometry for Scan data.

A2. Concurrent Data

As defined in Section 3.4., the Concurrent dataset is comprised of staring mode observations of GD153 and GRW70 in the set of core filters from 2017 to 2021.

Filter	Target	n	$m \pm m_{err}$ (%/yr)	σ (%)
F218W	GD153	47	-0.071 ± 0.039	0.278
	GRW70	30	-0.378 ± 0.063	0.398
F225W	GD153	49	-0.109 ± 0.045	0.340
	GRW70	32	-0.343 ± 0.064	0.472
F275W	GD153	41	-0.229 ± 0.040	0.336
	GRW70	31	-0.417 ± 0.056	0.407
F336W	GD153	25	-0.117 ± 0.039	0.311
	GRW70	22	-0.238 ± 0.062	0.471
F438W	GD153	40	-0.087 ± 0.038	0.418
	GRW70	31	-0.200 ± 0.048	0.666
F606W	GD153	44	-0.050 ± 0.040	0.403
	GRW70	30	-0.120 ± 0.064	0.625
F814W	GD153	44	-0.034 ± 0.033	0.340
	GRW70	30	-0.082 ± 0.055	0.663

Table A3: Same as Table A1, but derived solely from **staring mode data from 2017-2021** (Concurrent data set).

Filter	Target	n	$m \pm m_{err}$ (%/yr)	σ (%)
F218W	GD153	52	-0.098 ± 0.042	0.318
	GRW70	37	-0.139 ± 0.045	0.289
F225W	GD153	52	-0.136 ± 0.040	0.391
	GRW70	37	-0.138 ± 0.052	0.332
F275W	GD153	65	-0.136 ± 0.050	0.431
	GRW70	37	-0.185 ± 0.045	0.402
F336W	GD153	49	-0.103 ± 0.043	0.351
	GRW70	25	-0.117 ± 0.047	0.327
F438W	GD153	49	-0.248 ± 0.034	0.438
	GRW70	35	-0.204 ± 0.041	0.405
F606W	GD153	50	-0.163 ± 0.039	0.383
	GRW70	33	-0.052 ± 0.044	0.423
F814W	GD153	51	-0.117 ± 0.033	0.382
	GRW70	34	-0.079 ± 0.037	0.375

Table A4: Same as Table A3, but for UVIS 2 (Amp C) rates of detector sensitivity decline.

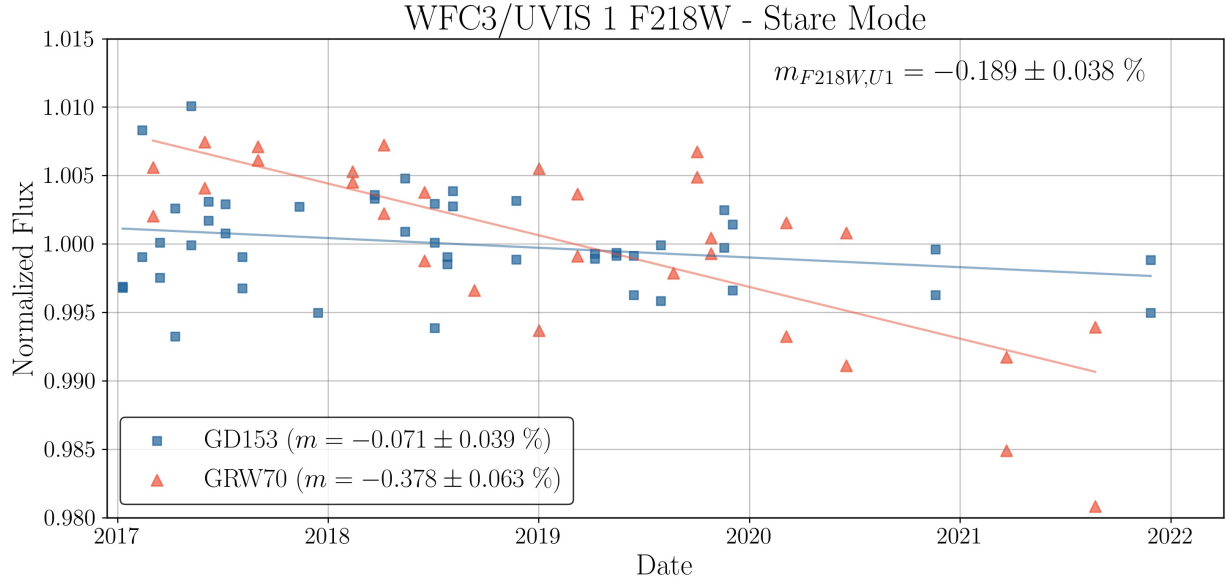


Figure A15: UVIS 1 (Amp A) F218W photometry for Concurrent data.

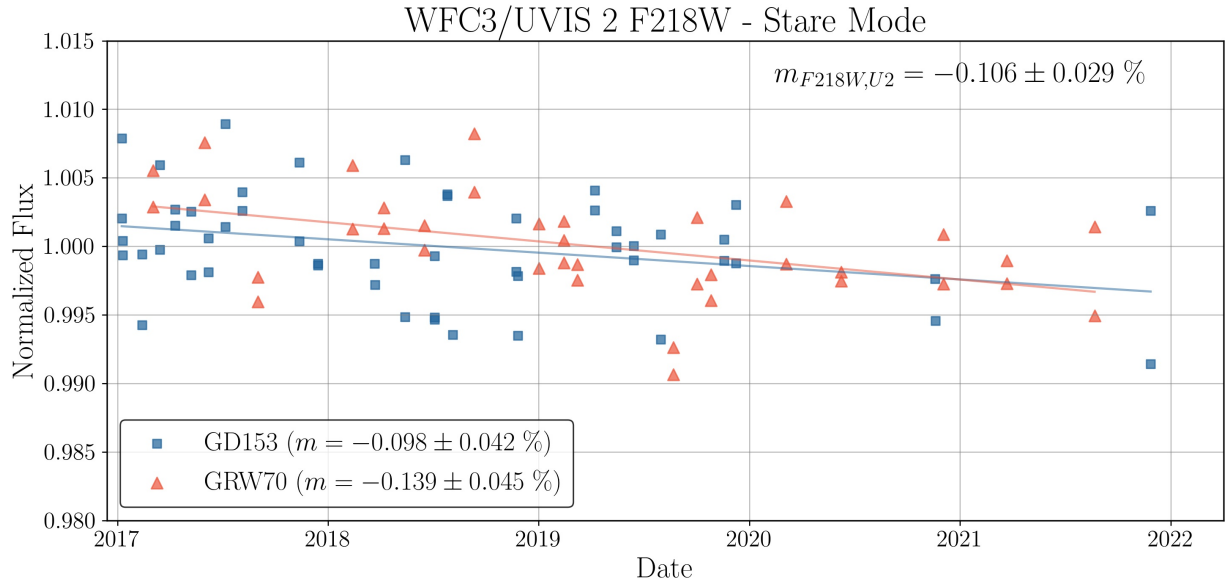


Figure A16: UVIS 2 (Amp C) F218W photometry for Concurrent data.

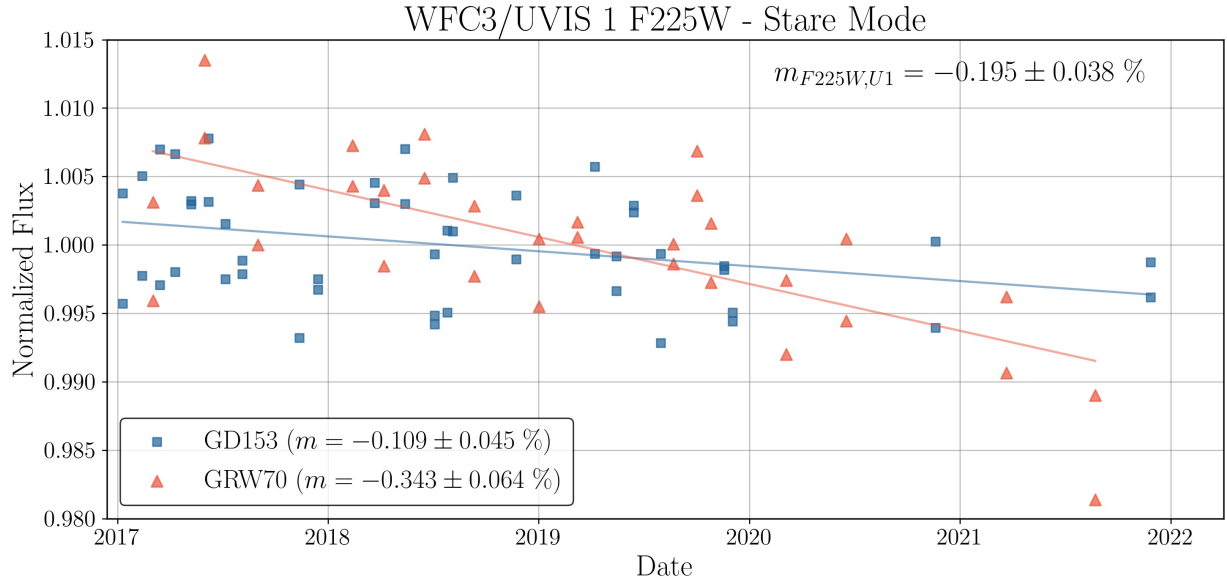


Figure A17: UVIS 1 (Amp A) F225W photometry for Concurrent data.

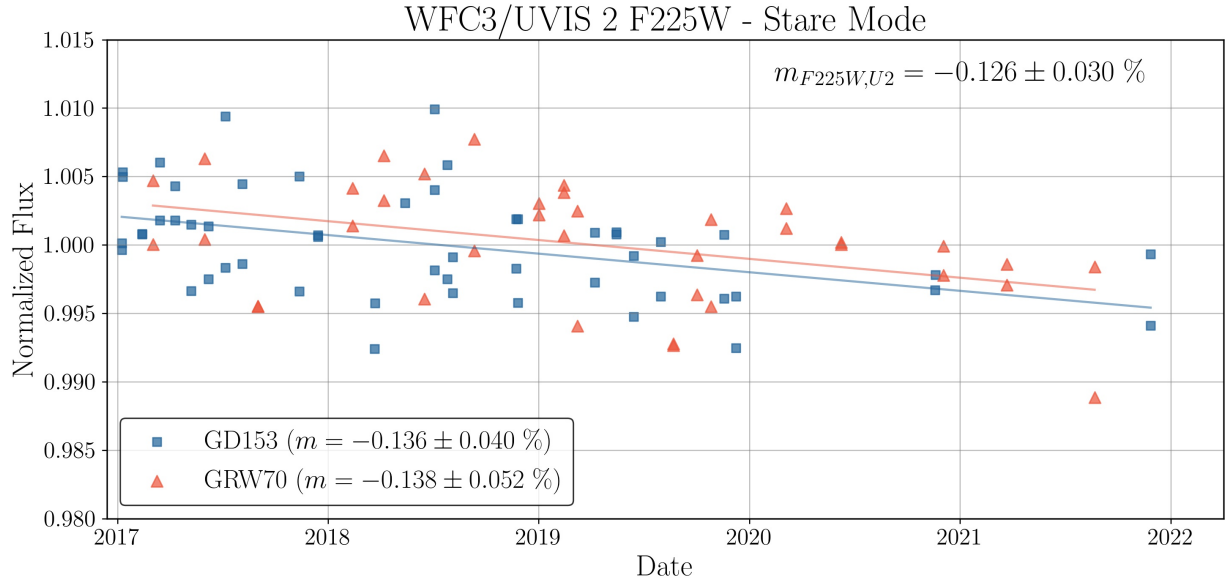


Figure A18: UVIS 2 (Amp C) F225W photometry for Concurrent data.

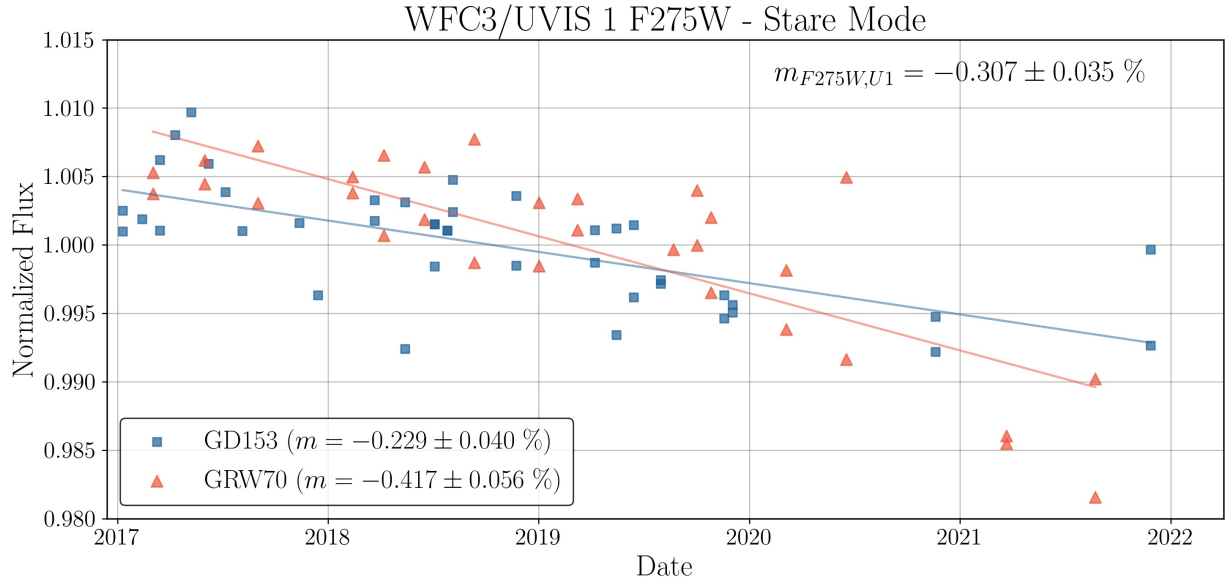


Figure A19: UVIS 1 (Amp A) F275W photometry for Concurrent data.

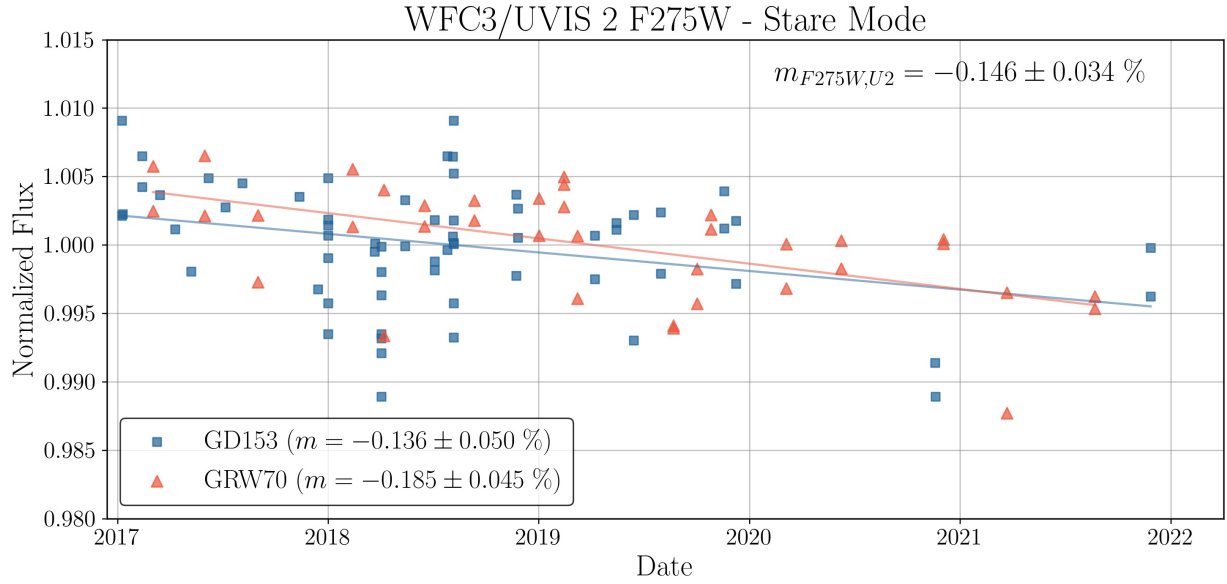


Figure A20: UVIS 2 (Amp C) F275W photometry for Concurrent data.

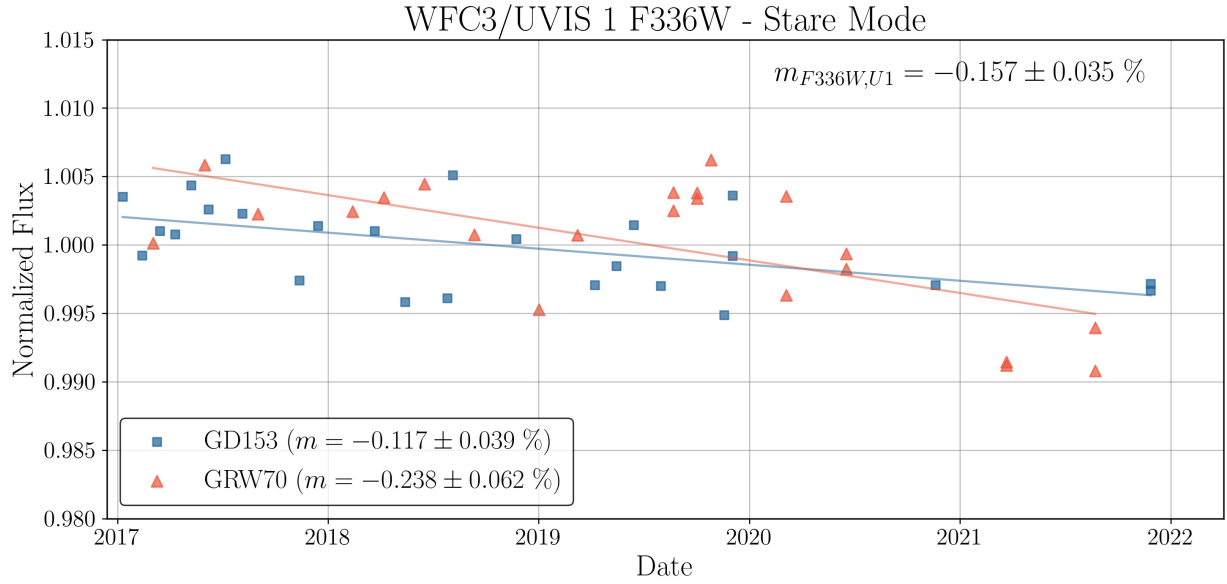


Figure A21: UVIS 1 (Amp A) F336W photometry for Concurrent data.

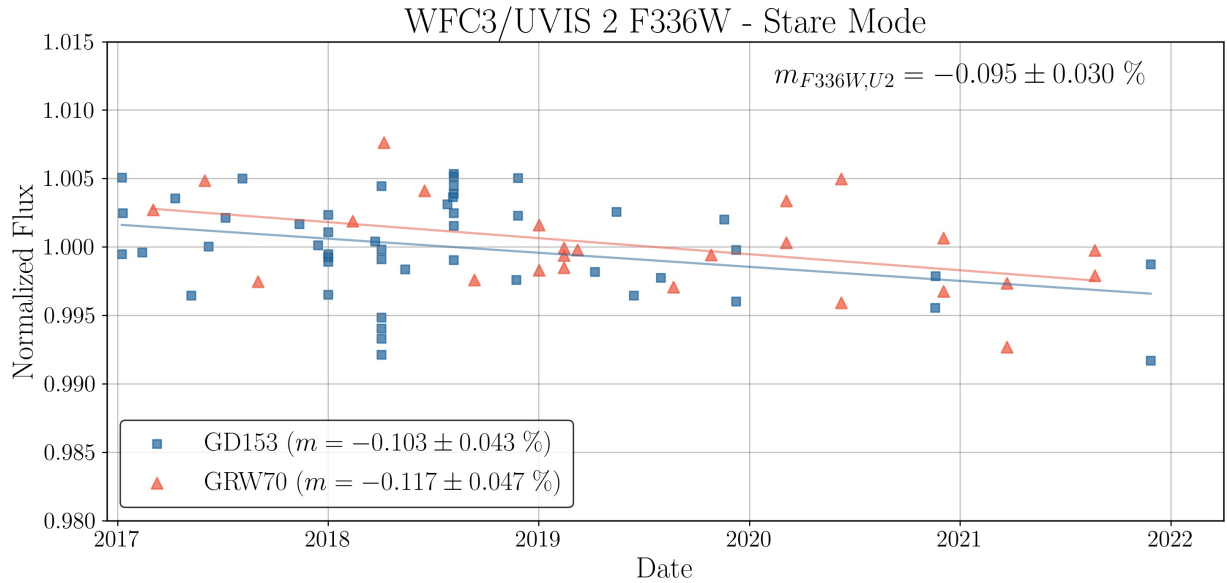


Figure A22: UVIS 2 (Amp C) F336W photometry for Concurrent data.

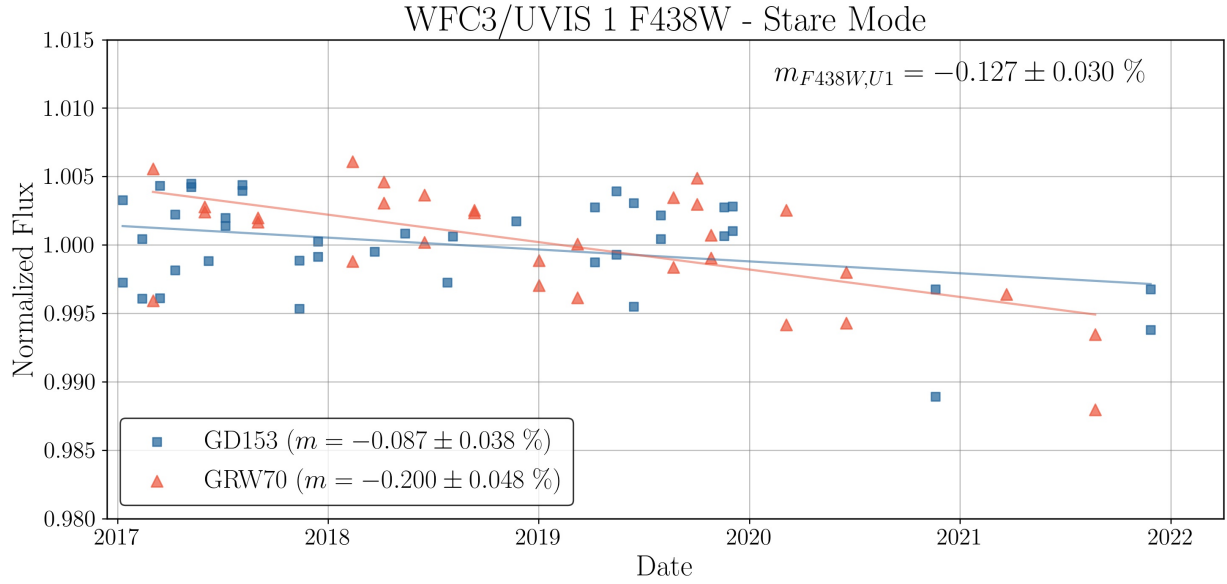


Figure A23: UVIS 1 (Amp A) F438W photometry for Concurrent data.

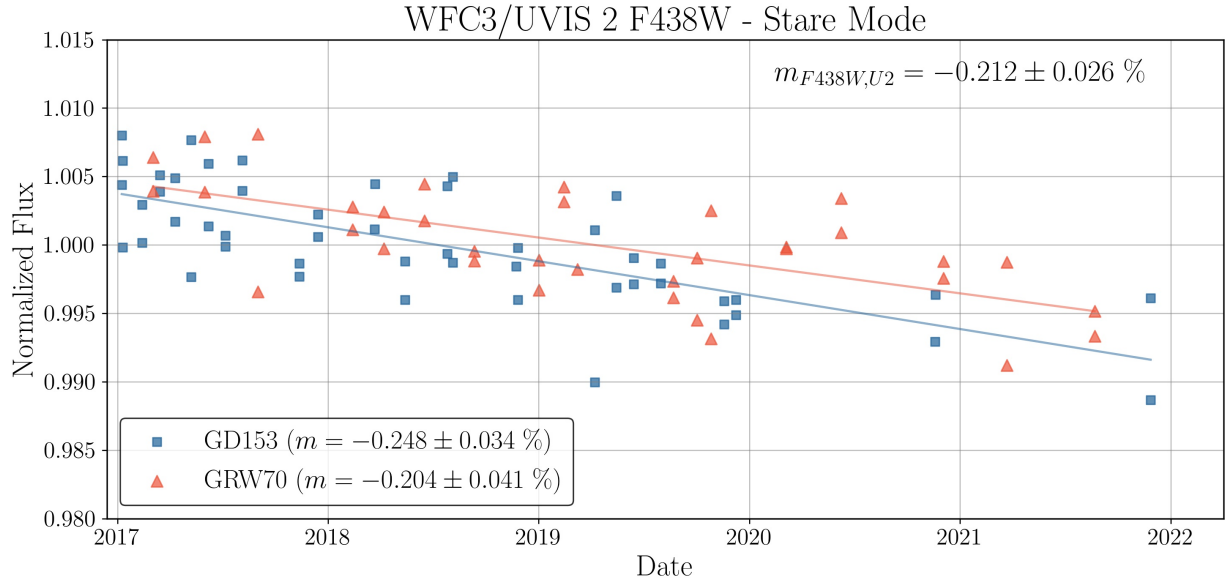


Figure A24: UVIS 2 (Amp C) F438W photometry for Concurrent data.

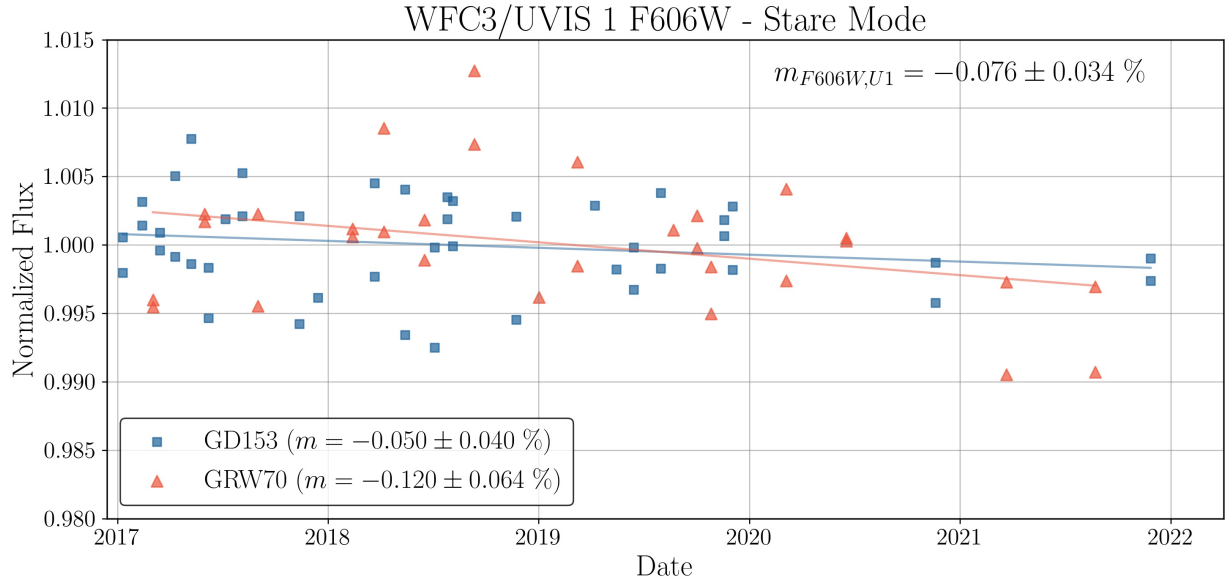


Figure A25: UVIS 1 (Amp A) F606W photometry for Concurrent data.

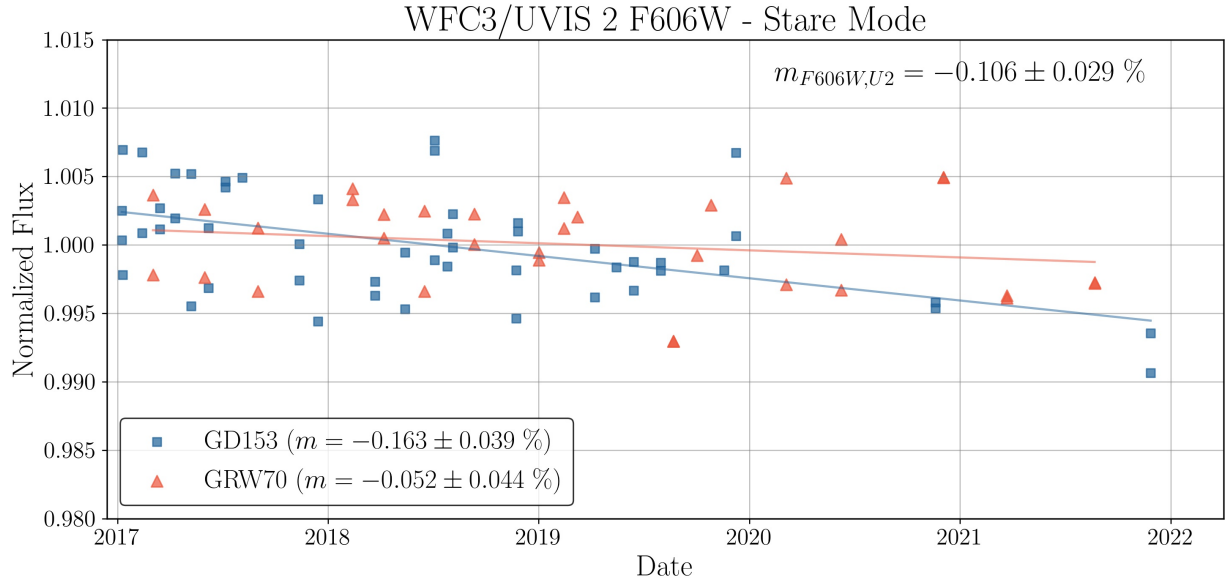


Figure A26: UVIS 2 (Amp C) F606W photometry for Concurrent data.

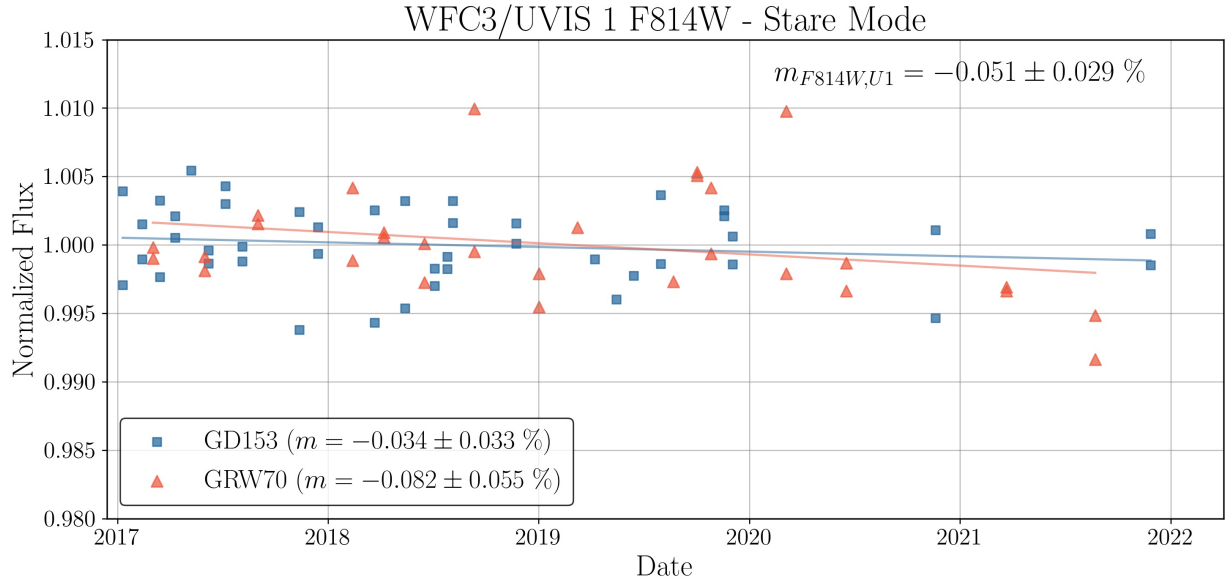


Figure A27: UVIS 1 (Amp A) F814W photometry for Concurrent data.

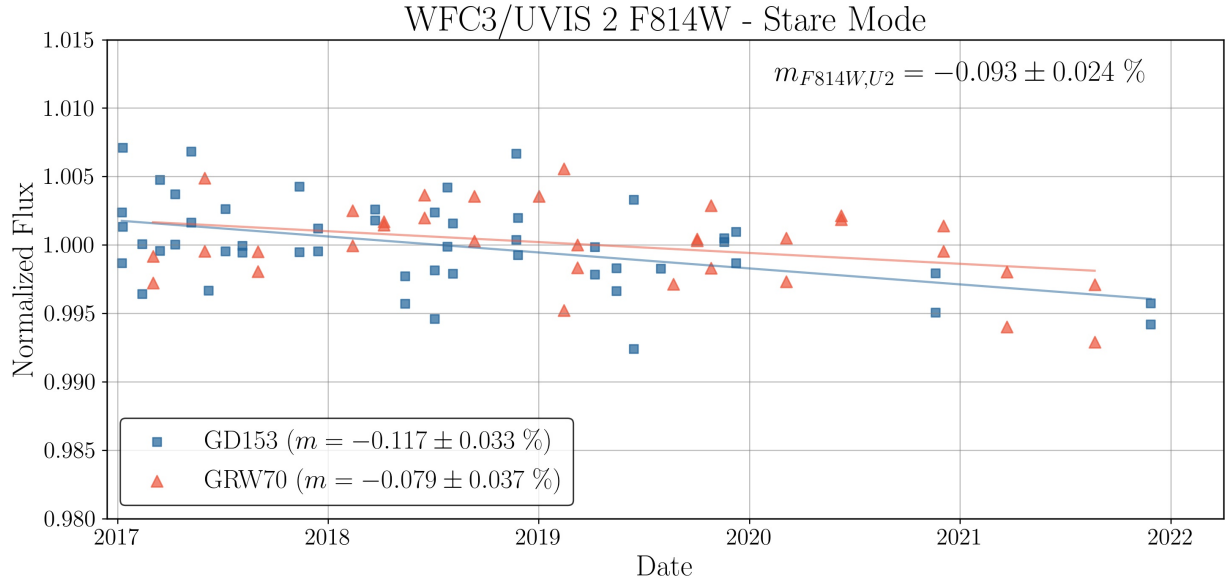


Figure A28: UVIS 2 (Amp C) F814W photometry for Concurrent data.

A3. Published Data

As defined in Section 3.4., the Published dataset is comprised of staring mode observations of GD153 and GRW70 in the set of core filters through November 2019 so as to include only data previously examined in 2021wfc..rept....4C.

Filter	Target	n	$m \pm m_{err}$ (%/yr)	σ (%)
F218W	GD153	66	-0.092 ± 0.037	0.558
	GRW70	155	-0.214 ± 0.018	0.643
F225W	GD153	67	-0.175 ± 0.037	0.896
	GRW70	175	-0.190 ± 0.016	0.865
F275W	GD153	47	-0.177 ± 0.038	0.669
	GRW70	126	-0.152 ± 0.014	0.650
F336W	GD153	72	-0.024 ± 0.012	0.380
	GRW70	136	-0.024 ± 0.012	0.395
F438W	GD153	92	-0.155 ± 0.009	0.414
	GRW70	152	-0.151 ± 0.011	0.473
F606W	GD153	79	-0.237 ± 0.013	0.459
	GRW70	159	-0.234 ± 0.013	0.548
F814W	GD153	73	-0.136 ± 0.011	0.405
	GRW70	118	-0.137 ± 0.012	0.577

Table A5: Same as Table A1, but derived from **all staring mode data through November 2019** (Published data set).

Filter	Target	n	$m \pm m_{err}$ (%/yr)	σ (%)
F218W	GD153	70	-0.119 ± 0.036	0.580
	GRW70	168	-0.250 ± 0.013	0.504
F225W	GD153	69	-0.182 ± 0.030	0.713
	GRW70	176	-0.233 ± 0.014	1.027
F275W	GD153	93	-0.213 ± 0.030	0.444
	GRW70	127	-0.182 ± 0.013	0.732
F336W	GD153	74	-0.160 ± 0.029	0.428
	GRW70	114	-0.057 ± 0.016	0.524
F438W	GD153	67	-0.240 ± 0.032	0.528
	GRW70	124	-0.191 ± 0.012	0.523
F606W	GD153	88	-0.201 ± 0.010	0.389
	GRW70	89	-0.269 ± 0.011	0.595
F814W	GD153	83	-0.150 ± 0.010	0.403
	GRW70	130	-0.145 ± 0.008	0.601

Table A6: Same as Table A5, but for UVIS 2 (Amp C) rates of detector sensitivity decline.

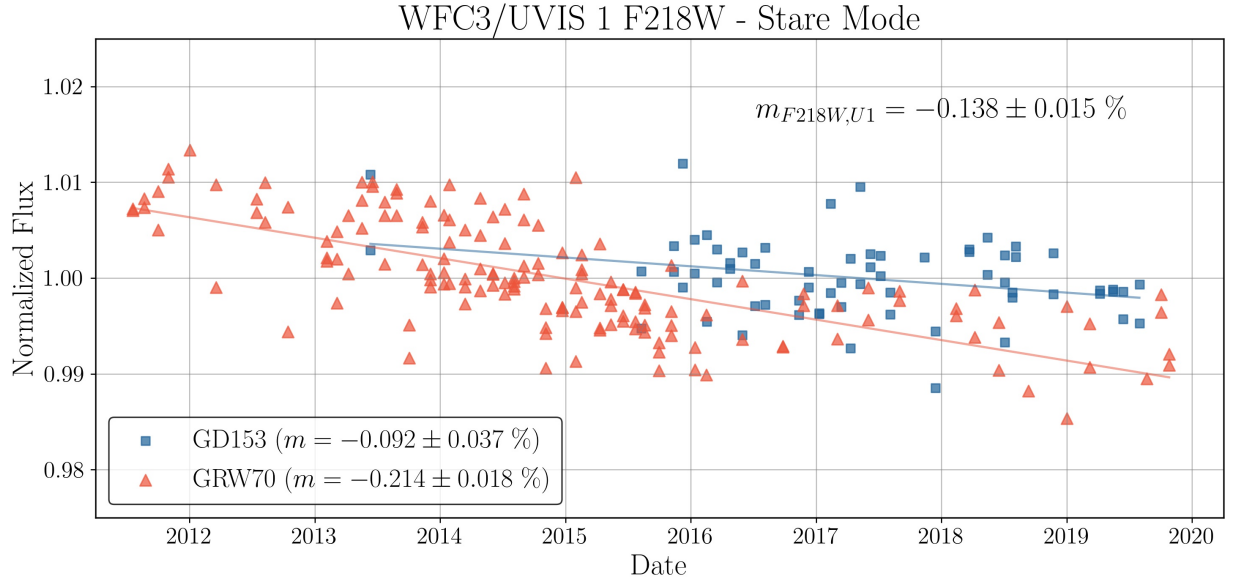


Figure A29: UVIS 1 (Amp A) F218W photometry for Published data.

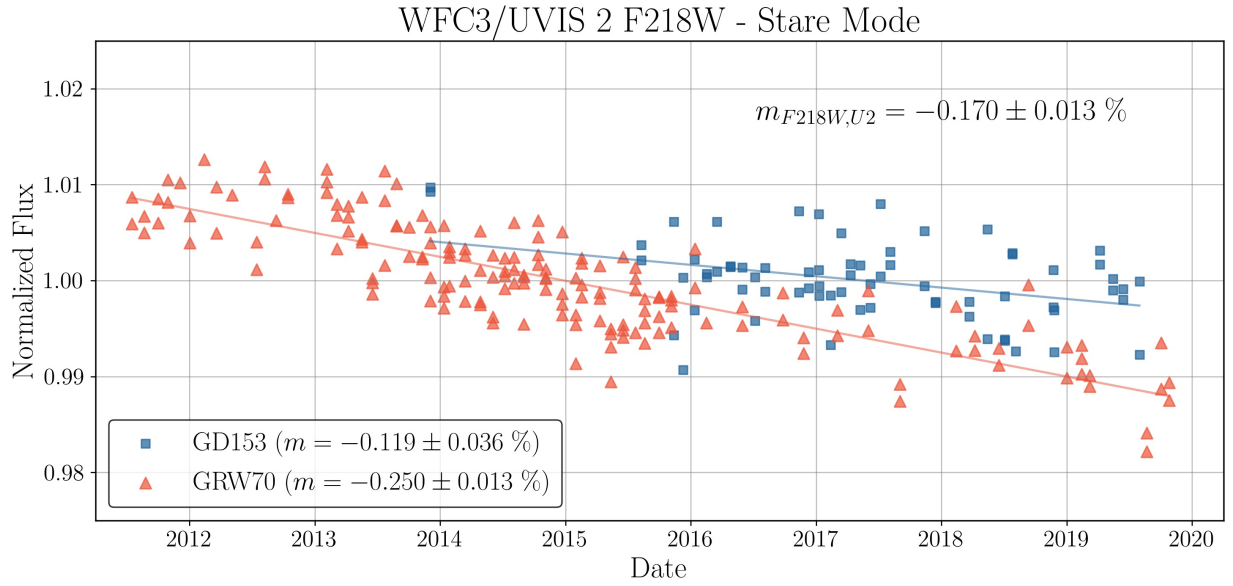


Figure A30: UVIS 2 (Amp C) F218W photometry for Published data.

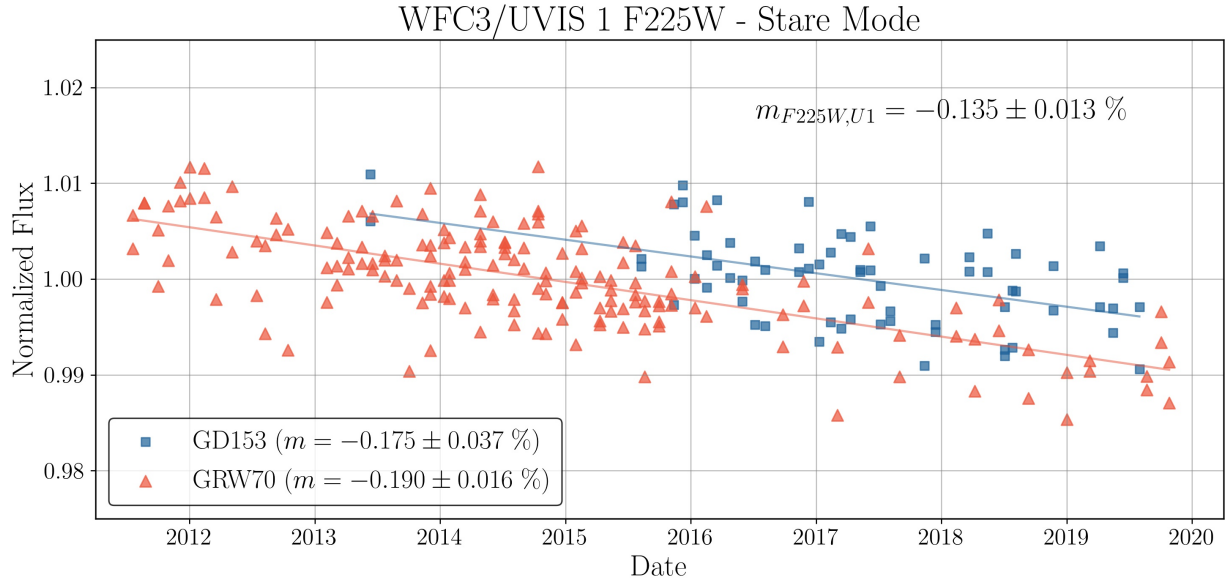


Figure A31: UVIS 1 (Amp A) F225W photometry for Published data.

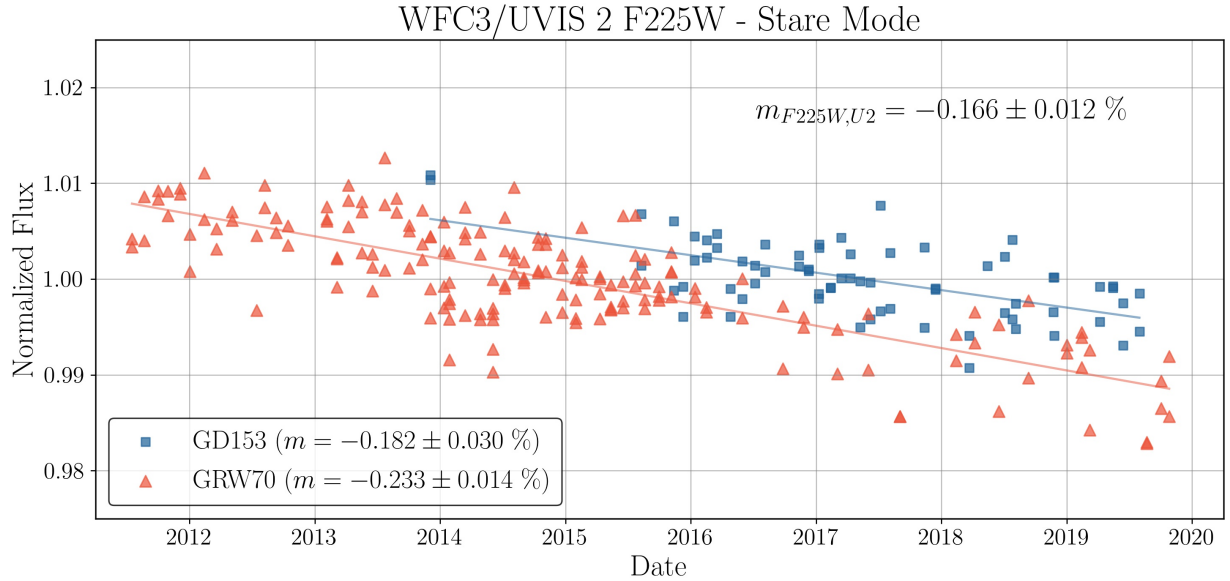


Figure A32: UVIS 2 (Amp C) F225W photometry for Published data.

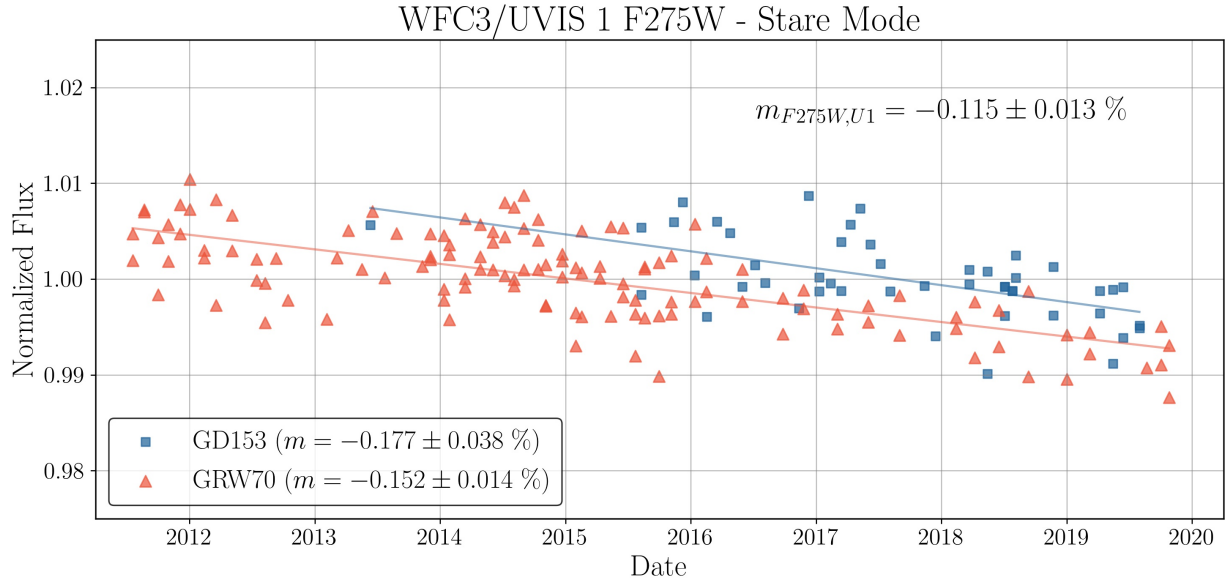


Figure A33: UVIS 1 (Amp A) F275W photometry for Published data.

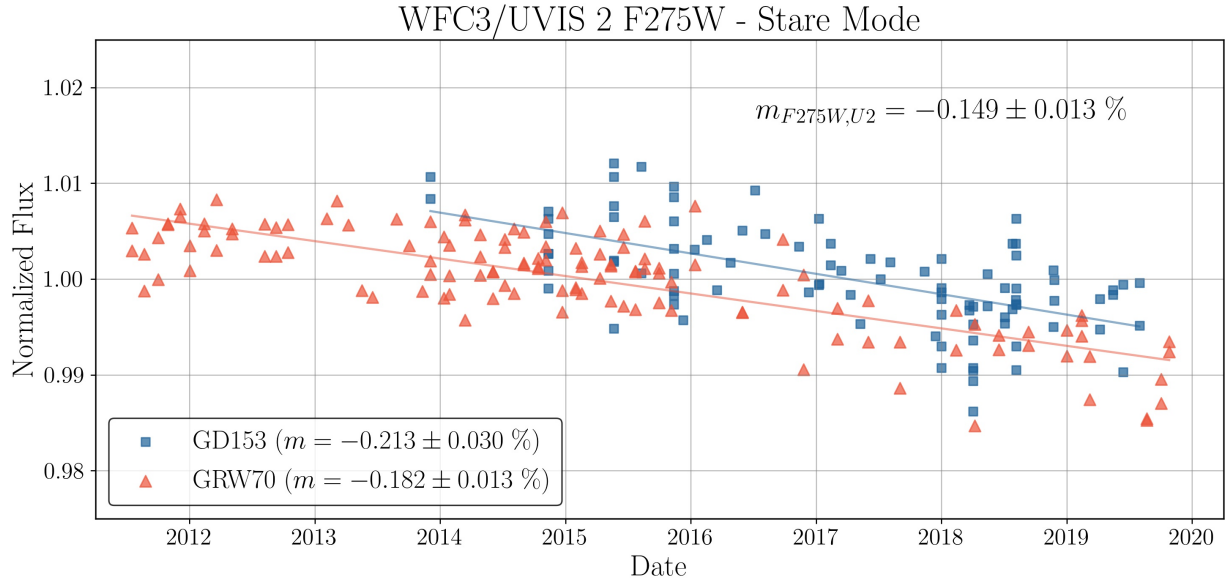


Figure A34: UVIS 2 (Amp C) F275W photometry for Published data.

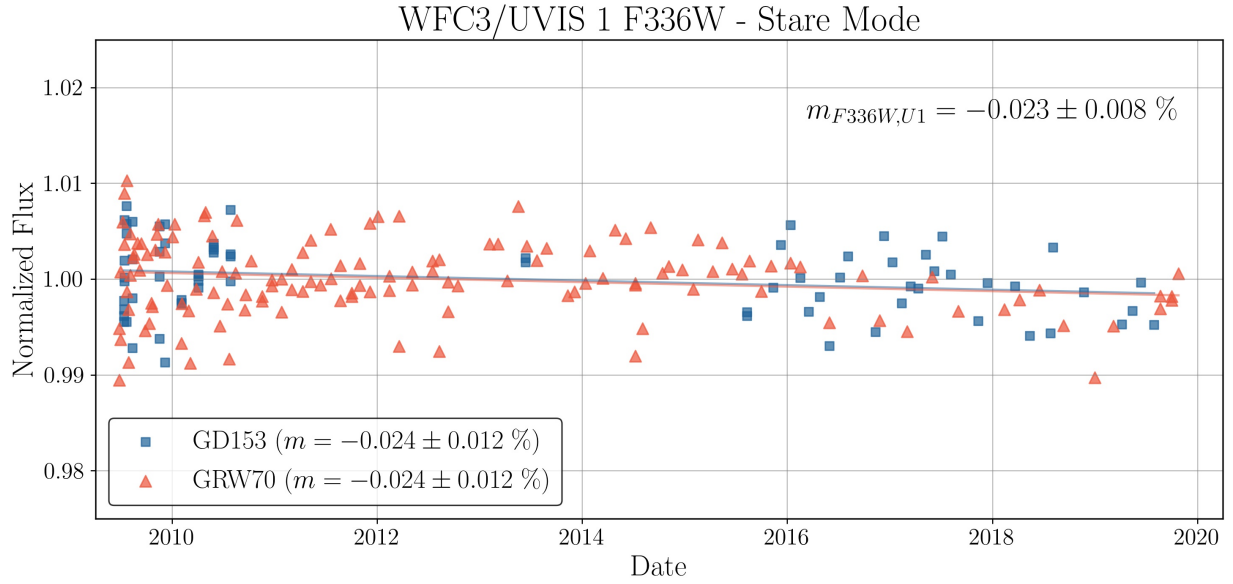


Figure A35: UVIS 1 (Amp A) F336W photometry for Published data.

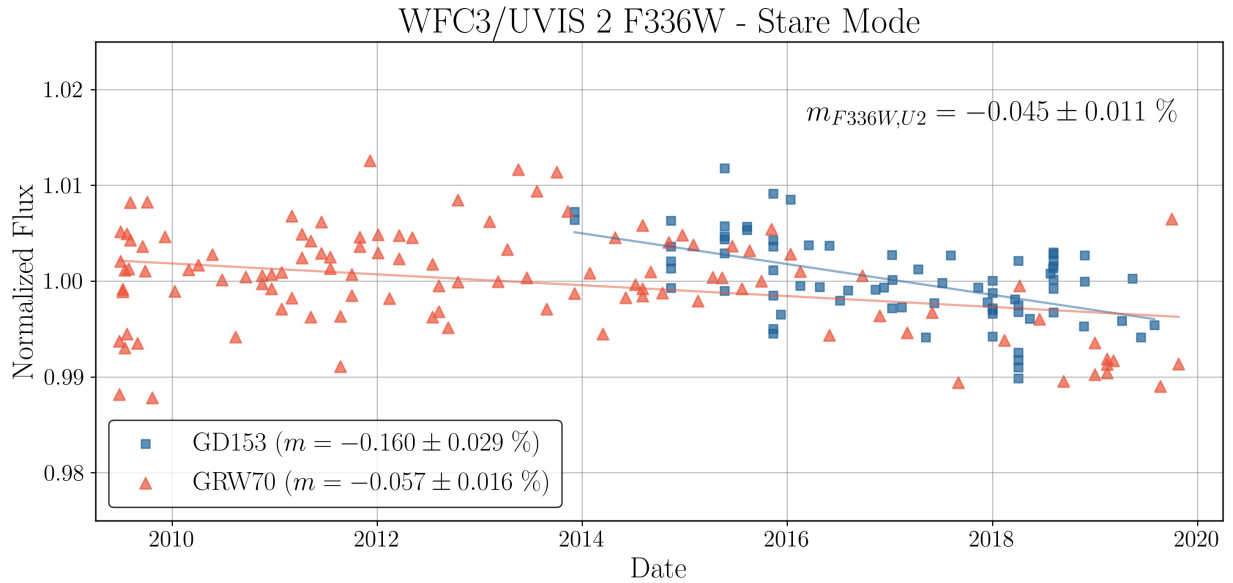


Figure A36: UVIS 2 (Amp C) F336W photometry for Published data.

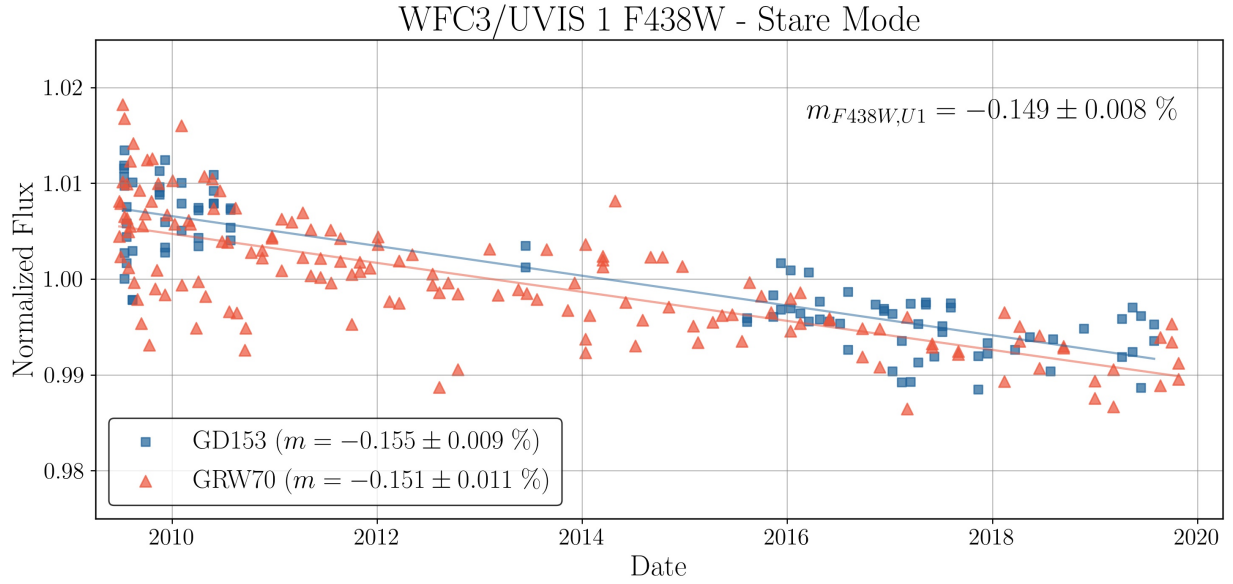


Figure A37: UVIS 1 (Amp A) F438W photometry for Published data.

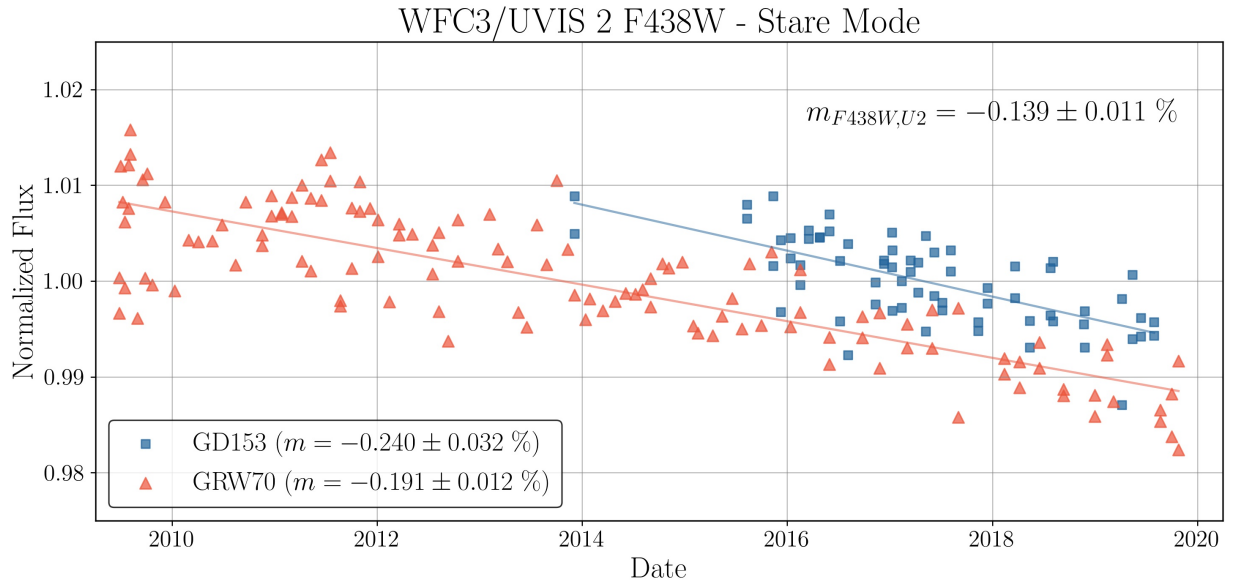


Figure A38: UVIS 2 (Amp C) F438W photometry for Published data.

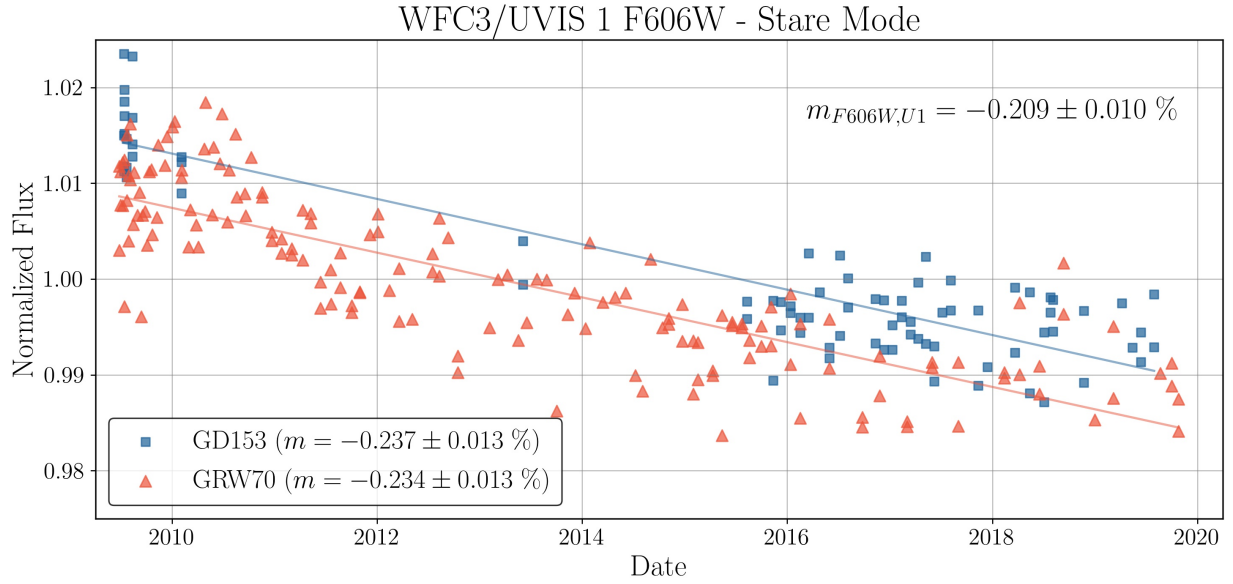


Figure A39: UVIS 1 (Amp A) F606W photometry for Published data.

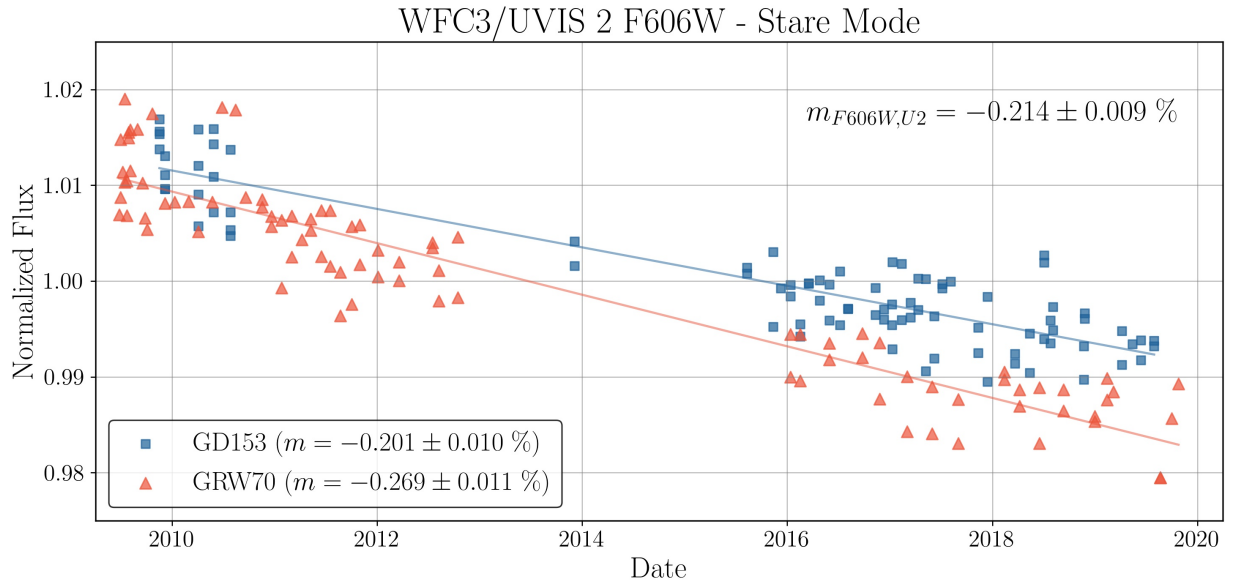


Figure A40: UVIS 2 (Amp C) F606W photometry for Published data.

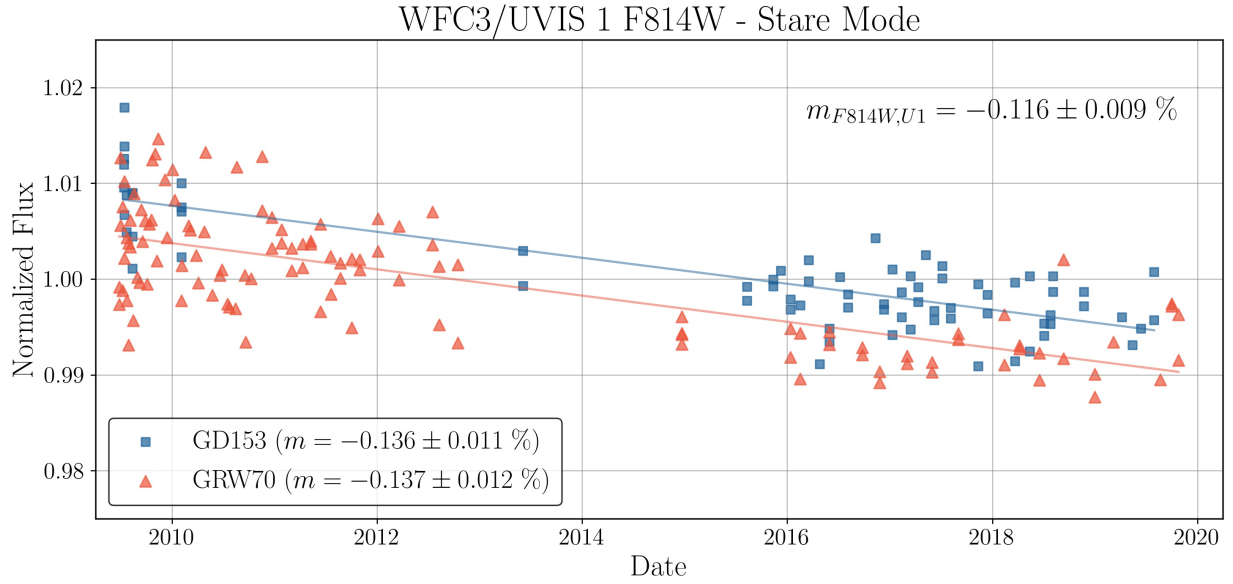


Figure A41: UVIS 1 (Amp A) F814W photometry for Published data.

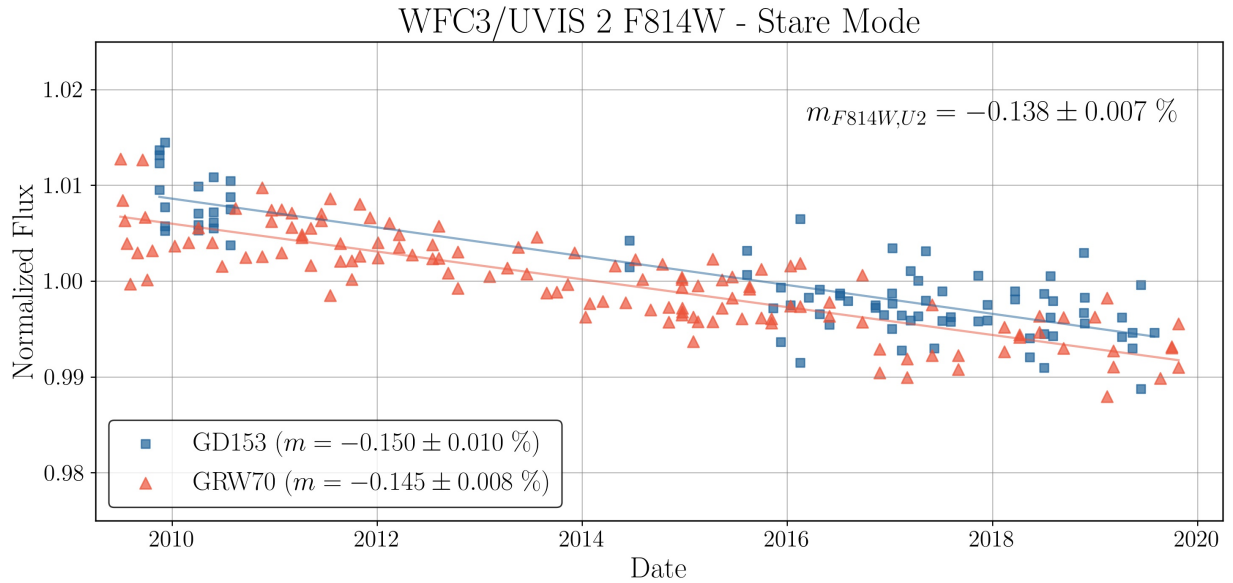


Figure A42: UVIS 2 (Amp C) F814W photometry for Published data.

A4. All Data

As defined in Section 3.4., the All dataset is comprised of all staring mode observations of GD153 and GRW70 in the set of core filters.

Filter	Target	n	$m \pm m_{err}$ (%/yr)	σ (%)
F218W	GD153	74	-0.079 ± 0.027	0.543
	GRW70	163	-0.235 ± 0.015	0.679
F225W	GD153	75	-0.164 ± 0.028	0.870
	GRW70	182	-0.211 ± 0.014	0.899
F275W	GD153	55	-0.195 ± 0.028	0.698
	GRW70	134	-0.185 ± 0.014	0.705
F336W	GD153	78	-0.030 ± 0.010	0.386
	GRW70	144	-0.055 ± 0.010	0.458
F438W	GD153	100	-0.153 ± 0.008	0.467
	GRW70	159	-0.159 ± 0.010	0.601
F606W	GD153	88	-0.210 ± 0.013	0.469
	GRW70	167	-0.221 ± 0.011	0.622
F814W	GD153	81	-0.122 ± 0.011	0.395
	GRW70	126	-0.134 ± 0.010	0.677

Table A7: Same as Table A1, but derived from **all staring mode data** (All data set).

Filter	Target	n	$m \pm m_{err}$ (%/yr)	σ (%)
F218W	GD153	78	-0.104 ± 0.027	0.583
	GRW70	179	-0.224 ± 0.011	0.542
F225W	GD153	77	-0.165 ± 0.023	0.730
	GRW70	186	-0.221 ± 0.011	1.069
F275W	GD153	101	-0.196 ± 0.025	0.502
	GRW70	137	-0.189 ± 0.011	0.788
F336W	GD153	81	-0.152 ± 0.023	0.442
	GRW70	124	-0.079 ± 0.013	0.569
F438W	GD153	75	-0.244 ± 0.023	0.544
	GRW70	134	-0.189 ± 0.010	0.595
F606W	GD153	94	-0.198 ± 0.009	0.407
	GRW70	99	-0.245 ± 0.010	0.639
F814W	GD153	91	-0.145 ± 0.009	0.407
	GRW70	140	-0.142 ± 0.007	0.635

Table A8: Same as Table A7, but for UVIS 2 (Amp C) rates of detector sensitivity decline.

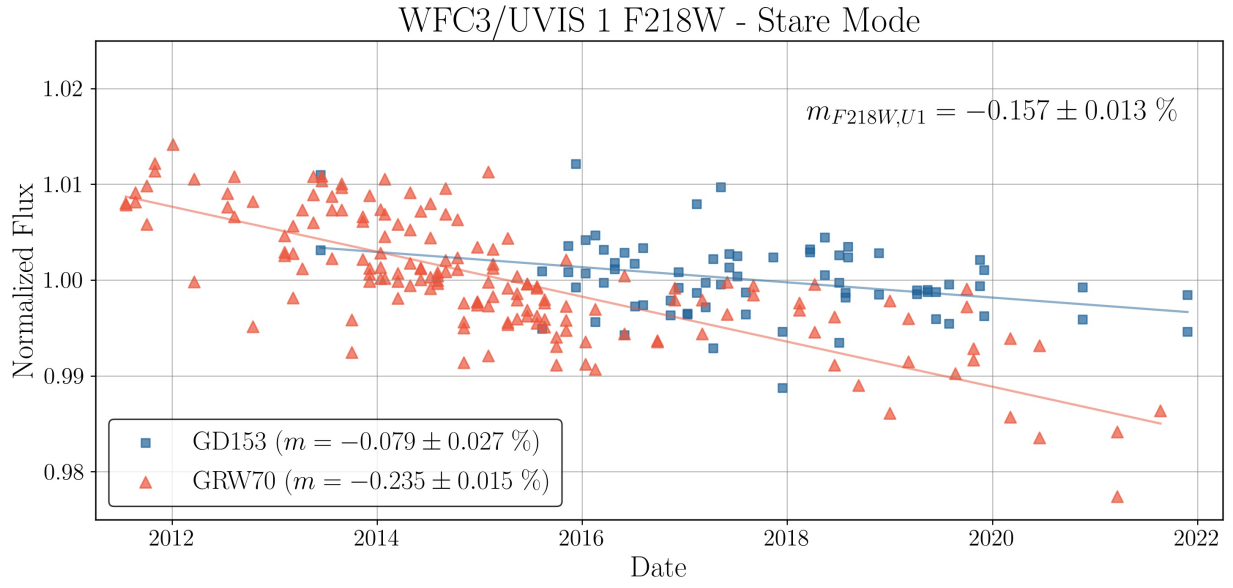


Figure A43: UVIS 1 (Amp A) F218W photometry for All data.

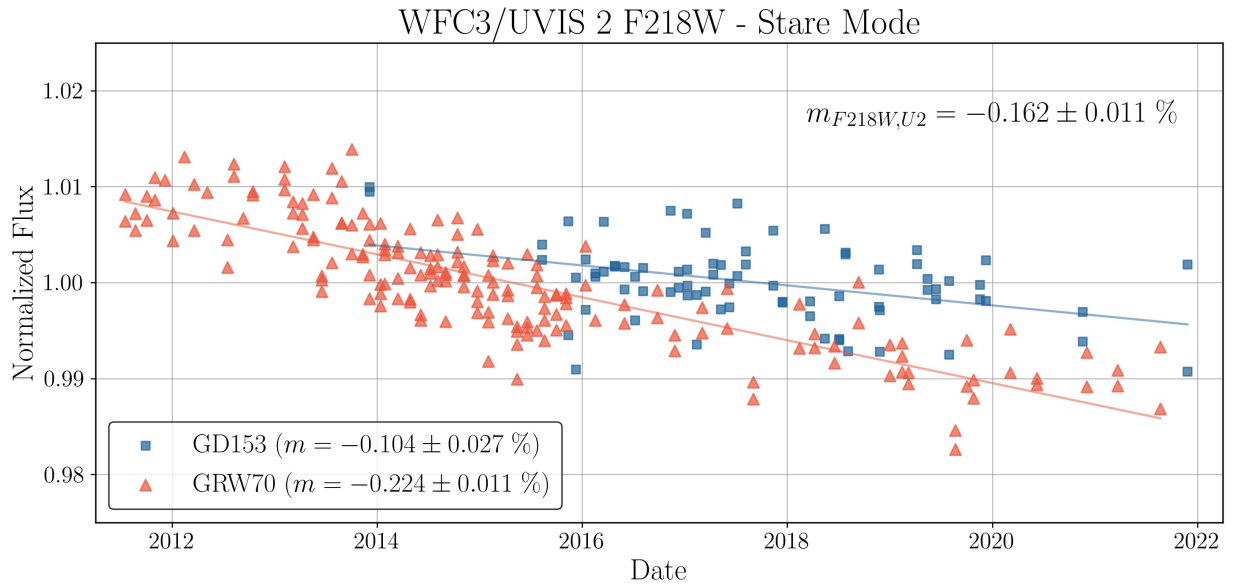


Figure A44: UVIS 2 (Amp C) F218W photometry for All data.

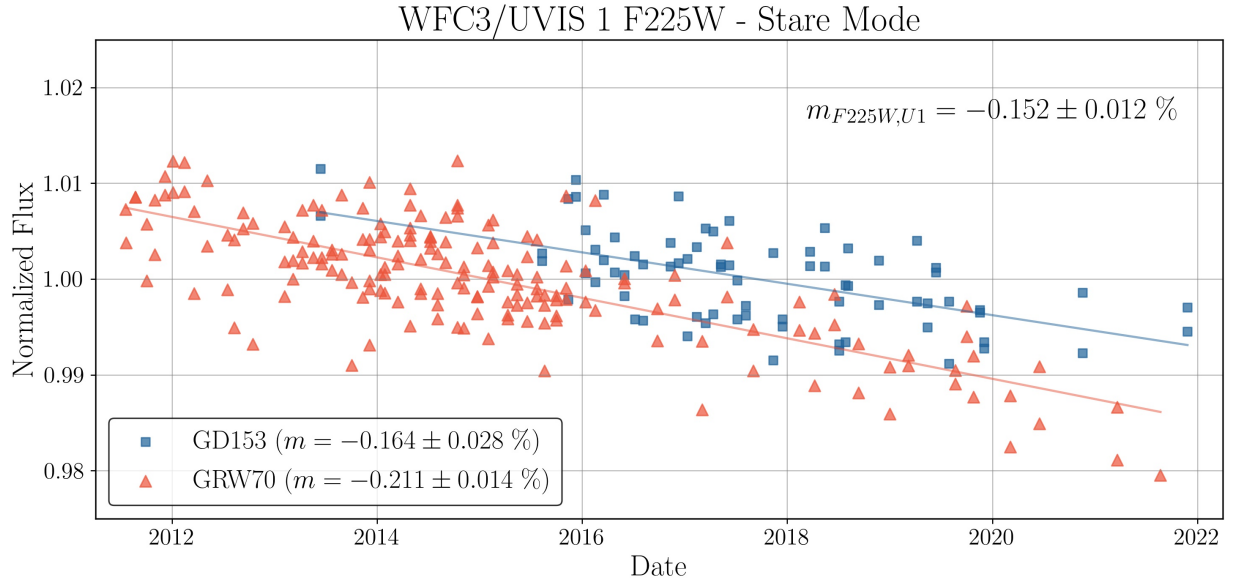


Figure A45: UVIS 1 (Amp A) F225W photometry for All data.

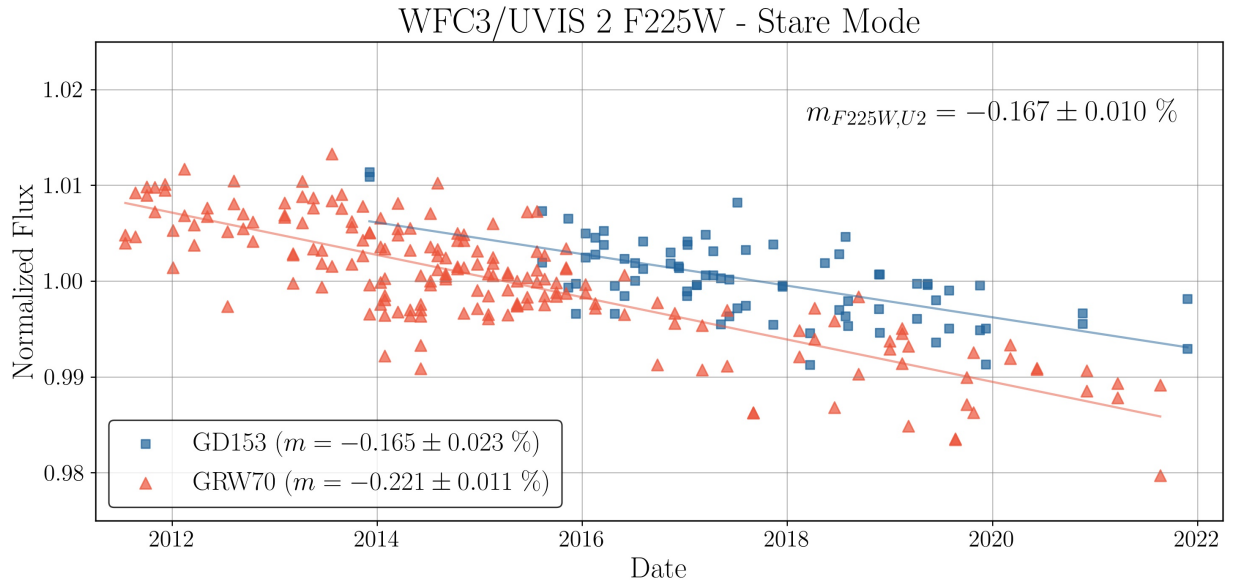


Figure A46: UVIS 2 (Amp C) F225W photometry for All data.

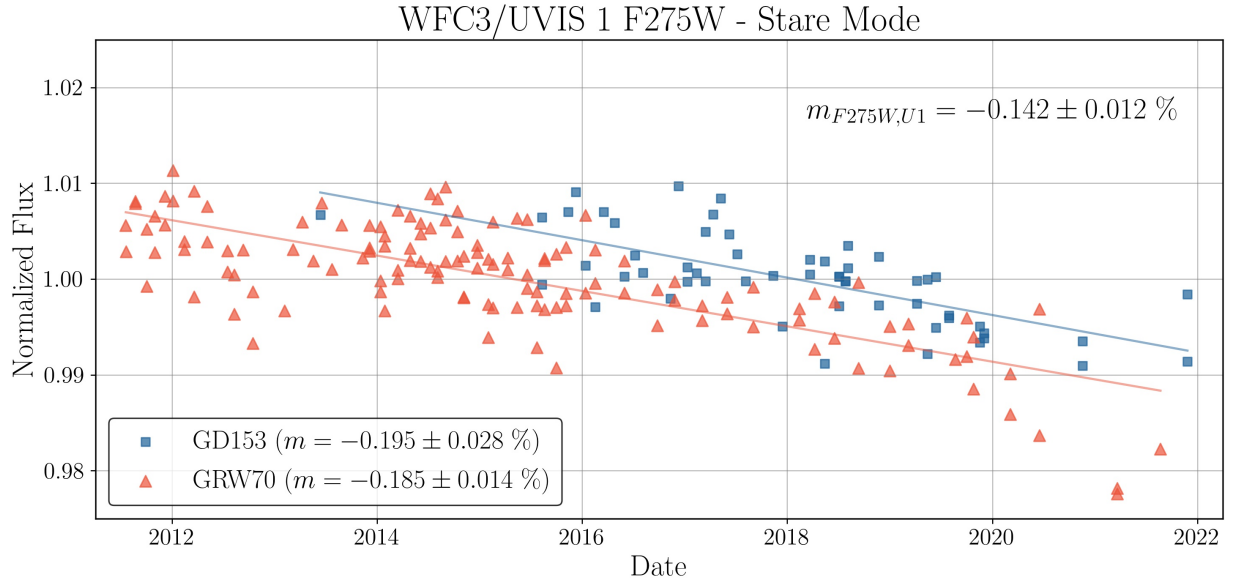


Figure A47: UVIS 1 (Amp A) F275W photometry for All data.

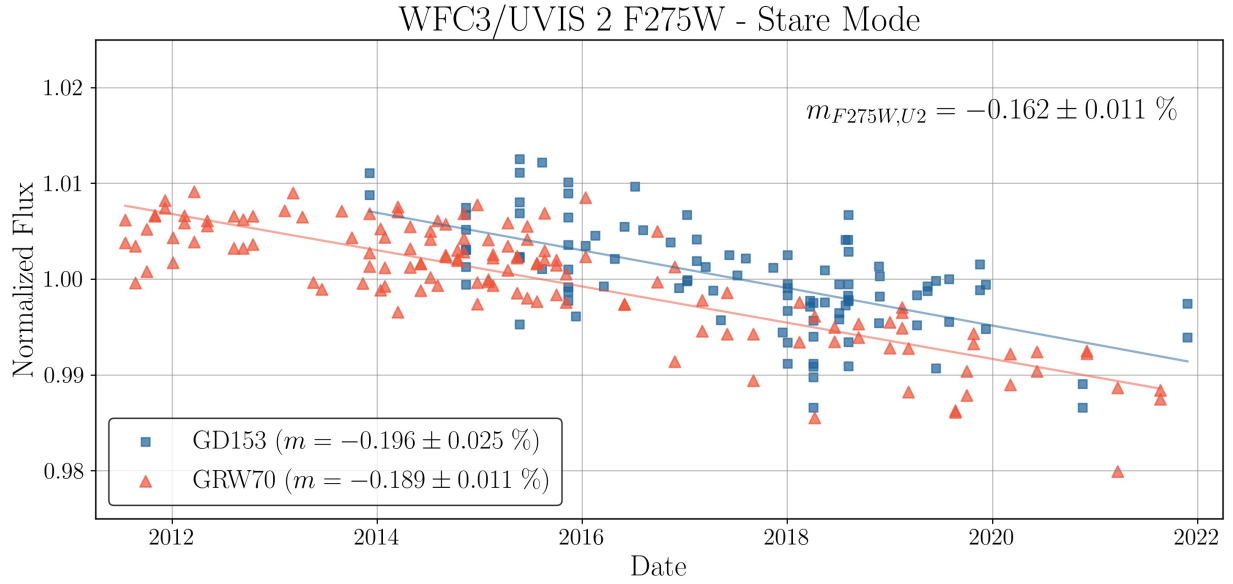


Figure A48: UVIS 2 (Amp C) F275W photometry for All data.

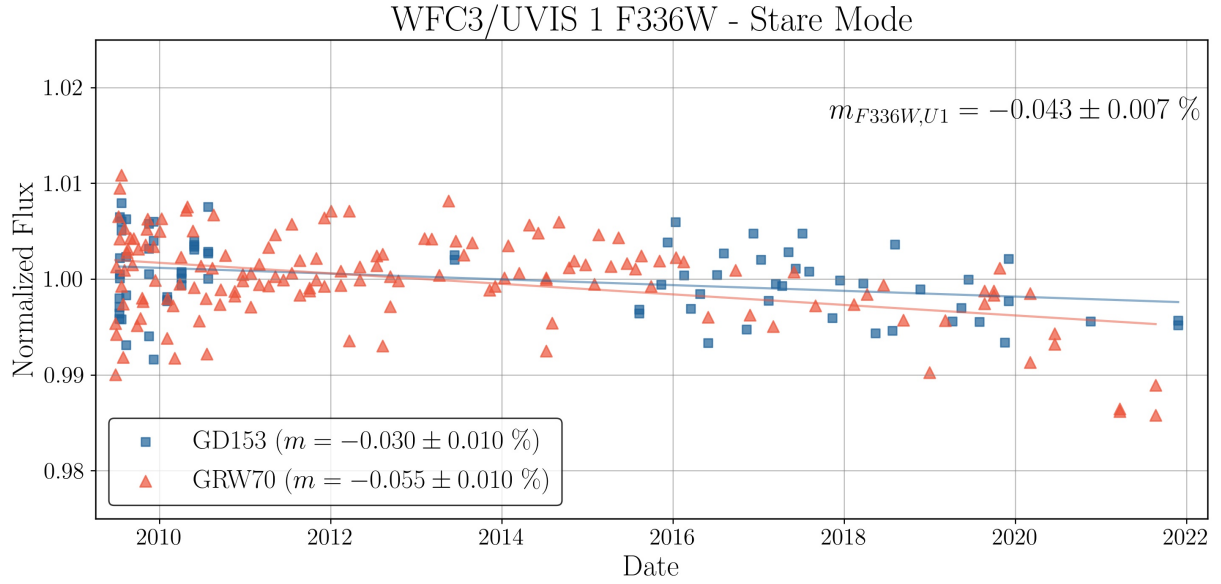


Figure A49: UVIS 1 (Amp A) F336W photometry for All data.

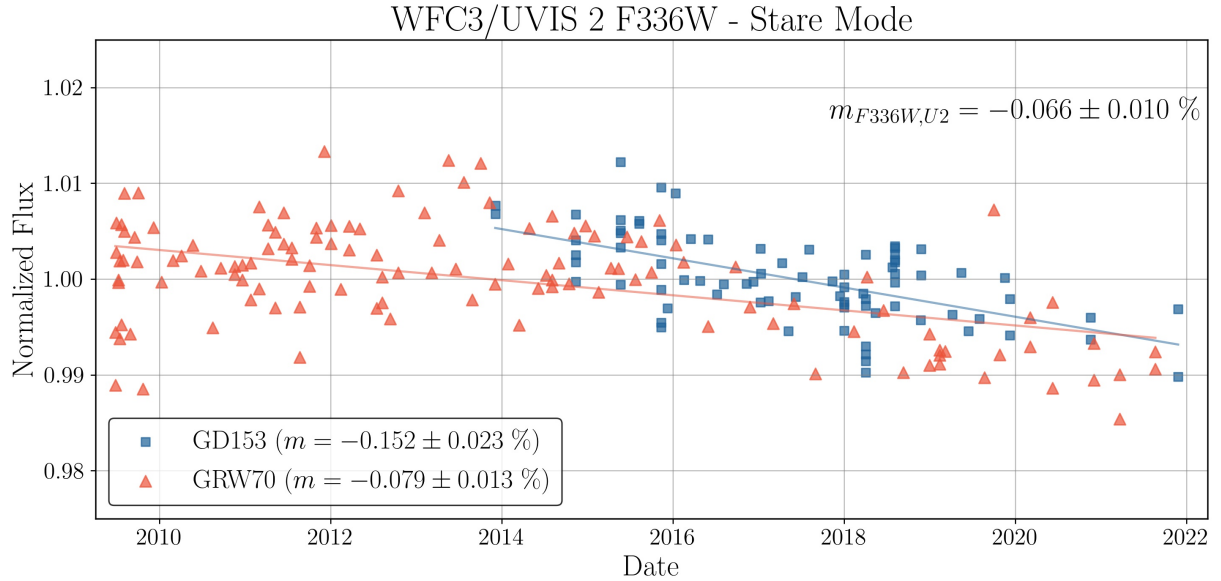


Figure A50: UVIS 2 (Amp C) F336W photometry for All data.

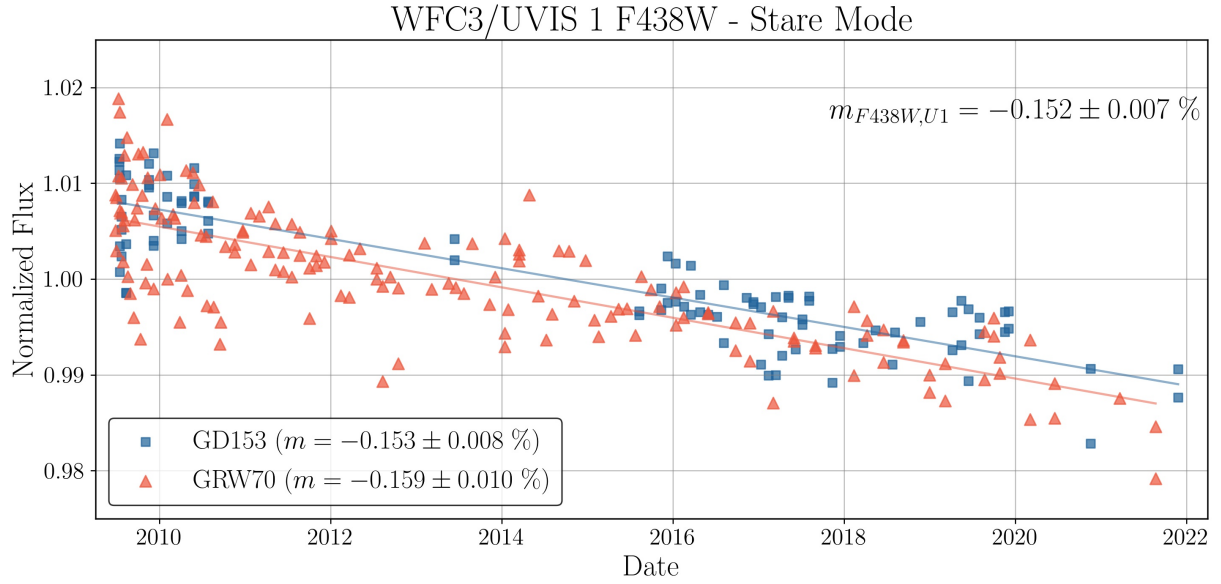


Figure A51: UVIS 1 (Amp A) F438W photometry for All data.

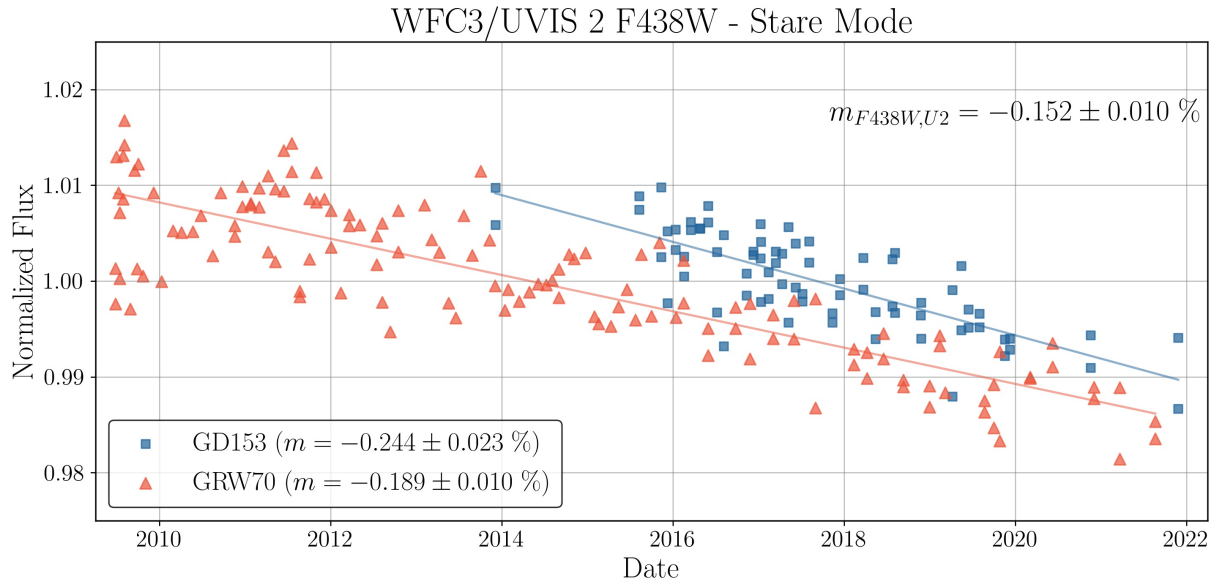


Figure A52: UVIS 2 (Amp C) F438W photometry for All data.

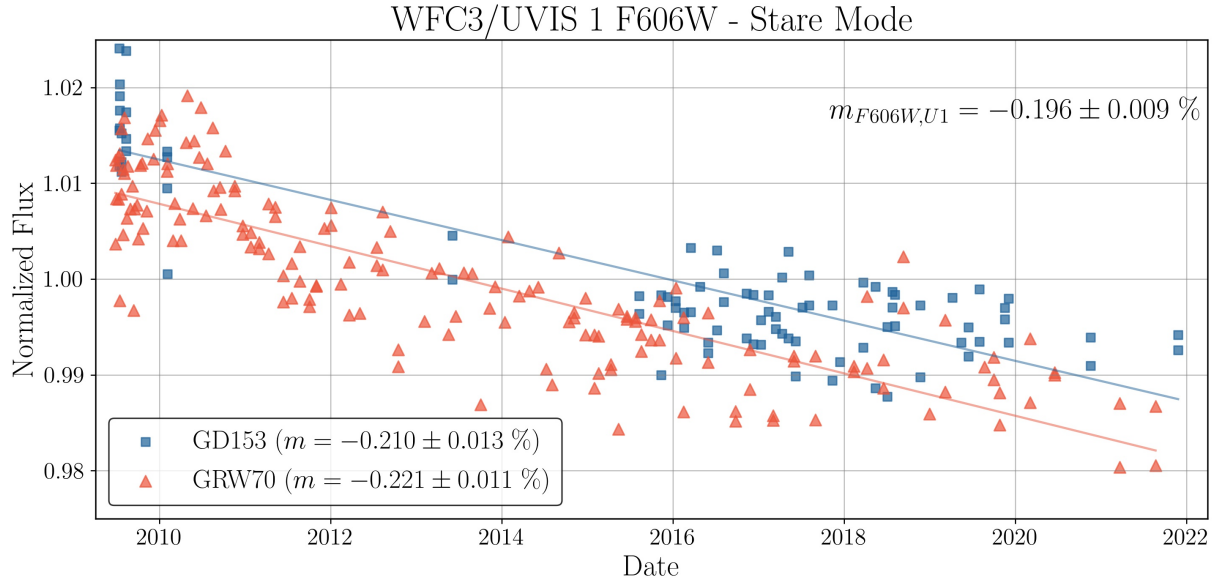


Figure A53: UVIS 1 (Amp A) F606W photometry for All data.

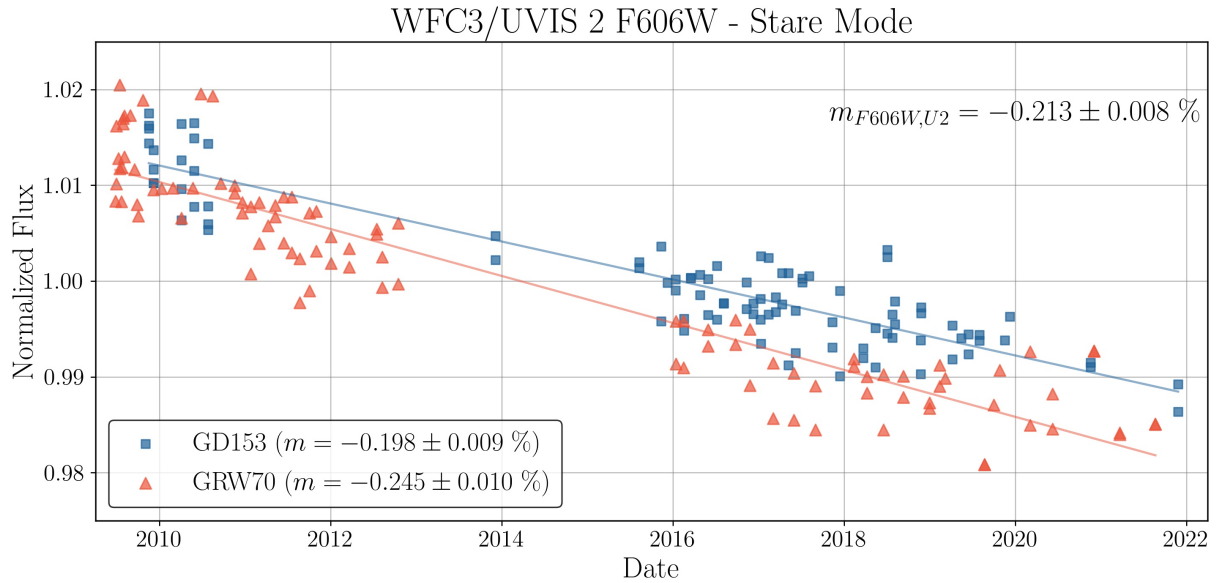


Figure A54: UVIS 2 (Amp C) F606W photometry for All data.

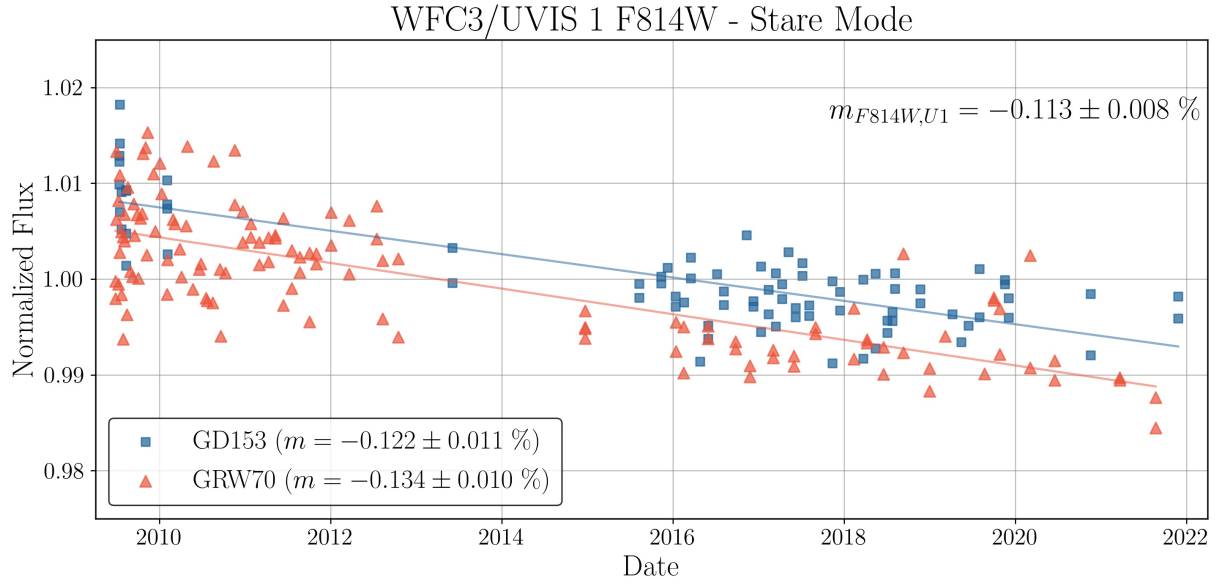


Figure A55: UVIS 1 (Amp A) F814W photometry for All data.

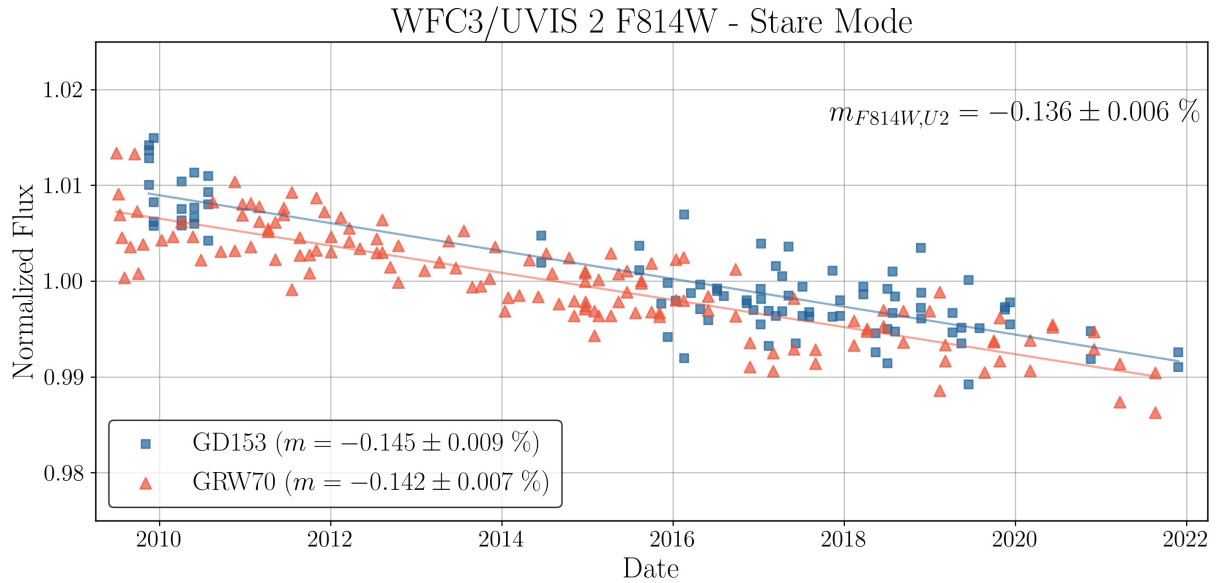


Figure A56: UVIS 2 (Amp C) F814W photometry for All data.

B Appendix B - Photometric Repeatability

Filter	Target	σ_{Scan} (%)	$\sigma_{Concurrent}$ (%)	$\sigma_{Concurrent}/\sigma_{Scan}$
F218W	GD153	0.198	0.368	1.86
	GRW70	0.205	0.438	2.14
F225W	GD153	0.193	0.383	1.99
	GRW70	0.207	0.451	2.18
F275W	GD153	0.180	0.304	1.69
	GRW70	0.163	0.387	2.38
F336W	GD153	0.122	0.281	2.31
	GRW70	0.116	0.365	3.14
F438W	GD153	0.099	0.359	3.65
	GRW70	0.140	0.325	2.32
F606W	GD153	0.052	0.341	6.58
	GRW70	0.087	0.458	5.26
F814W	GD153	0.164	0.279	1.70
	GRW70	0.159	0.391	2.46

Table B1: UVIS 1 (Amp A) target-specific $1 - \sigma$ dispersion for Scan and Concurrent data.

Filter	Target	σ_{Scan} (%)	$\sigma_{Concurrent}$ (%)	$\sigma_{Concurrent}/\sigma_{Scan}$
F218W	GD153	0.187	0.360	1.93
	GRW70	0.215	0.332	1.55
F225W	GD153	0.099	0.342	3.47
	GRW70	0.145	0.391	2.70
F275W	GD153	0.145	0.396	2.74
	GRW70	0.115	0.339	2.95
F336W	GD153	0.114	0.430	3.78
	GRW70	0.133	0.291	2.18
F438W	GD153	0.112	0.297	2.65
	GRW70	0.093	0.296	3.18
F606W	GD153	0.074	0.341	4.61
	GRW70	0.109	0.326	2.99
F814W	GD153	0.182	0.283	1.56
	GRW70	0.116	0.271	2.34

Table B2: Same as Table B1, but for UVIS 2 (Amp C) Scan and Concurrent data.

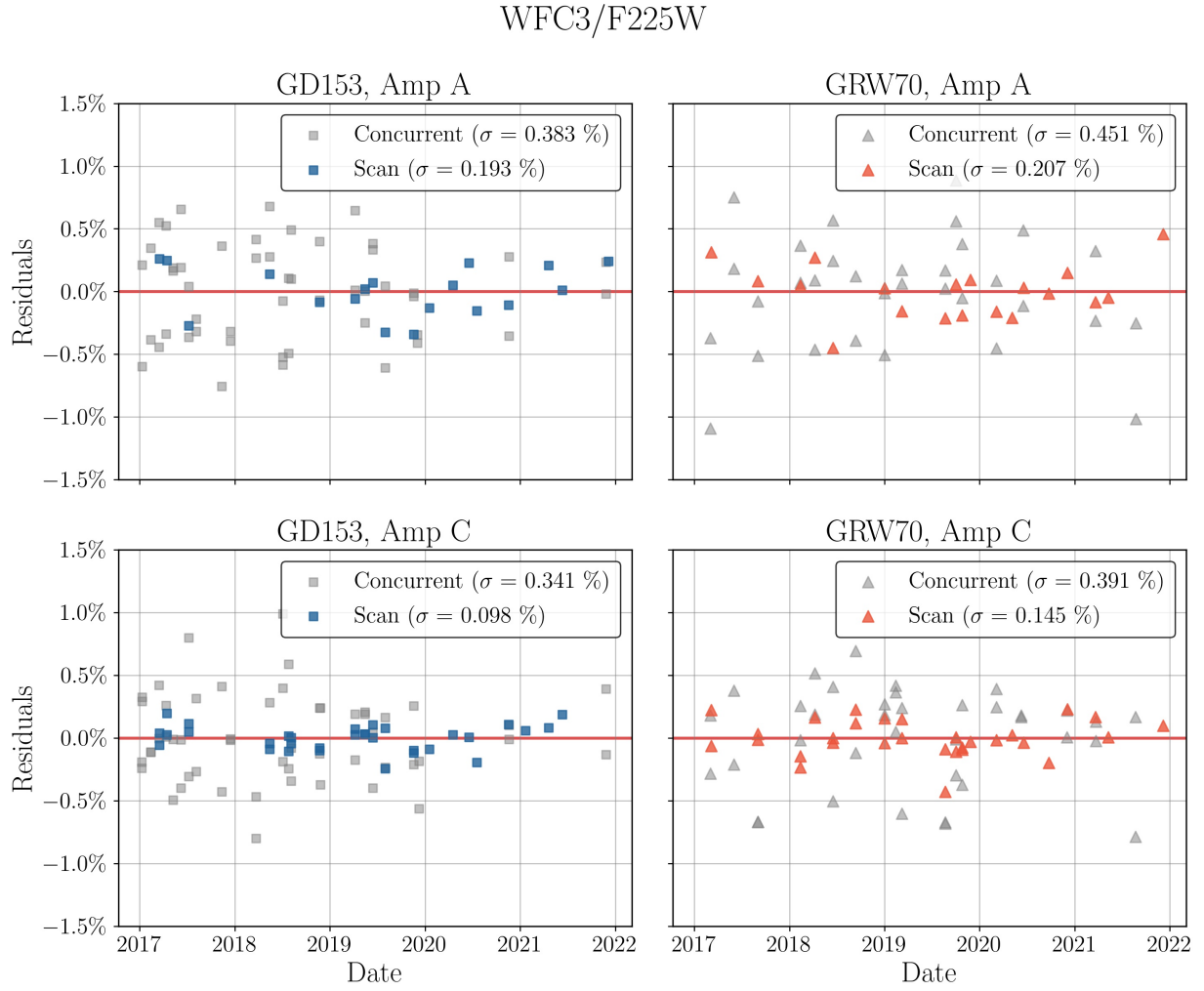


Figure B1: F225W residuals for scan and staring mode data from 2017 to 2021.

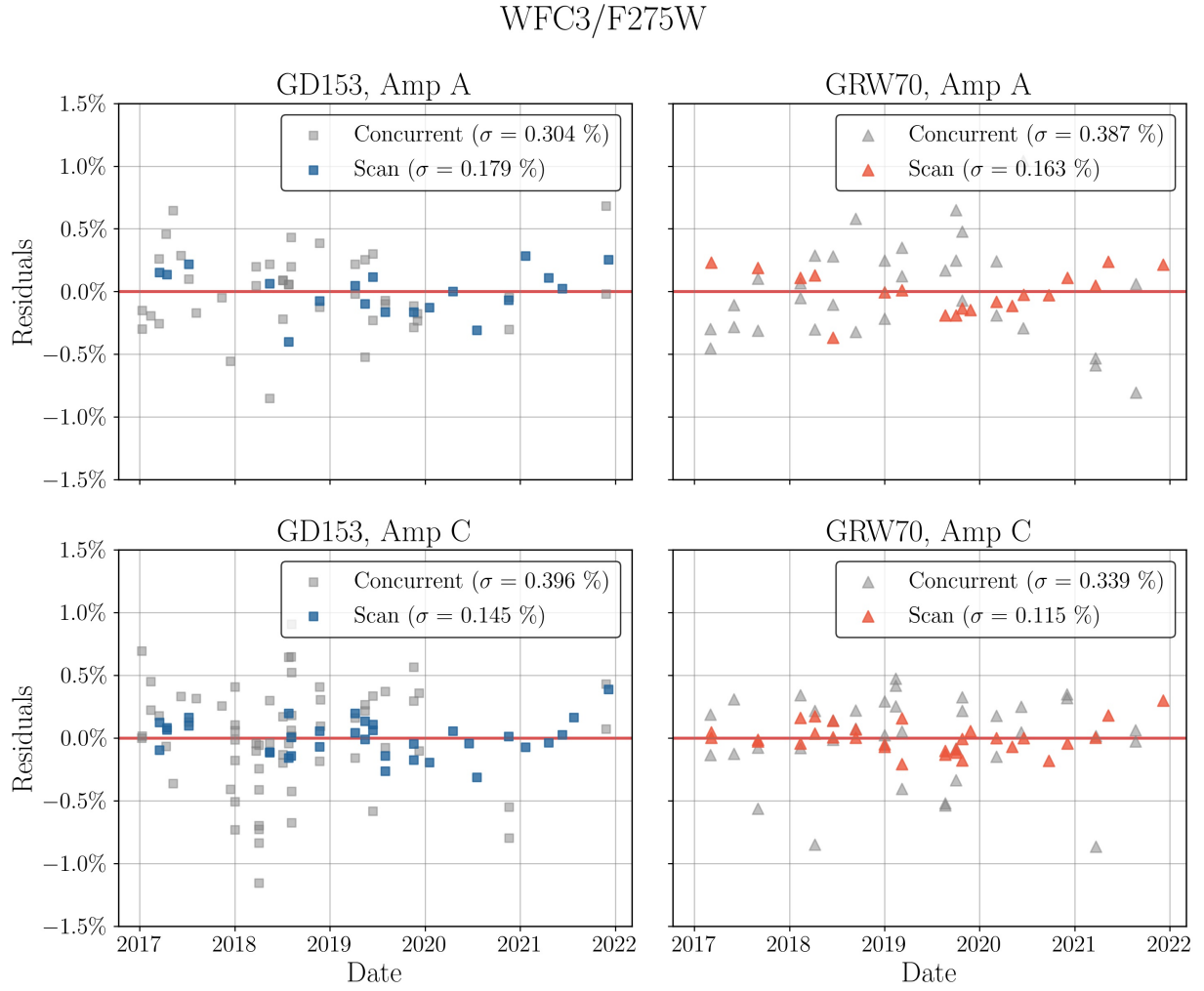


Figure B2: F275W residuals for scan and staring mode data from 2017 to 2021.

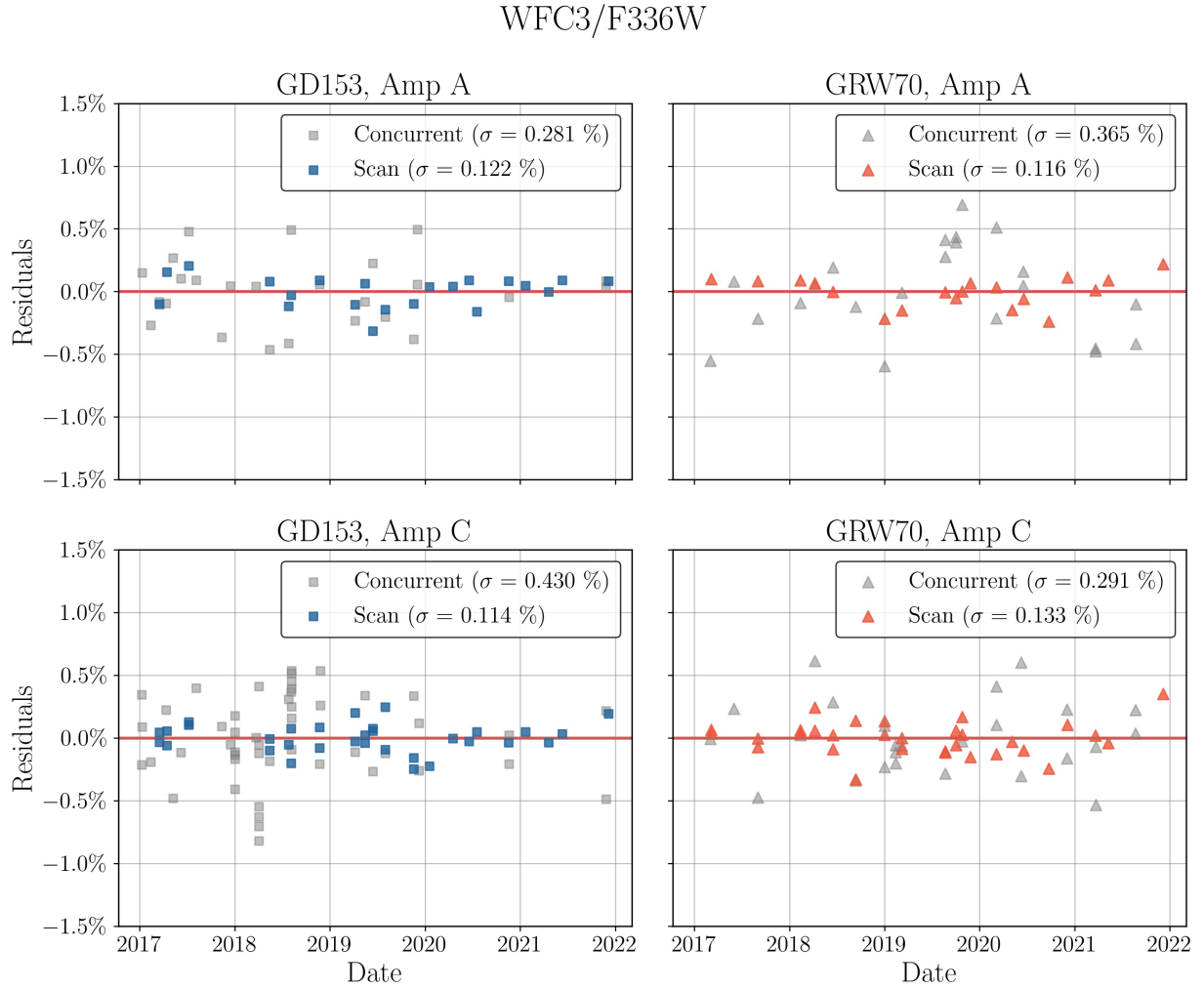


Figure B3: F336W residuals for scan and staring mode data from 2017 to 2021.

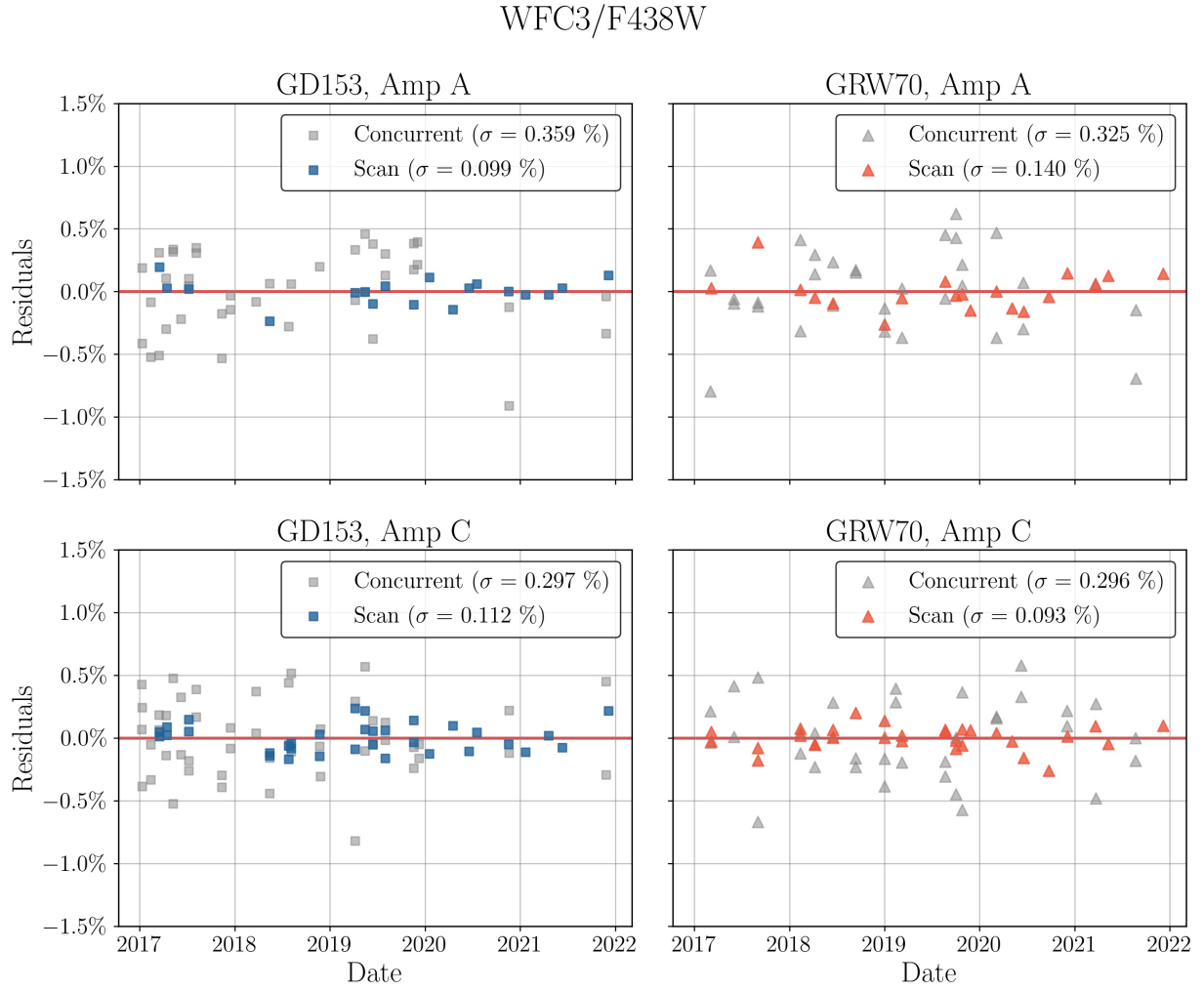


Figure B4: F438W residuals for scan and staring mode data from 2017 to 2021.

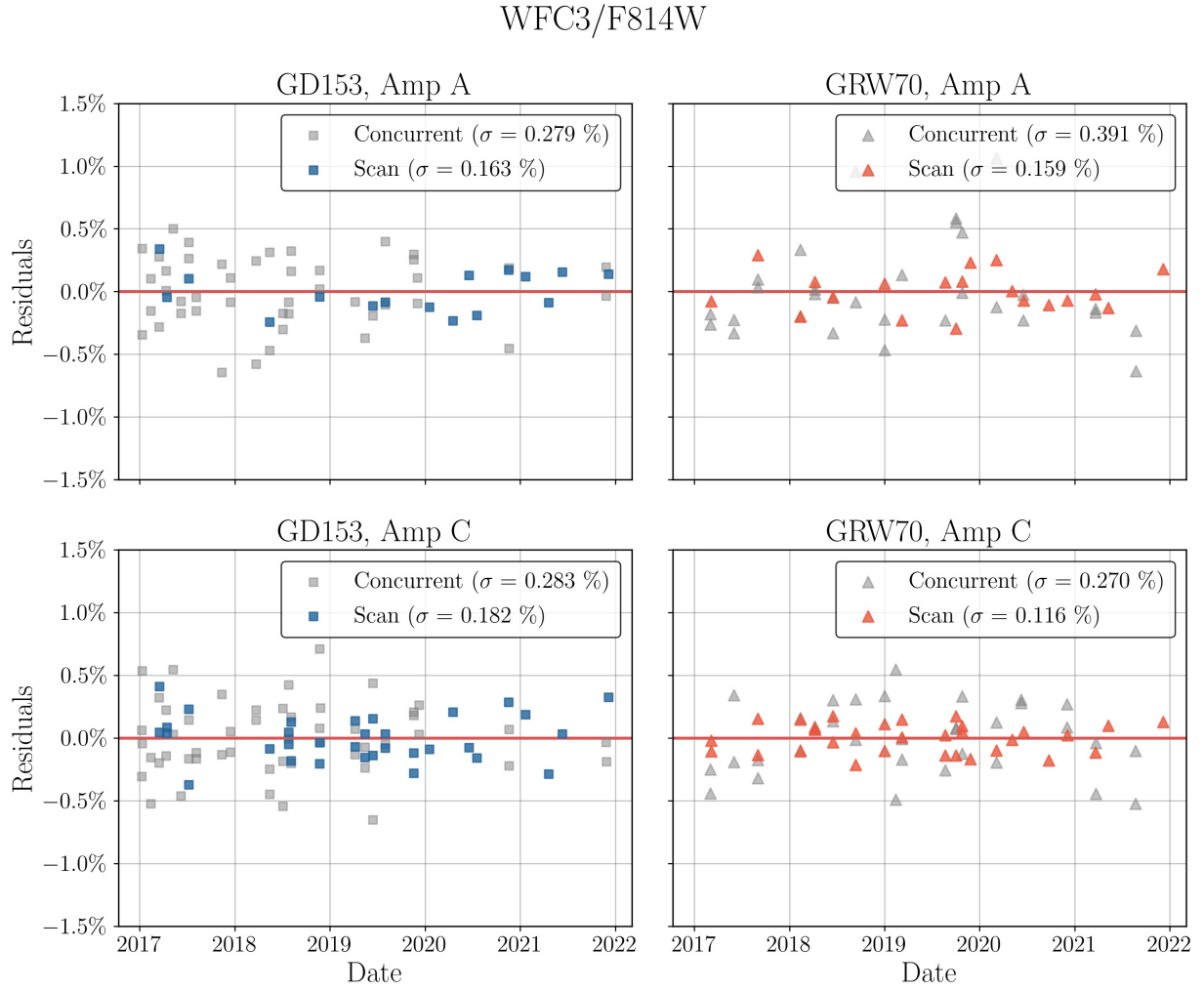


Figure B5: F814W residuals for scan and staring mode data from 2017 to 2021.